

A Mechanics Study on Surface Ruga Morphologies of Soft Materials

by

Ruikang Zhao

B. E., Xi'an Jiaotong University, 2012

M. S., Brown University, 2014

A dissertation submitted in partial fulfillment of the
requirements for the Degree of Doctor of Philosophy
in the School of Engineering at Brown University

Providence, Rhode Island

May 2016

© Copyright 2016 by Ruike Zhao

This dissertation by Ruike Zhao is accepted in its present form
by the School of Engineering as satisfying the
dissertation requirement for the degree of Doctor of Philosophy.

Date_____

Prof. Kyung-Suk Kim, Advisor

Recommended to the Graduate Council

Date_____

Prof. Huajian Gao, Reader

Date_____

Prof. Christian Franck, Reader

Approved by the Graduate Council

Date_____

Prof. Peter M. Weber
Dean of the Graduate School

Vita

Ruike Zhao was born September 15, 1990 in Xi'an, China. She attended Xi'an Jiaotong University in 2008, and received the B.E. in Mechanical Engineering in 2012. Subsequently, she entered Brown University at the fall of 2012 for graduated program in Solid Mechanics and got her M.S. in School of Engineering in May 2014. Her research focused on modeling and simulations of deformation of soft material and its applications.

Acknowledgments

First, I'm very grateful to my advisor Prof. Kyung-suk Kim, whose intelligence of thinking, brilliant ideas, and untiring support made this thesis possible. Before I started my graduate study, Prof. Kim took me as a visiting student in his lab in January 2012 when I was still a senior student in Xi'an Jiaotong University. He taught me so many things including how to design scientific devices, how to work as a qualified experimentalist and the how to become a good researcher. Although most of my works done are computation-oriented, I have benefited a lot from his diversity of research.

Second, special gratitude to Prof. Huajian Gao, for his encouragement and scientific guidance throughout my graduate studies.

Third, my thanks to Prof. Christian Franck, member of both my thesis and preliminary exam committee, who spent a lot of time reading and offering me suggestions for my thesis writing.

I would also like to thank everyone who has been working in the same lab and office with me, in particularly Dr. Mazen Diab and Dr. Teng Zhang, for their valuable advices and discussions on my research and study. And remote thanks to my friends in China, who have shown their greatest support from more than seven thousand miles away. Furthermore, I would like to express my thanks to the staffs in the lab, machine shop for their help. I appreciate the lab facilities and computing resources that are provided by Brown University.

Most important, I would like to express my deepest gratitude to my parents, Wushan Zhao and Xiuli Lei, for their endless dedication throughout my existing time on earth. I wouldn't have achieved anything without their love and care.

Contents

Signature Page	iii
Vita	iv
Acknowledgements	v
Table of Contents	vi
List of Tables	ix
List of Figures	x
1 Introduction.....	1
1.1. Briefing on “Ruga Mechanics”.....	1
1.2. Studies on major ruga phases and their transitions	3
1.2.1. Wrinkle.....	4
1.2.2. Crease.....	5
1.2.3. Fold	6
1.2.4. Ridge	7
1.2.5. Delamination ruga	7
1.2.6. Two-dimensional Ruga	8
1.3. Methodology and approaches.....	8
1.4. Outline of the thesis	9
2 The Primary Bilayer Ruga-Phase Diagram I: Evolution of Multi-mode Wrinkles, Folds and Creases [13].....	12

2.1. Introduction	12
2.2. Ruga evolution leading to global ruga localization.....	14
2.3. Computational analysis of ruga localization	16
2.4. Results and discussions: The PB ruga-phase diagram.....	18
2.4.1. Global crease localization	18
2.4.2. Fold and ridge localizations	21
2.4.3. The PB ruga-phase diagram	23
2.5. Conclusion	28
 3 The Primary Bilayer Ruga-Phase Diagram II: Irreversibility in Ruga Evolutions*	
.....	29
3.1. Introduction	29
3.2. Generic irreversible ruga-phases of the primary bilayer	32
3.2.1. Irreversible ruga-phases of cooperative-mode creases.....	34
3.2.2. Irreversible ruga-phases of multi-mode wrinkles.....	39
3.3. Irreversible transitions of multi-mode wrinkles of PB without strain mismatch .	40
3.4. Primary-period switching jumps in cyclic ruga evolution of PB with strain mismatch	43
3.5. Enhancements in cyclic ruga irreversibility: causes and consequences	48
3.5.1. Viscosity effect on Primary-period switching jumps in cyclic ruga-evolution.....	49
3.5.2. Cyclic stability of ruga configuration hysteresis and coexistence of ruga-phases ...	51
3.6. Conclusion	55
 4 The Primary Bilayer Ruga-Phase Diagram III: Ridging Transitions and Mobility Bifurcations of Ridges*	
.....	57
4.1. Introduction	57

4.2. Computational implementation.....	60
4.3. Ruga period and mode control under pre-stretch effect.....	61
4.3.1. Ruga period and mode control for $R>1$	63
4.3.2. Crease period control for equi-modulus bilayer.....	64
4.4. Ridging and order-disorder transition	66
4.4.1. Wrinkle-ridge and order-disorder transitions.....	69
4.4.2. Detection of order-disorder patterns and coexistence of phases	72
4.4.3. Ruga mobility bifurcations.....	79
4.5. Ruga order-disorder transition for 2D systems	81
4.6. Conclusion	84
5 Ruga Morphological Control.....	86
5.1. Introduction	86
5.2. Experimental setup.....	87
5.3. Results and discussions	89
5.3.1. <i>Ridge suppression</i> in graded modulus system with large strain mismatch	90
5.3.2. Hierarchical wrinkles and co-existent phases in graded material with kinked modulus distribution	95
5.4. Summary of ruga morphologies control aspects and factors	101
5.5. Conclusion	103
6 Conclusions and Perspectives	105
6.1. Overall conclusions.....	105
6.2. Outlook of future research.....	107
Bibliography	109

List of Tables

5.1.	Ruga morphological control aspects and factors.....	101
------	---	-----

List of Figures

1.1.	Ruga phases in nature and engineered materials: (a) schematics of ruga phases in 1D structure; (b) 50nm gold film folds: blue-red: 0-2 MPa Mises stress [5]; (c) graphene folds, on PDMS (top and side views) [77]; (d) 2D ruga pattern on 10 nm ion beam implanted DLC on PDMS [158]; (e) the cortex structure of Einstein's brain (discover magazine); (f) interface crease in proliferation and differentiation of hematopoietic cells: Morphology of U937 and HL-60 cells stimulated with Phyco-CM and others [171]; (g) ridge, crease patterns observed on colon [172]; (h) folds on muscular artery wall [172]; (i) ridges and ridge folds on mesenteric artery wall [172].....	2
2.1.	Schematics of ruga localizations in PB systems: (a) A PB composed of a neo-Hookean thin film with thickness h and shear modulus μ under lateral compression; (b) various ruga phases in ruga evolution; (c) three types of global ruga localization.....	16
2.2.	Pathways to global crease localization of soft-film bilayers: (a) schematics of four different pathways to global crease localization; FEM simulation plots of the maximum principal nominal strain, ε_p^{\max} , for (b) instantaneous crease ($\bar{k} = 1.44$); (c) wrinkle – film crease – global crease localization ($\bar{k} = 1.00$); (d) wrinkle – double-mode wrinkle – quadruple-mode crease – global crease localization ($\bar{k} = 0.87$); (e) wrinkle – double-mode wrinkle – quadruple-mode wrinkle – quadruple-mode wrinkle-tip crease – quadruple-mode crease-fold – global crease	

- localization ($\bar{k} = 0.41$): Frames in the dotted box of (c) and (d) show final localization processes in a different scale. The color bar of ε_p^{\max} ranges (b) 0-1.14, (c) 0-0.94, (d) 0-1.09 and (e) 0-0.77.....18
- 2.3. Pathways to global localization of stiff-film bilayers: (a) global fold localization with pathways of wrinkle – double-mode wrinkle – quadruple-mode wrinkle – fold – global fold localization (The FEM frame display is for $\bar{k} = 0.17$); (b) global ridge localization caused by pre-stretch of the substrate (The FEM display is for a pre-stretch of 2.0). The color bar of ε_p^{\max} ranges (a) 0-0.94 and (b) 0-1.93.....21
- 2.4. The PB ruga-phase diagram: \bar{k} and ε denote the stiffness-ratio index, and the compressive strain respectively; the solid curve T_{12} and T_{13} represents equation (3); A ($\varepsilon_A = 0.35, \bar{k}_A = 1.44$) and B ($\varepsilon_A = 0.46, \bar{k}_A = 1.44$) signify the lower bound of the subcritical state of creasing, and the Biot instability point; (I) flat phase; (II) single-mode wrinkle phase; (III) limit phase of global crease localization; (IV) double-mode wrinkle phase; (V) quadruple-mode wrinkle phase; (VI) fold phase; (VII) limit phase of global fold localization; (IIc), (IVc) and (Vc) are three setback-crease phases; (Vcf) crease-fold phase; \bar{M}^+ ($\varepsilon = 0.32, \bar{k} = 1.20$), \bar{M}^- ($\varepsilon = 0.27, \bar{k} = 0.40$), D^+ ($\varepsilon = 0.24, \bar{k} = 1.00$), Q^+ ($\varepsilon = 0.22, \bar{k} = 0.60$), and $F^+(0)$ are five ruga-phase triple points.....23
- 3.1. The primary ruga-phase diagram: \bar{k} ; scaled stiffness ratio, ε ; compressive strain: (I) flat phase, (II) single-mode wrinkle phase, (III) global crease localization, (IV) double-mode wrinkle phase, (V) quadruple-mode wrinkle phase, (VI) fold phase, (VII) global fold localization, (IIc), (IVc) & (Vc); three setback-crease phases, (Vcf)

- crease-fold phase, A; subcritical crease strain limit, B; Biot critical strain of creasing, D_I^R ; M-period doubling limit, Q_I^R ; M-period quadrupling limit. The five colored regions represent irreversible ruga-phases.....34
- 3.2. Cooperative creasing irreversibility for $\bar{k} = 0.59, R = 15$. (a) $\Delta\Omega$ is the crease tips amplitude difference normalized by critical onset wrinkling wavelength. The normalization factor of the critical onset wrinkling wavelength by film thickness is shown at the bottom left corner of the table. Critical strains for wrinkling, doubling and creasing modal bifurcations are marked on the axis: $\varepsilon_W = 0.08$, $\varepsilon_D = 0.19$, $\varepsilon_C = 0.22$; $\varepsilon_1 = 0.24$, $\varepsilon_2 = 0.35$ and $\varepsilon_3 = 0.36$ are three particular strains which are chose for comparison of loading and unloading; (b) contour plot of loading and unloading FEM results for ε_1 , ε_2 and ε_336
- 3.3. Reversibility of the ruga modes on the surface of the bi-layer system without strain mismatch at the interface. $\Delta\Omega$ is the amplitude difference normalized by critical onset wrinkling wavelength. Reversibility is checked by plotting the traces, $\Delta\Omega^s$ and $\Delta\Omega^l$, of the vertical normalized amplitude difference between the period doubling valley and respectively the single mode valley and the quadrupling valley, as a function of the global nominal strain during a loading-unloading cycle. The normalization factor of the critical onset wrinkling wavelength by film thickness is shown at the bottom left corner of the table. (a) bilayer with modulus ratio $R = 90$ ($\bar{k} = 0.32$): the traces coincide during the loading-unloading cycle indicating reversibility of the ruga modes; (b) bilayer with modulus ratio $R = 3000$ ($\bar{k} = 0.10$):

- both DM2 and QM2 exhibit hysteretic behavior during unloading leading to mode locking; the FEM contour plots show the ruga phases under four specific compressive strains ε_1 , ε_2 , ε_3 and ε_4 during loading and unloading.....41
- 3.4. P-period switching irreversibility of PB with strain mismatch ($R = 10^5$ and pre-stretch ratio $\lambda_{ps} = 1.4$) during loading/unloading cycle: $\Delta\Omega$; amplitude difference normalized by critical onset wrinkling wavelength l , ε ; compressive strain, ($\Delta\Omega^s$, $\Delta\Omega^l$); normalized amplitude difference between shallow wrinkling valley and two neighboring deep valleys, Solid curves; loading (DM1 \rightarrow QM1 \rightarrow F), Dashed curves; unloading, P; critical point where shallow wrinkle valley becomes flat. (a) Unloading from M-period doubling (DM1 \rightarrow SM2). (b) Unloading from M-period quadrupling (QM1 \rightarrow DM2 \rightarrow SM2): (G^+ , R^+); unloading starting points of two quadrupling bifurcations, (G^- , R^-); points of excited-mode DM2, Black star; configuration of excited-mode SM2. (c) FEM contour plots of ruga evolution during a loading-unloading cycle: (c1, c3); primary modes through transition (SM1 \rightarrow DM1 \rightarrow QM1), c4; excited-mode DM2 during unloading by snap-buckling from QM1.....44
- 3.5. Vertical surface velocity of P-period switching: Upper curves of (a, b, d, e, f); velocity profile of a selected range marked by dashed red box in (c), Lower curves; corresponding surface profiles (Ω normalized by critical onset wrinkling wavelength l). (a) Unloading from QM1 to current DM1 with small viscosity. (b)

	Loading to current DM1: (d-f); unloading from QM1 to SM2 with viscoelastic loss tangent of 2×10^{-4}	50
3.6.	Schematics of ruga-modes on the surface of a neo-Hookean bilayer system, composed of a thin film with modulus μ_f and a deep substrate with modulus μ_s , subject to a loading-unloading cycle. (a) Three types of global ruga localization, crease, fold and ridge; (b) Mode transitions during the loading-unloading cycle, where solid and dashed arrows represent loading and unloading processes respectively, the bottom row shows ruga evolution pathway for a bilayer system during the loading segment of the cycle, (I) flat phase, (II) primary single-mode wrinkle phase SM1, (IV) primary double-mode wrinkle phase DM1, (V) primary quadruple-mode wrinkle phase QM1; the other ruga modes denoted by (SMi), (DMi) and (QMi), $i=2,4$, denote corresponding excited-modes observed in simulation during unloading; the dashed boxes represent other possible excited-modes that are not detected by our simulations.....	53
4.1.	Schematics of ruga formation with pre-stretch. Column (a) PB loading system with pre-stretch: (i) initial substrate configuration with length L , depth H and modulus μ_s ; (ii) stretched configuration with final length of $\lambda_{ps}L$; (iii) stress free film with modulus μ_f and thickness h is attached to the stretched substrate; (iv) loaded configuration. Column (b) investigation domain: \bar{k} denotes the normalized characteristic wavenumber; ε is the loading strain and λ_{ps} represents the substrate pre-stretch ratio. ε_f and ε_s axis are the measurements for film strain and substrate strain respectively. ε_s starts from the no stretch axis where the substrate is fully	

	released. The $\varepsilon_s = 0.35$ creasing plane and $\varepsilon_s = 0.46$ Biot plane is marked in the plot.....	58
4.2.	Ruga phase period control under pre-stretch effect. Column (a) crease period control; (a1) contour plot of every four valley crease for PB without strain mismatch ($R = 4.5, \bar{k} = 0.87, \lambda_{ps} = 1.0$); (a2) contour plot of every other valley crease for PB with strain mismatch ($R = 30, \bar{k} = 0.46, \lambda_{ps} = 1.2$); (a3) experimental results of every other valley crease; (a4) contour plot of every valley crease for PB with strain mismatch ($R = 30, \bar{k} = 0.46, \lambda_{ps} = 1.8$); (a5) experimental results of every valley crease. Column (b) fold period control; (b1) contour plot of every four valley fold for PB without strain mismatch ($R = 600, \bar{k} = 0.17, \lambda_{ps} = 1$); (b2) contour plot of every other valley fold for PB with strain mismatch ($R = 1000, \bar{k} = 0.14, \lambda_{ps} = 1.5$); (b3) experimental results of every other valley fold of a stiff skin formed on soft PDMS substrates [165].....	62
4.3.	Pre-stretch effect on creasing of equi-modulus bilayer. Column (a) represents the crease evolution sequence for homogeneous PB without substrate pre-stretch: (a_i) flat state; (a_{ii}) crease at $\varepsilon_s = 0.45$; (a_{iii}) crease growth at same strain. Column (b) illustrates the crease evolution sequence for equi-modulus bilayer with substrate pre-stretch $\lambda_{ps} = 2.0$: (b_i) single crease initiation at $\varepsilon_f = 0.36$; (b_{ii}) crease frequency multiplication at $\varepsilon_f = 0.50$; (b_{iii}) crease period multiplication and growth at $\varepsilon_f = 0.64$	65
4.4.	Wrinkle-ridge (I) and order-disorder (II) transitions under substrate pre-stretch. (a-c) shows difference morphological response for pre-stretch ratio $\lambda_{ps} = 1.8$ of	

various bilayer stiffness ratio R . (a) sequence of normal wrinkle evolution for $R = 18$ ($\bar{k} = 0.55$): (a_i) wrinkling phase at $\varepsilon_s = -0.52$, $\varepsilon_f = 0.16$; (a_{ii}) wrinkle growth at $\varepsilon_s = -0.22$, $\varepsilon_f = 0.32$; (a_{iii}) doubling wrinkle phase at $\varepsilon_s = 0.06$, $\varepsilon_f = 0.48$; (b) sequence of ordered-ridge evolution for $R = 60$ ($\bar{k} = 0.37$): (b_i) ridging at $\varepsilon_s = -0.53$, $\varepsilon_f = 0.15$; (b_{ii}) ridge frequency multiplication at $\varepsilon_s = -0.34$, $\varepsilon_f = 0.25$; (b_{iii}) secondary wrinkle at $\varepsilon_s = -0.17$, $\varepsilon_f = 0.35$; (b_{iv}) uniform period doubling at $\varepsilon_s = 0.10$, $\varepsilon_f = 0.45$; (c) order-disorder transition of ridging for $R = 600$ ($\bar{k} = 0.17$): (c_i) ridging at $\varepsilon_s = -0.67$, $\varepsilon_f = 0.07$; (c_{ii}) ridge frequency multiplication at $\varepsilon_s = -0.58$, $\varepsilon_f = 0.12$; (c_{iii}) onset of period multiplication $\varepsilon_s = -0.22$, $\varepsilon_f = 0.32$; (c_{iv}) disorder and coexistence ruga phases at $\varepsilon_s = 0$, $\varepsilon_f = 0.44$. (d) Phase diagram for wrinkle-ridge and order-disorder transitions: blue circles are data points have no ridging process during releasing; purple diamonds are data points for ridging with order transition; red triangles are data points for ridging with disorder transition; black curve denotes the critical moduli ratio ($1/R$) for ridging respect of substrate pre-stretch λ_{ps} ; red curve represents the boundary for order-disorder transition. The previous three cases (a), (b), (c) are marked in the phase diagram. The boundaries (I) and (II) represent loci of wrinkle-ridge (I) and order-disorder (II) transitions respectively.....67

- 4.5. Imperfection and film-modulus effects on wrinkle-ridge and order-disorder transitions. (a₁) shows the FFT plot of normal wrinkle evolution of bilayer system ($R = 60$, $\bar{k} = 0.37$, $\lambda_{ps} = 1.8$) with relative large imperfection amplitude; (a₂) shows the corresponding evolution sequence: (a_i) uniform wrinkling at $\varepsilon_s =$

	-0.57 , $\varepsilon_f = 0.13$, (a_{ii}) incipient ridging at $\varepsilon_s = -0.35$, $\varepsilon_f = 0.25$, (a_{iii}) suppression of ridging at $\varepsilon_s = -0.10$, $\varepsilon_f = 0.39$, (a_{iv}) uniform folded wrinkle at $\varepsilon_s = 0.14$, $\varepsilon_f = 0.52$. (b ₁) illustrates ridge order-disorder transition of bilayer system ($R = 60$, $\bar{k} = 0.37$, $\lambda_{ps} = 1.8$) with relative small imperfection amplitude; (b ₂) shows the corresponding evolution sequence: (b_i) ridging at $\varepsilon_s = -0.64$, $\varepsilon_f = 0.09$, (b_{ii}) ridge frequency multiplication at $\varepsilon_s = -0.33$, $\varepsilon_f = 0.26$, (b_{iii}) ordered ridge at $\varepsilon_s = -0.13$, $\varepsilon_f = 0.37$, (b_{iv}) disordering and co-existent phases at $\varepsilon_s = 0.08$, $\varepsilon_f = 0.49$. (c ₁) shows the order-disorder transition of bilayer system ($R = 600$, $\bar{k} = 0.17$, $\lambda_{ps} = 1.8$); (c ₂) shows the corresponding evolution sequence: (c_i) ridging at $\varepsilon_s = -0.67$, $\varepsilon_f = 0.07$, (c_{ii}) ridge frequency multiplication at $\varepsilon_s = -0.34$, $\varepsilon_f = 0.25$, (c_{iii}) ordered ridge at $\varepsilon_s = -0.19$, $\varepsilon_f = 0.34$, (c_{iv}) disordering at $\varepsilon_s = 0.10$, $\varepsilon_f = 0.39$	74
4.6.	Order-disorder transitions of 2D ruga: simulation and experiment. (a_i^t) to (a_{iii}^t) shows the top view of 2D ruga evolution under compressive loading; (b_{iii}^t) is the experimental comparison for (a_{iii}^t) , shows SEM micrograph of the wrinkle patterns on PDMS substrates with amorphous carbon deposition time $t = 30$ s; (a_{ii}^c) and (a_{iii}^c) are the corresponding cross section view for (a_{ii}^t) and (a_{iii}^t) ; (b_{ii}^c) and (b_{iii}^c) are the experimental cross section comparison [10] for (a_{ii}^c) and (a_{iii}^c) , showing FIB cross-sectional image of an amorphous carbon film on PDMS with different deposition times.....	83
5.1.	Experimental setup. (a) Manufactured self-tightening loading device: (A) base plate, (B) grip pair, (C) translational stage, (D) actuator, (E) control module; (b)	

	exaggerated view of grip design; (c) loading device fit in UV light chamber.....	88
5.2.	Ruga patterns on a pre-stretched oxidized PDMS surface detected by regular optics. The magnification rate increases from (a) to (d).....	90
5.3.	Ruga shape observed by interference microscope Zygo. (a) top view of ruga stripes; (b) interference fringes of scanned region; (c) oblique view of (a); (d) the amplitude and wavelength measurement of the ruga patterns.....	93
5.4.	AFM measurements of Young's modulus of the oxidized PDMS as a function of depth from the free surface. A, C: a contour plot of the contact stiffness along the fractured surface of the sample as measured by AFM; B, D: corresponding Young's modulus as a function of depth from the free surface [4].	94
5.5.	Multi-layer structure simulation to mimic oxidized PDMS at substrate pre-stretch ratio $\lambda_{ps} = 2.0$. (a) the schematics of modulus and thickness distribution of the finite element model; (b1) Ruga state at strain of $\varepsilon_f = 0.135$, $\varepsilon_s = -0.730$; (b2) is the zoomed in figure of the valleys in (b1); (c1) Ruga state at strain of $\varepsilon_f = 0.355$, $\varepsilon_s = -0.290$; (c2) is the zoomed in figure of the valleys in (c1); (d1) Ruga state at strain of $\varepsilon_f = 0.356$, $\varepsilon_s = -0.288$; (d2) is the zoomed in figure of the valleys in (d1); (d*) the experimental verification of (d1); (e) folded ruga during further compression $\varepsilon_f = 0.622$, $\varepsilon_s = 0.244$; (e*) the experimental verification of (e).....	97
5.6.	AFM measurement of hierarchical wrinkles on oxidized PDMS surface and its comparison with FEM results. (a) scanned region of PDMS surface ($5 \mu m \times 5 \mu m$); (b) FEM result of multi-layer film/ substrate with kinked modulus	

distribution under substrate pre-stretch $\lambda_{ps} = 2.0$; (c) exaggerated view of the large wrinkle valley from the dotted box in (b); (d, e) comparison of simulation with AFM measurement: (d) shows the exaggerated view from the dotted box in (c) under certain shrinkage amount to fit with (e); (f) the corresponding amplitude data of measurement in (e).99

Chapter 1

Introduction

1.1. Briefing on “Ruga Mechanics”

Surface morphologies such as wrinkles, creases, folds, ridges, wrinklons, crinkles and crumples on the surface of a solid, including those for a thin film on a substrate, are collectively referred to as rugae states. ‘Ruga’, a Latin term, means a single state of various corrugated material configurations. While rugae (plural of ruga) in Latin originally meant variety of corrugated configurations, it has been narrowly used in anatomy. Studies of ruga formations are of fundamental importance to a broad range of applications including flexible electronics [26], strain-controlled superhydrophobicity [30], bio-inspired adhesion devices [29], self-assembled patterns [161], biological tissues [39, 105], brain science [35-37], geo science [40-43].

Surface instabilities of a soft material are elicited under certain conditions and reflect themselves by different surface corrugations with distinct ruga features. Ruga structures are widely observed in Nature and research works (Fig. 1.1). If we classify the soft material systems by the formation process of their surface pattern, there are generally two types: deformation ruga system and growth induced ruga system. Surface patterns of the former one manifest under applied external load or mechanical excitation; the latter one exhibits ruga patterns primarily caused by material deposition processes. Deformation ruga have been found in experiments as shown in experiments as shown in Fig. 1.1(b-d).

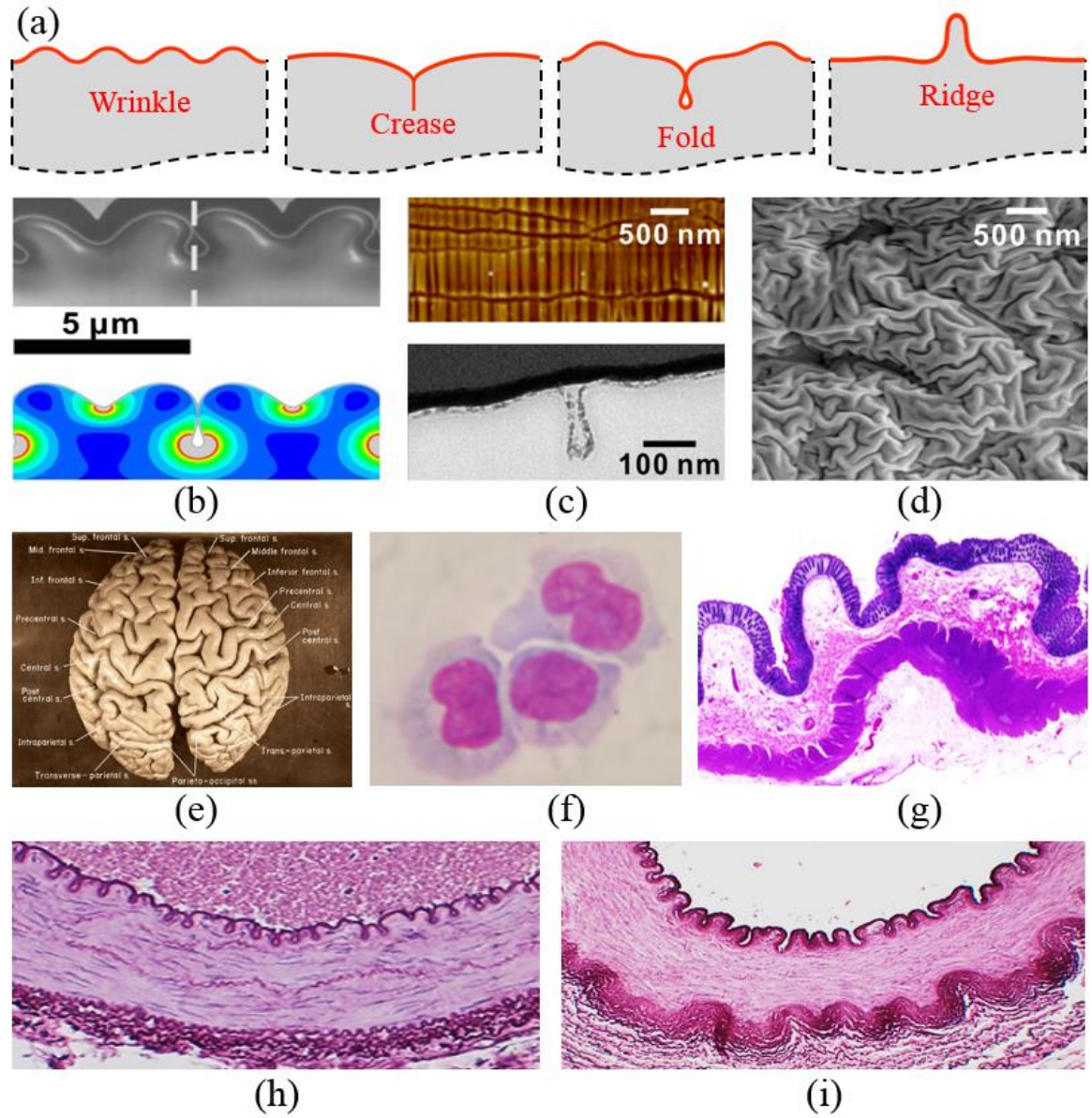


Figure 1.1. Ruga phases in nature and engineered materials: (a) schematics of ruga phases in 1D structure; (b) 50nm gold film folds: blue-red: 0-2 MPa Mises stress [5]; (c) graphene folds, on PDMS (top and side views) [77]; (d) 2D ruga pattern on 10 nm ion beam implanted DLC on PDMS [158]; (e) the cortex structure of Einstein's brain (discover magazine); (f) interface crease in proliferation and differentiation of hematopoietic cells: Morphology of U937 and HL-60 cells stimulated with Phyco-CM and others [171]; (g)

ridge, crease patterns observed on colon [172]; (h) folds on muscular artery wall [172]; (i) ridges and ridge folds on mesenteric artery wall [172].

Growth induced ruga is commonly observed in nature especially in bio-systems. Fig. 1.1(e-i) reveal various ruga patterns in organisms carried out by tissue growth. Different tissue types shows diverse ruga formations such as highly localized crease on the cortex structure of human brain (e); interface creasing of a blood cell during the differentiation process (f) or ridge fold on artery wall (h, i). These ruga patterns vary with distinct physical properties of the tissue, strain mismatch distribution of the layers, tissue global deformation and other control factors. From the examples, the large diversity of the soft structure categories leads to various surface morphologies, which motivates our research on exploring possible ruga patterns and their formation mechanisms.

In this thesis, we aim to solve the following questions systemically: (i) How many ruga states can we observe with different soft material system? (ii) Under what conditions could one surface instability evolve to another? (iii) How to control the ruga morphologies through designing soft structure system? Before going deep to investigate these questions, we summarized the current studies of different ruga types classified by their morphological features.

1.2. Studies on major ruga phases and their transitions

Since the references on major ruga phases are extensive, we, M. Diab, R. Zhao and K. S. Kim, summarized the status of the study on a blog of Imechanica [173], and here in this section, the content from the online source is quoted.

“Ruga configurations have distinct geometrical characteristics, and each of them stands for an energetically *monomorphic* equilibrium configuration representing a single phase of ruga. Over the past half century important ruga phases have been identified – Biot for wrinkle[1], Gent and Cho / Hohlfeld and Mahadevan / Hong, et al. for crease [2, 72-74], Brau, et al. for period multiplication [3, 4], Sun, et al. and Pocivavsek, et al. for fold [5, 6], Cao and Hutchinson for ridge [7], Bowden, et al. for 2D wrinkles [8], Efimenko, et al. for hierarchical wrinkles [9], Ahmed, et al. for 2D ruga tessellation [10]. Diab, et al. recently constructed a comprehensive ruga phase diagram of a stiff surface boundary layer in a neo-Hookean solid [11, 12]. They showed that, similar to conventional *material phase transitions* for which a thermodynamic potential typically depicts the behavior, *ruga phase transitions* are naturally described by bifurcation analysis with a mechanical (structural) potential. Construction of iso-periodic [11, 12] and self-selective *ruga phase diagrams* [13] will not only enable analysis for coexistence, scaling or localization of multiple ruga phases, etc., but will also provide understanding on meso-scale self-organizing mechanisms that can be controlled by large-scale field parameters.

1.2.1. Wrinkle

Over the past several decades, mechanics research revealed that wrinkle has the following primary characteristics: 1) critical wavelength and critical strain, 2) distinct material property dependence, 3) weak imperfection sensitivity and stable amplitude growth. The research provided relatively simple relation among the critical wavelength, stiffness ratio and thickness. However, dependence of the relationship on material properties of the film and the substrate, and loading conditions including pre-stretch and finite deformation has been steadily and extensively investigated [1, 42, 44-64]. While the

onset criticality of the wrinkling was analyzed by first-order perturbation, growth rate of the wrinkle amplitude and imperfection sensitivity of the criticality required higher-order-perturbation post-buckling analysis typically with the Koiter method [11, 12, 65-69]. The wrinkle characteristics of weak imperfection sensitivity and stable amplitude growth have been attractive features of wrinkle for experimental measurement of the property of the film relative to that of the substrate or vice versa [70, 71]. In addition, hierarchical wrinkles with their frequencies clustered in broad scales have been observed, and cause of the clustering has been debated [4, 9].

1.2.2. Crease

In contrast to wrinkle, crease has other three distinct characteristics: localization of deformation, snap buckling with strong imperfection sensitivity and global irreversibility of deformation. It was first theoretically predicted by Biot [1, 45] that a homogenous Neo-Hookean half space is susceptible to surface wrinkling under a compressive strain exceeding 0.46. Subsequently, surface creasing were captured experimentally at a compressive strain about 0.35 ± 0.07 in Neo-Hookean materials [2], and it was later proven theoretically and numerically that there indeed exists a critical compressive strain for creasing at 0.35 [72, 74, 75]. The critical strain for creasing has also been shown via finite element (FEM) simulations with a pre-pinching method [73]. Later, Diab et al., [11, 12] uncovered that the crease localization is caused by cascade instability either from a fundamental state (instantaneous crease) or from a wrinkle state (setback crease). For the second aspect, a series of investigations [72-76] revealed that snap buckling of creasing is a consequence of bifurcation onto a branch of solutions extended from a subcritical state to a supercritical state. For the third aspect, the global irreversibility exhibits hysteresis in

loading and unloading despite that the local deformation is elastic (reversible) everywhere [12, 74]. In addition, it is found that creasing is sensitive to imperfections [69].

1.2.3. Fold

When wrinkle amplitude grows large, the wrinkles often form folds with high amplitude aspect ratio for self-contact, period multiplication of the wrinkle to set the fold periodicity, and subsequently leads to fold localization. Here, high amplitude aspect ratio means the amplitude of the wrinkle is much larger compared to its wavelength. The folds have attractive features for nano-manufacturing of surface nanostructures such as subsurface nano channels. Diverse characteristics of folding processes have been observed and investigated by several research groups. Those include folding of an elastic sheet floating on water [5], period multiplication of a wrinkle on a bilayer system [3], formation of periodic folds [6], folding of a graphene sheet on a PDMS [77], etc. The role of substrate nonlinearity in the post-buckling evolution of wrinkle has been revealed numerically by Sun, et al. [6] for fold, and further investigated by Hutchinson [68] and Zhao, et al. [13]. However, a quantitative characterization of the critical conditions for the large amplitude wrinkle evolution is still elusive due to lack of analytical expressions of the wrinkle configuration with nonlinear finite deformation at the onset of period multiplication. Once the wrinkle surfaces make self-contacts for folding, some selective fold tips begin to advance into the substrate with a series of unfolding of nearby folds, leading to fold localization.

1.2.4. Ridge

Ridge is a ruga phase of localized bulge that exhibits mechanical characteristics similar to those of crease for localization and irreversible mode of hysteresis behavior. It is typically observed in a surface layer compressed by releasing a large pre-stretch strain. For example, depending on the level of pre-stretches of an incompressible neo-Hookean substrate, the wrinkle generally bifurcates to a single isolated ridge followed by development of periodic ridges through frequency multiplication followed by period multiplication. Ridges are formed through snap buckling and the configurational evolution is irreversible in general. Ridges often grow into ridge-folds at large compression of the film. ([13, 32, 69, 78, 79])

1.2.5. Delamination ruga

Delamination ruga develops when a thin surface-mounted film with a relatively weak interface is laterally compressed to be debonded. Blistering and telephone cord buckling of a thin film mounted on a stiff substrate were extensively studied in 1990s. In contrast, when a stiff film is delaminated through wrinkling on a soft substrate, the delamination process develops localized delamination ridges. The delamination ridges often transforms into delamination folds under large strain mismatch, typically observed in CVD grown films of graphene caused by large thermal strain mismatch. Isolation of bending localization on the debonded part of the film has attracted attention for potential use of delamination ruga in flexible electronics applications. Recently a delamination ruga phase diagram was proposed. ([80-86])

1.2.6. Two-dimensional Ruga

Experimental observations of various 2D ruga phases such as periodic checkerboard, herringbone, labyrinth, crease and fold have been reported [8, 87-93]. Recently Ahmed et al., [10] showed that for a strain larger than 0.30 the folds evolve in random orientations to create asymmetric disordered tessellation. Wrinkle instability of hyper-elastic half space under general biaxial compression was studied by Nowinski [94], and Usmani and Beatty [95]. However, it was not until recently that the community started to investigate the formation of the various 2D ruga phases of bilayer systems using numerical and/or analytical approaches [55, 96-105]. Most all of these studies haven't considered the full sequential bifurcations of the various patterns at large strains. Many issues are still unexplained such as the disordered tessellation observed in [10], the labyrinthine pattern, mode jumping, coexistent of states, and the role of imperfections on the formation of the ruga patterns. More efforts are needed to develop analytical and numerical tools that are capable of handling the formation of the complex 2D ruga phases and transitions among them.”

1.3. Methodology and approaches

The studies in this thesis are mainly carried out by finite element analysis (FEA) using commercial software package ABAQUS standard. FEA is a robust computational technique to solve complicated partial differential equations with specific boundary conditions. It plays an important role in predicting material behavior especially when the problems are subject to highly nonlinearity and large deformation, analytical solutions for such kind of problems are very difficult to achieve. All of the computational results

presented in following chapters are subject to implicit simulations. The constitutive law we used here to simulate soft material is hyperelastic solid. We assume the material follows neo-Hookean representation, which has the strain energy expression of

$$W = \frac{\mu}{2} \sum_{i=1}^3 (\lambda_i^2 - 3), \quad (1.1)$$

where μ is the shear modulus of the material and λ_i are the principal stretches. The material is considered to be incompressible throughout the simulations in this thesis.

In the meantime, experiments are done to verify some of the computational results. Microscopy with different resolutions such as general optics, interference microscope and atom force microscope are used to observe morphological Ruga deformation at various length scale.

1.4. Outline of the thesis

In this thesis, we will investigate the ruga evolution of different soft material systems. This thesis consists of six chapters and is organized as follows.

Chapter 1 gives a general introduction to the ruga mechanics including the possible ruga phases that have been observed in nature and recent studies and their potential applications. The remaining issues and unsolved problems in this field are listed. Methods that used to investigate the problems throughout this thesis are also presented in this chapter.

Chapter 2 is about developing the ruga phase diagram for a primary bi-layer system with no strain mismatch between the film and substrate. Possible ruga phases, evolution pathways and their corresponding triggering strains for this specific system are pointed out

in the phase diagram. Three types of creasing of a bi-layer system: instantaneous creasing, wrinkle set-back creasing and the substrate localization creasing are delineated. The higher instabilities for stiff film system such as period doubling and quadrupling are discussed together with their strain universality.

Chapter 3 follows the primary ruga phase diagram from the previous chapter. We investigated the irreversibility of various ruga phases under particular conditions such as substrate pre-stretch and viscosity. The localization irreversibility and modal irreversibility of various ruga-phase transitions are analyzed based on the surface deformation behavior during cyclic loading. We also predict the possible excited ruga modes triggered by modal irreversibility.

Chapter 4 takes the substrate pre-stretch into fully consideration and explores the mechanism of ridging. We studied the strain mismatch effect in determining ruga phase periods with respect of the modulus ratio of the bi-layer system. The mobility of ridge is investigated through the loading process. The relationship of symmetry breaking of ridges and its mobility bifurcation is discussed in this chapter. Concept of the order-disorder transition of ruga phases is firstly brought into this field.

In Chapter 5, we study and summarize the ruga control aspects and their corresponding control factors. A specific example of ruga transition suppression---ridging suppression is shown experimentally through a loading test of a PDMS with oxidized top surface and strain mismatch. Simulation of a multi-layer soft structure is carried out to verify the experimental observation. The ruga distribution control is illustrated by presenting the hierarchical wrinkles by microscopes with different resolution levels.

Chapter 6 generally concludes the entire thesis including the major observations and discussions. The ongoing work and future perspectives of ruga mechanics are also pointed out in this chapter.

Chapter 2

The Primary Bilayer Ruga-Phase Diagram I: Evolution of Multi-mode Wrinkles, Folds and Creases ^[13]

2.1. Introduction

Over the past several decades, a series of analyses on solid-surface deformation under in-plane compression have revealed diverse characteristics of one dimensional (1D) ruga structures – various 1D corrugated patterns of solid surfaces, and their transitions [1-3, 6, 72, 69]. In particular, a bilayer system generates relatively simple generic ruga phases with a single characteristic ruga wavenumber. The ruga phases include single- as well as multi-mode wrinkles, creases, folds and ridges. Morphological characteristics of the ruga phases are often found useful for various technological applications [25, 26, 29, 30]. Moreover, study of ruga phase transitions helps understand formation processes of various biological and geological ruga structures [105, 43]. In addition, fine control of self-organizing ruga phases will enable us to create advanced materials of unprecedented properties by folding 2D material structures [111]. To this end, here, we investigate formation conditions of various 1D ruga phases, and criteria on their stabilities, localization, and co-existence of multiple phases by constructing a ruga-phase diagram of a soft-substrate bilayer system.

A bilayer system of an elastic thin film on a soft elastic substrate develops a variety of ruga phases when compressed laterally and/or experiences growth of mismatch strain between the film and the substrate. Collection of the ruga phases on a plane of the characteristic ruga wavenumber (or elastic stiffness ratio) versus the compressive strain of the film represents a *ruga-phase diagram* [11, 12, 85]. Similar to the phenomenological description of a conventional *material phase diagram* in terms of its minimum free energy for various equilibrium phases [162], collection of monomorphic ruga configurations in equilibrium under well-defined constraints can constitute a *ruga-phase diagram*. While the material phase transitions can be rightly described by the Ginzburg-Landau theory [163], the ruga-phase transition is typically analyzed by bifurcation theories such as the Koiter theory [65, 67].

In this chapter, we only consider the most basic bilayer – an infinite-span film on a half-space substrate, both incompressible neo-Hookean, among diverse combinations of film/substrate geometries and elastic properties, as a primary bilayer (PB). Furthermore, we limit our ruga analyses to PB's without mismatch strain (or substrate pre-stretch), for various stiffness ratios, by tracing ruga evolution caused by plane-strain compression up to complete ruga localization at the Biot strain of 0.46. When a PB is gradually compressed, the film first buckles to generate a periodic wrinkle or crease, depending on the relative film stiffness to the substrate; a stiff film wrinkles and a soft creases. Hutchinson [68] analyzed the role of nonlinear substrate elasticity on 1D PB wrinkling under general biaxial stretch of the substrate; he also got the critical stiffness ratio and strain for wrinkle instability, employing the Koiter method [65, 67]. The PB-buckling period in undeformed reference configuration sets the characteristic ruga wavenumber.

In general, uniaxial ruga wavenumber of a deep-substrate bilayer depends on the stiffness ratio and the film span, when normalized by the film thickness. However, the normalized characteristic wavenumber of PB is governed only by the stiffness ratio. In particular, the dependence of the normalized characteristic wavenumber on the stiffness ratio is reduced to a simple formula [6, 7, 68],

$$\bar{k} = 2\pi h/L = \left(3\mu_s/\mu_f\right)^{1/3}, \quad (2.1)$$

for $\mu_s/\mu_f \ll 1$, where L is the wavelength, and μ_s and μ_f the shear stiffness of the substrate and the film respectively. Here, equation (2.1) represents not only the stiff-film limit wavenumber of a PB but also a convenient *stiffness-ratio index* of the PB. Then, all possible ruga phases of PB's can be displayed on a compact bound plane of (ε, \bar{k}) , where ε represents the compressive strain applied on the PB; the display is the *PB ruga-phase diagram*.

While a ruga-phase diagram can be constructed for absolute minimum energy configurations [85], here, we build the PB ruga-phase diagram by following ruga evolution under monotonic compression, employing extensive finite element analyses. Then, we can readily see ruga localizations, irreversible ruga transitions and substrate pre-stretch (or mismatch strain) effects on the PB ruga-phase diagram. We present studies of ruga localizations in this chapter, while analyses of irreversible ruga transitions and substrate pre-stretch effects on ruga formations are reported in the following chapters.

2.2. Ruga evolution leading to global ruga localization

A stiff film on a soft substrate has intrinsic characteristics of wrinkling at a small compressive strain [48]; on the other hand, the soft substrate by itself has intrinsic characteristics of creasing at a large compressive strain [2, 72, 73]. Wrinkling typically

disperses distribution of the film stress into the substrate, while creasing has tendency to localize surface deformation. Therefore, interaction between the film and the substrate deformation characteristics creates various ruga phases evolving from wrinkle initiation to global crease-like fold localization when compressed up to a large strain. The ruga phases of the PB system include not only single-, double- and quadruple-mode wrinkles, but also multiple-mode film creases, fold and ridge, leading to global crease, fold and ridge localizations.

Fig. 2.1a shows a schematic of a PB under lateral compression, which undergoes various ruga evolution pathways (Fig. 2.1b) to reach global ruga localizations (Fig. 2.1c). A soft film but stiffer than the substrate is typically observed in biological systems, and such a film often creases periodically, which eventually leads to a global crease localization under further compression [105]. In contrast, a very stiff film on a soft substrate is typically used in advanced engineering applications, and the film generally folds before it develops a global localization under large compression [6]. Compression with very large substrate pre-stretch causes ridge localization [69]. Now, we have the following questions. How stiff must a soft film be, relative to the substrate, not to crease upon lateral compression? What are the critical compressive strains for mode doubling and quadrupling of the characteristic wrinkle of a bilayer system? Can we have mode transitions of film-crease in a PB system, similar to the wrinkle folding process? What are the critical compressive strains for the onsets of global ruga localizations? How are the critical values influenced by a substrate pre-stretch (or mismatch) strain? These questions are answered by constructing the primary ruga-phase diagram in this and following chapters.

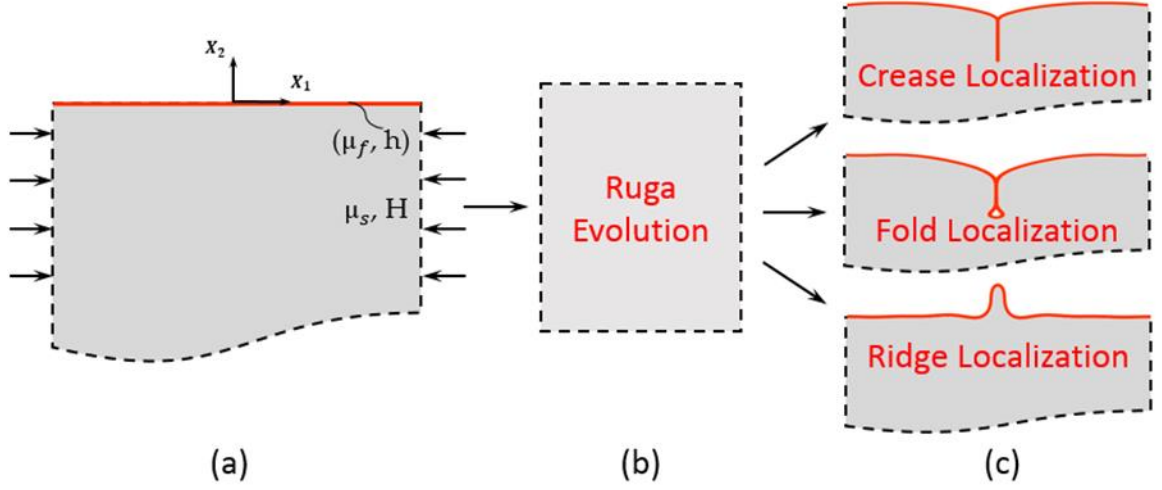


Figure 2.1. Schematics of ruga localizations in PB systems: (a) A PB composed of a neo-Hookean thin film with thickness and shear modulus under lateral compression; (b) various ruga phases in ruga evolution; (c) three types of global ruga localization.

2.3. Computational analysis of ruga localization

Finite element method (FEM) is used to implement the simulations of ruga phase evolution and associated plane-strain deformation in the PB system under lateral compression, employing the standard FEM package ABAQUS. The incompressible neo-Hookean constitutive model is adopted for both the film and substrate with different shear moduli. The length of the simulation sample is set to be L in X_1 direction and H in the X_2 direction. The initial length of the sample is set to be at least four times of the critical wavelength of wrinkling in the film-substrate system to ensure that relevant phenomena (e.g., period quadrupling) can be observed in the simulation. To mimic a semi-infinite substrate, the aspect ratio (depth to length) of the sample is set to be 20 (i.e., $H=20L$).

Prior to compression, a small sinusoidal perturbation in displacement in the X_2 direction is applied to the film surface to probe any instability in the system. The expression for this perturbation is written as

$$u_2 = \zeta \cos(8\pi X_1/l), \text{ for } -\frac{L}{2} \leq X_1 \leq \frac{L}{2}, \quad (2.2)$$

where L and l denote the film span and the characteristic wavelength of the PB system, respectively; the perturbation amplitude ζ should be small enough to ensure the accuracy of simulation, and is taken to be $\zeta/l = 0.0005$. The characteristic wavelength, l , for general PB is given by [12, 68].

In the FEM model, hybrid elements CPE4RH are used to simulate the incompressible neo-Hookean material, and periodic boundary condition is applied at both lateral faces. The span of the film, L , is varied for $L = 4nl$, $n = 1, 2, \dots, 5$ to test model-size sensitivity of various critical strains in ruga evolution. A self-contact interaction with the type of frictionless and “hard contact” is applied to the film surface to avoid penetration during creasing and folding deformations. The onset strains of ruga-phase transitions are identified by Fast Fourier Transform (FFT) with the criticality-identification method introduced in [11]. The stiffness-ratio index, \bar{k} , expressed in (2.1) ranges from 1.44 to zero, corresponding to the limiting case of a homogeneous solid ($\mu_s = \mu_f$) and an extremely stiff substrate ($\bar{k} = 0$). The stiffest film simulated is 10^4 times stiffer than the substrate.

2.4. Results and discussions: The PB ruga-phase diagram

The extensive FEM simulations reveal that the PB system has four distinct ruga evolution pathways to global crease localization, one pathway to global fold localization, and another to global ridge localization. The ridge localization requires pre-stretch of the substrate, and the post ridge localization behavior is quite different from those of crease or fold localization. The critical strains of ruga-phase transitions identified by FEM are insensitive to the modeling span of the film for $L = 4nl$, $n = 1, 2, \dots, 5$.

2.4.1. Global crease localization

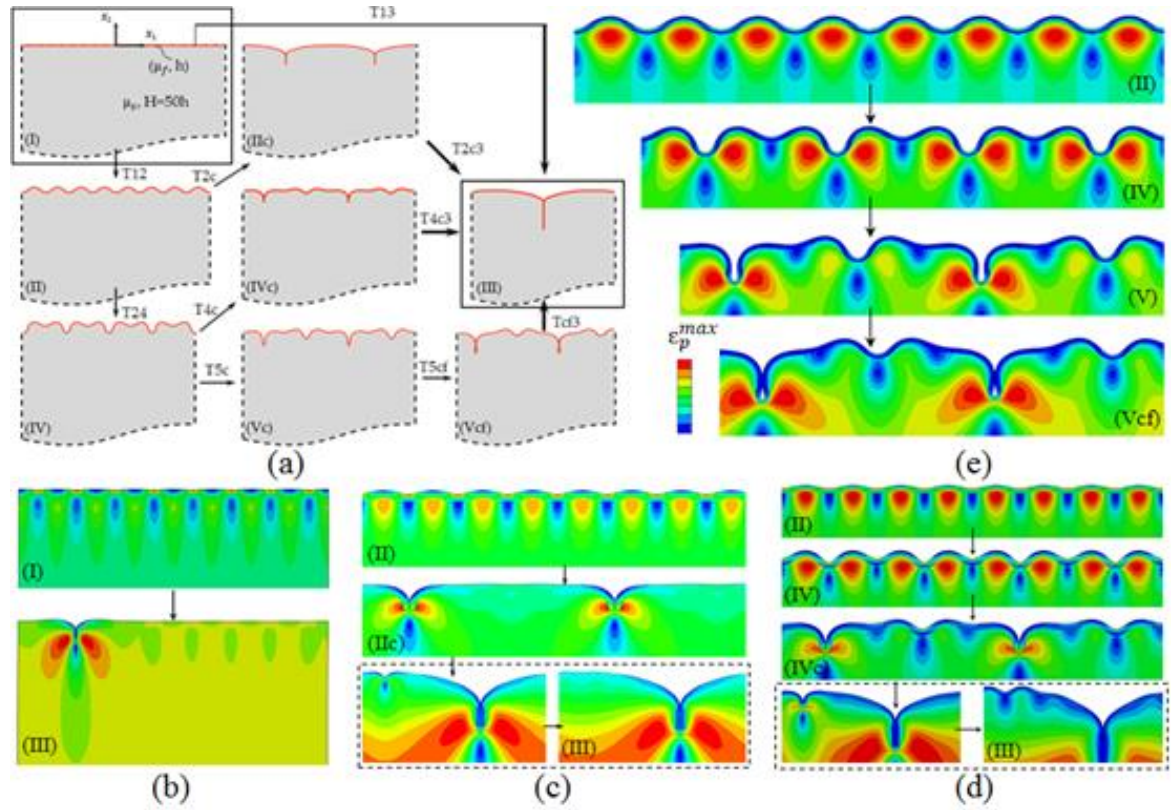


Figure 2.2. Pathways to global crease localization of soft-film bilayers: (a) schematics of four different pathways to global crease localization; FEM simulation plots of the

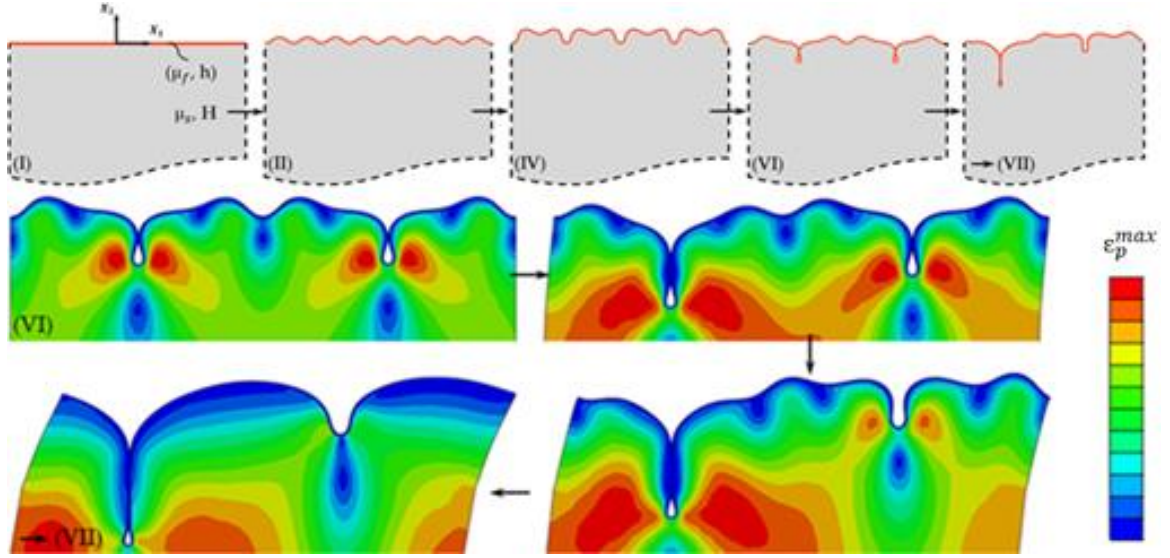
maximum principal nominal strain, ε_p^{\max} , for (b) instantaneous crease ($\bar{k} = 1.44$); (c) wrinkle – film crease – global crease localization ($\bar{k} = 1.00$); (d) wrinkle – double-mode wrinkle – quadruple-mode crease – global crease localization ($\bar{k} = 0.87$); (e) wrinkle – double-mode wrinkle – quadruple-mode wrinkle – quadruple-mode wrinkle-tip crease – quadruple-mode crease-fold – global crease localization ($\bar{k} = 0.41$): Frames in the dotted box of (c) and (d) show final localization processes in a different scale. The color bar of ε_p^{\max} ranges (b) 0-1.13, (c) 0-0.94, (d) 0-1.06 and (e) 0-0.77.

Fig. 2.2(a) shows schematics of the four different ruga evolution pathways heading towards the limit phase of global crease localization (III). The first pathway is instantaneous film crease which directly leads to the global crease localization (III) from the flat phase (I), for a very low film-stiffness ratio (or high stiffness-ratio index; $1.20 \leq \bar{k} \leq 1.44$) of the bilayer. The second pathway is setback crease of the film, (I) \rightarrow wrinkle (II) \rightarrow wrinkle-crease (IIc), which leads to the global crease localization (IIc \rightarrow III), for $0.80 \leq \bar{k} \leq 1.20$. The setback film crease has the wavenumber of $k_w/4$ where k_w is the wrinkle wave number; in other words, the period of the film creasing is quadruple of the primary wrinkle period. The quadruple-period creasing is believed due to the reason that it is necessary to amplify local strains at wrinkle valleys to the level of the Biot critical strain of 0.46 and to have sufficient energy release for unstable crease growth at every fourth valleys. The third pathway is mode doubling of the wrinkle (IV) followed by setback crease (IVc) which leads to the global crease localization (III), for $0.60 \leq \bar{k} \leq 0.80$. Again, the period of the film creasing is quadruple of the primary wrinkle period. The fourth

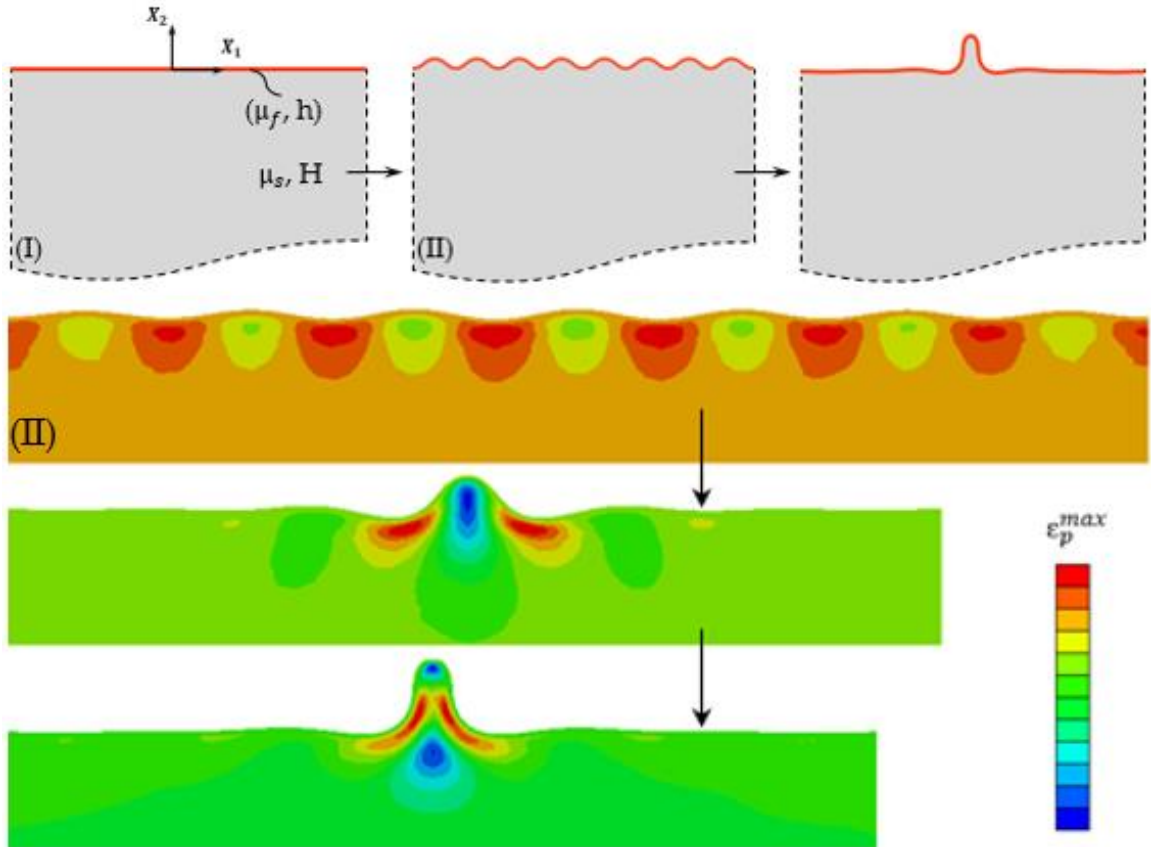
pathway is the setback crease (Vc) following wrinkle period doubling and quadrupling (V), which develops folds with crease tips (Vcf) before they proceed to the global crease localization (III), for $0.40 \leq \bar{k} \leq 0.60$. The fold period is also quadruple of the primary wrinkle period. While the initial quadruple crease and fold localizations are the most probable localization mode for a very large film span, it is also possible to have non-quadruple localizations for small film spans of $L = 4nl$ with non-integer n 's.

Fig. 2.2(b-e) show FEM generated ruga configurations of typical 1st ($\bar{k} = 1.44$; homogeneous half space), 2nd ($\bar{k} = 1.00$), 3rd ($\bar{k} = 0.87$) and 4th ($\bar{k} = 0.41$) pathways leading to a global crease localization, together with associated maximum principal nominal strain, ε_p^{\max} , distributions in the cross-section of the bilayer. Fig. 2.2b shows that the global crease localization (III) is made by relaxing periodic strain concentrations of initial perturbation (I), in the first evolution pathway. Similarly, Fig. 2.2c displays that the film wrinkles first (II), and every four other valleys of the wrinkle make setback creases in expense of relaxing three other wrinkle valleys (IIc). Then, the global crease localization (III) is achieved by releasing the periodic setback film-creases, in the second evolution pathway. Fig. 2.2d exhibits that the film forms a single-mode wrinkle (II), followed by transforming to a double-mode wrinkle (IV), and then creases in every fourth valleys of the primary wrinkle period (IVc) before it progresses to the globally localized crease (III), in the third pathway. Fig. 2.2e presents that the film forms a single-mode wrinkle (II), transforms to a double-mode wrinkle (IV), then to a quadruple-mode wrinkle (V) where all the deep valleys crease (Vc) before the creasing valleys fold (Vcf), in the fourth pathway. The crease fold eventually reaches the limit phase of global crease localization upon further compression.

2.4.2. Fold and ridge localizations



(a)



(b)

Figure 2.3. Pathways to global localization of stiff-film bilayers: (a) global fold localization with pathways of wrinkle – double-mode wrinkle – quadruple-mode wrinkle – fold – global fold localization (The FEM frame display is for $\bar{k} = 0.17$); (b) global ridge localization caused by pre-stretch of the substrate (The FEM display is for a pre-stretch of 2.0). The color bar of $\bar{\epsilon}$ ranges (a) 0-0.94 and (b) 0-1.93.

The first row of Fig. 2.3(a) shows schematics of the ruga evolution pathway of global fold localization through wrinkling (II), mode doubling (IV), mode quadrupling (V), and folding (VI), to get to the limit phase of global fold localization (VII), as compressive strain increases for $0.0 < \bar{k} \leq 0.40$. When the film is approximately 47 times or more stiffer than the substrate ($0.0 < \bar{k} \leq 0.40$), the film of the PB without substrate pre-stretch does not crease; instead, it folds in every four other wrinkle valleys after mode quadrupling of the wrinkle. The subsequent two rows of Fig. 2.3a show four FEM-generated ruga configurations in the process of global fold localization from the periodic folds (IV) for a stiff film ($\bar{k} = 0.17$). The four frames of the localization process show that the localizing fold tip penetrates deep into the soft substrate in expense of opening other nearby folds.

If the substrate is pre-stretched beyond the stretch ratio of approximately 1.5, the film develops a global ridge localization instead of a global crease or fold localization, as shown in Fig. 2.3b. The first row of Fig. 2.3b shows schematics of the ridge localization; the film wrinkles first, and then a ridge localizes in expense of unloading the wrinkles away from the localized ridge, as shown in the subsequent rows. However, unlike a global crease or a fold localization, growth of the ridge height has a limit upon further compression. Beyond the ridge-localization limit strain, multiple ridges begin to form and the ridge-

subcritical state of creasing, and the Biot instability point; (I) flat phase; (II) single-mode wrinkle phase; (III) limit phase of global crease localization; (IV) double-mode wrinkle phase; (V) quadruple-mode wrinkle phase; (VI) fold phase; (VII) limit phase of global fold localization; (IIc), (IVc) and (Vc) are three setback-crease phases; (Vcf) crease-fold phase; \bar{M}^+ ($\varepsilon = 0.32$, $\bar{k} = 1.20$), \bar{M}^- ($\varepsilon = 0.27$, $\bar{k} = 0.40$), D^+ ($\varepsilon = 0.24$, $\bar{k} = 1.00$), Q^+ ($\varepsilon = 0.22$, $\bar{k} = 0.60$), and F^+ ($\varepsilon = 0.24$, $\bar{k} = 0.60$) are five ruga-phase triple points.

The black dots on the ruga-phase diagram represent critical points of wrinkle bifurcation identified by FEM analyses. The ruga-phase boundary T_{12} delineates the wrinkle phase (II) from the flat phase (I). The wrinkle-bifurcation boundary T_{12} indeed approaches the theoretical prediction $\bar{k} = 2\sqrt{\varepsilon}$ for $\varepsilon \ll 1$, i.e. for a very stiff film. The solid curve for T_{12} and T_{13} in Fig. 2.4 is a plot of

$$\bar{k} = 2(1 + 0.15\varepsilon)\sqrt{\varepsilon}. \quad (2.3)$$

The FEM results are closely represented by equation (2.3) for the entire range of $0 \leq \varepsilon \leq 0.46$ up to the Biot critical strain. Here, the stiffness-ratio index, \bar{k} , is not close to the actual wrinkle wavenumber \bar{k}_w , not exceeding 0.60, for compliant films ($0.30 < \bar{k}$). The formula for the actual wavenumber \bar{k}_w of the PB can be found in reference [12, 68]. Here, ‘B’ at $\varepsilon = 0.46$ on the line of homogeneous half space ($\bar{k} = 1.44$) denotes the Biot critical point [1], while ‘A’ signifies the subcritical limit of the homogeneous-half-space creasing at $\varepsilon = 0.35$ [72, 73].

Along the wrinkling boundary T_{12} , we encounter a triple point \bar{M}^+ at $\bar{k} = 1.20$ and $\varepsilon = 0.32$; above this point, i.e. $\bar{k} > 1.20$, the wrinkle instability turns into higher-order

cascade instability, and the wrinkle instability line T_{12} becomes an instantaneous crease line T_{13} [12]. At the triple point \bar{M}^+ , the wrinkle instability line T_{12} , the instantaneous crease line T_{13} and the setback crease line T_{2c} merge together. Along the setback crease line T_{2c} , every four other wrinkle valleys crease in expense of relaxing the wrinkle, as discussed in section 2.4.1 with Fig. 2.2c. The setback crease line is extended from \bar{M}^+ to another triple point \bar{M}^- along the trace of green square markers in Fig. 2.4. Along the setback crease trace, we also meet two other triple points D^+ and Q^+ .

At the triple point D^+ at $\bar{k} = 1.00$ and $\varepsilon = 0.24$, the setback crease line T_{2c} , the double-mode wrinkle instability line T_{24} and another setback crease line T_{4c} merge together. The line of $\bar{k} = 1.00$ for $0.24 \leq \varepsilon \leq 0.35$ sets the ruga-phase boundary P_{24} which delineates the ruga-phase (IIc) from (IVc). Along T_{24} depicted by the trace of blue diamond markers in Fig. 2.4, the single-mode wrinkle (II) becomes unstable and transforms to a double-mode wrinkle (IV), as illustrated by the first two frames in each of Fig 2.2d and Fig 2.2e. Across the setback crease line T_{4c} , deep valleys of every fourth primary wrinkle period in the double-mode wrinkle (IV) crease to generate the phase (IVc) as illustrated in Fig. 2.2d. At the triple point Q^+ at $\bar{k} = 0.60$ and $\varepsilon = 0.22$, the quadruple-mode wrinkle instability line T_{45} merges to the setback crease lines T_{4c} and T_{5c} . The line of $\bar{k} = 0.60$ for $0.22 \leq \varepsilon \leq 0.35$ sets the ruga-phase boundary P_{45} which delineates the ruga-phase (IVc) from (Vc) and (Vcf). Along T_{45} indicated by the trace of brown triangle markers, the double-mode wrinkle (IV) becomes unstable and transform to a quadruple-mode wrinkle (V). On the setback crease line T_{5c} , the deepest valleys of every fourth primary wrinkle

period in the quadruple-mode wrinkle (V) crease to produce the phase (Vc) as illustrated in Fig. 2.2e.

At the triple point \bar{M}^- at $\bar{k} = 0.40$ and $\varepsilon = 0.27$, the setback crease line joins the fold line composed of T_{5cf} and T_{56} , and extended from F^- to F^+ . The line of $\bar{k} = 0.40$ for $0.27 \leq \varepsilon \leq 0.45$ sets the ruga-phase boundary P_{56} which delineates the ruga-phase (Vc) from (VI). The fold line traces the purple diamond markers in Fig. 2.4. Across T_{5cf} the valleys of (Vc) fold with their tips creased to produce the phase (Vcf) as illustrated in Fig. 2.2e. It is noted that the PB without mismatch strain cannot develop more than quadruple mode wrinkles, since the deep valleys of the quadruple mode wrinkle begin to fold before higher modes could be activated. As a consequence of folding after mode quadrupling, the PB without mismatch strain can only fold the wrinkles in every four other valleys. In our computer simulations it is noticed that if the bilayer is compressed with a large positive pre-stretch, it can fold every other valleys, but not every valley. In addition, it is found that stiff films of $\bar{k} \leq 0.20$ have critical strains of double-mode and quadruple-mode wrinkle instabilities at $\varepsilon_D = 0.18$ and $\varepsilon_Q = 0.26$, independent of the stiffness ratio of the bilayer system. The folding strain $\varepsilon_F = 0.29$ is also insensitive to variations of the stiffness ratio for such stiff-film bilayers. The last triple point that we see is F^+ at which three phases, (IVc), (Vc) and (Vcf) coexist.

When the wrinkles are compressed to go through setback creasing for $0.60 \leq \bar{k} \leq 1.20$ or folding for $0 \leq \bar{k} \leq 0.60$, the ruga begins to globally localize. The localization starts at a point on the trace of the red square markers in Fig. 2.4. The onset of global localization occurs consistently at $\varepsilon = 0.35$ for $0.40 < \bar{k} \leq 1.20$, exhibiting

imperfection insensitivity. In contrast, the compressive strain to trigger the global localization drops down to approximately 0.30 from 0.35 for $0.20 < \bar{k} \leq 0.40$, and the critical strain to start the global localization wildly fluctuate between 0.30 and 0.40 for $\bar{k} \leq 0.20$. The initiation points of global ruga localization likely indicate that the film crease triggers the substrate-creasing mode of the global localization at $\varepsilon = 0.35$ [72] for $0.40 < \bar{k} \leq 1.2$, and that the folded wrinkle plays a role of imperfection to prompt the substrate-creasing mode in the range of $0.28 < \varepsilon < 0.42$ [69] for $\bar{k} \leq 0.40$. Once the global ruga localization starts, advancements of the periodic localization fronts compete each other through the deformation field, similar to growth of parallel cracks. Eventually only one front will advance by unloading all other fronts. In our simulation, the localization nearly completes at the Biot critical strain $\varepsilon = 0.46$, as indicated with a vertical dotted line in Fig. 2.4.

The PB ruga-phase diagram reveals that there exist five triple points, which can stimulate coexistence of multiple ruga phases caused by fluctuations in variables of ruga formation. The variables include the film thickness, the stiffness ratio and the size of the bilayer, and the boundary conditions of compression. Coexistence of multiple ruga phases limits controllability in making uniform ruga patterns, and is caused by not only fluctuations in ruga-formation variables near triple points but also irreversibility of ruga-phase transitions. Various forms of irreversibility in ruga-phase transitions are discussed in the next chapter. Since the PB ruga-phase diagram in Fig. 2.4 is for monotonic compression, much portion of the ruga-phase boundaries, other than T_{12} , will shift to the left on the diagram for unloading, due to irreversibilities of creasing, some period multiplications and global localizations.

2.5. Conclusion

Extensive nonlinear FEM analyses have revealed various ruga evolution patterns leading to global ruga localization in PB's subjected to large lateral compressive deformation. The ruga evolution is marked by a series of bifurcations which delineate various ruga phases. The PB wrinkles when compressed to $\varepsilon = \{\bar{k}/(2 + 0.3\varepsilon)\}^2$. A PB with a soft compliant film ($0.40 \leq \bar{k} \leq 1.44$) always encounters instantaneous film-crease for $1.20 \leq \bar{k} \leq 1.44$ or quadruple-mode setback film-crease for $0.40 \leq \bar{k} \leq 1.20$, which eventually develops into a global crease localization. In contrast, a PB with a stiff film ($\bar{k} \leq 0.60$) folds before progressing to a crease ($0.40 \leq \bar{k} \leq 0.60$) or fold ($\bar{k} \leq 0.40$) localization. All the folding processes of the PB without pre-stretch are preceded by double- and quadruple-mode wrinkling. Collection of the ruga phases on a (ε, \bar{k}) plane comprises the PB ruga phase diagram. Five triple points are observed on the PB ruga-phase diagram. Fluctuations in ruga-formation variables can promote coexistence of multiple ruga phases near the triple points. A uniform ruga phase can be effectively manufactured by avoiding the triple points. We expect that the PB ruga-phase diagram will play a significant role in controlling nano ruga structures of 2D atomic-layer materials to explore unprecedented functional properties.

Chapter 3

The Primary Bilayer Ruga-Phase Diagram II: Irreversibility in Ruga Evolutions*

*: Part of the results in this chapter had been presented by the author in NewMech workshop 2015 and SES conference 2015.

3.1. Introduction

In the Chapter 2 [13], we constructed a “*Primary Bilayer Ruga-Phase Diagram*” (PB-RPD) of a neo-Hookean bilayer system under monotonic compressive loading on the $\bar{k} - \varepsilon$ plane. Here, $\bar{k} = \sqrt[3]{3\mu_s/\mu_f}$ denotes a normalized characteristic wavenumber which represents a scaled relative shear modulus of the substrate (μ_s) to the film (μ_f), and ε is the compressive strain. We showed on the PB-RPD that the system develops various stable equilibrium configurations of ruga-phases, depending on \bar{k} and ε . Therein, we analyzed evolution paths of various ruga-phases under gradually increasing compressive loading starting from the flat state to the ultimate global localization. The PB-RPD is expected to serve as a guiding map to engineering multifunctional ruga materials which have a wide range of applications such as stretchable electronics, soft robotics and bio-inspired adhesion devices [19-25].

However, in practical applications, materials normally experience repetitive cycles of loading and unloading, for example, charging/discharging of dielectric elastomer actuators in soft robotics. Recently, several studies have revealed that particular ruga-phases are irreversible during unloading. For instance, Hohlfeld and Mahadevan (2011) [74] and Diab and Kim (2014) [12] analyzed irreversibility of free-surface creasing of a neo-Hookean solid, and Zhao, et.al (2015) [136] reported irreversibility of certain multi-mode wrinkles. Therefore, it is crucial to evaluate irreversibility of the ruga-phases on the PB-RPD. In this chapter, we focus our attention on ruga-phase evolution during loading and unloading cycles to investigate ***configurational irreversibility*** of various ruga-phase transitions on the PB-RPD. The configurational irreversibility of a ruga-phase during a loading and unloading cycle implies loss of static equilibrium configuration typically at the critical points of either unstable crease localization or transition in the mode of wrinkle-ruga configuration. We will simply call the former as ‘*localization irreversibility*’ and the latter ‘*modal irreversibility*’.

An example of ***localization irreversibility*** is ruga transition of a smooth free surface or interface to or from a state of a crease tip under subcritical or critical far-field strain. Here we define the critical point as the instance at which the smooth surface snaps to form a crease tip, e.g. creasing of a flat free surface at the Biot strain, 0.46. Such a snapping transition of crease formation typically leads to a load-deformation hysteresis with crease-phase mode locking in reverse loading. Similar localization irreversibility is also observed in ridging. In contrast, two different types of ***modal irreversibility*** are observed in ruga-phase transitions among the single-, double-, quadruple- and folding-mode wrinkles. One is the *rate-independent modal irreversibility* caused by unstable snapping transition of a

large-amplitude wrinkle to another large-amplitude wrinkle. The other is the *rate-dependent modal irreversibility* triggered by inhomogeneous viscoelastic deformation of a wrinkle, which is typically promoted by local pop-out snapping of shallow valleys of the wrinkle. Such a snapping switches the primary period of the wrinkle.

While the nonlinear finite deformation of ruga phases sets the energy landscape for ***rate-independent bifurcation*** of static equilibrium states, various modes of rate-dependent incremental deformation can trigger transitions from a ruga phase to various metastable ruga phases. Both types of modal irreversibility are also observed in ridging and crumpling, and the modal transitions are in general sensitive to lateral boundary conditions in a finite size specimen. Regarding ***rate-dependent irreversibility***, while viscoelasticity effects in wrinkling have been studied extensively [51, 52, 54, 167], viscoelasticity effects in general ruga evolution have not been well understood yet. In this chapter, we show that viscoelasticity promotes generation of diverse modes of meta-stable ruga configurations, which instigates irreversibility of ruga evolution in cyclic loading. In turn, it is found that cyclic instability or stability, i.e. divergence or shake-down, of ruga configurations can be controlled by viscoelasticity. The rate dependent irreversibility of ruga configurations can be a critical behavior of bio-organ deformation [168-170].

The plan of this chapter is as follows. In Section II, we will highlight ***generic irreversible ruga-phases*** on the primary-bilayer ruga-phase diagram (PB-RPD), employing the finite element method (FEM) model developed in Chapter 2. Here, a generic irreversible ruga-phase stands for the phase created by rate-independent bifurcation under quasi-static compression. Throughout this chapter, we employ negligible incrementally linear viscoelastic damping [174-175] by setting the loss tangent (damping energy/elastic

energy) 2×10^{-5} to stabilize the incremental equilibrium-configuration search algorithm of FEM for various bifurcation processes, except for studying specific viscoelastic effects in section IV. In section III, presented are *irreversible transitions of multi-mode wrinkle phases* in a primary bilayer with no mismatch strain. Then, we will discuss *enhancement of ruga irreversibility* triggered by *viscosity effect* in multi-mode wrinkle transitions of PB with *strain mismatch* in section IV. Finally, in Section V, possible irreversible evolution pathways made by cyclic loadings and their corresponding morphological features are sorted and discussed.

3.2. Generic irreversible ruga-phases of the primary bilayer

Fig. 3.1a shows the generic irreversible ruga-phases represented as colored zones on the PB-RPD reported in Chapter 2. While the wrinkling transition across the boundary T_{12} in Fig. 3.1a is reversible during a loading-unloading cycle, irreversibility is observed in some other transitions; the irreversibility depends primarily on the compressive strain and the film/substrate moduli ratio. The zones of various ruga-phases are denoted by Roman numerals on the PB-RPD as follows: Flat state (I), primary single-mode wrinkle [SM1; (II)], wrinkle-setback crease (IIc), global crease limit (III), double-mode wrinkle [DM1; (IV)], double-setback crease (IVc), quadruple-mode wrinkle [QM1; (V)], quadruple-setback crease (Vc), fold-setback crease (Vcf), fold (VI) and global fold localization limit (VII). The number 1 of multi-mode wrinkles, in SM1, DM1 and QM1, signifies the primary period of the mode being the lowest-energy wrinkle period of the PB. In the followings,

metastable multi-mode wrinkles with their primary periods being multiples of the lowest-energy wrinkle period are symbolized as SM_i , DM_i and QM_i , $i = 2, 3, \dots$. In specifying the period, we distinguish two different types of ruga characteristic period, *primary period* (P-period) and *mode period* (M-period). Their definitions are pictorially illustrated as P-period of single mode [SM_1 ; (II)] in Fig. 3.1b₁, M-period of double mode [DM_1 ; (IV)] in Fig. 3.1b₂, and M-period of quadruple mode [QM_1 ; (V)] in Fig. 3.1b₃. In M-period transitions under large compressive strain, its P-period remains the same as that of the primary wrinkle configuration.

As previous studies [74, 12] revealed, an individual crease under cyclic loading makes a smooth free surface (or interface) snap-jump to and from subcritical crease states. As aforementioned, a flat free surface under monotonic compressive loading snaps to crease at the Biot critical strain. In a special case, a surface defect can cause singular perturbation on the fundamental state, and trigger reversible creasing on the flat free surface of a neo-Hookean half space at a smaller compressive strain, approximately 0.35 [73]. However, in PB, all the crease tips along the curves of T_{13} , T_{2c} , T_{4c} , and T_{5cf} are under corresponding critical far-field strains, and follow trajectories of subcritical crease states with mode locking upon unloading. In turn, the transitions across the curves are all irreversible under cyclic loading. The boundaries of crease unloading jump are located on the left side of the critical crease loading jump curves in PB-RPD. These irreversible transitions make the ruga phases, IIc, IVc, Vc, Vcf (in green) and those towards (III) (in pink) locally irreversible for their crease tips. Since the local irreversibility of creasing is relatively well

understood by now, primarily the *modal irreversibility* of bilayer creasing and multi-mode wrinkling will be treated in the rest of this chapter.

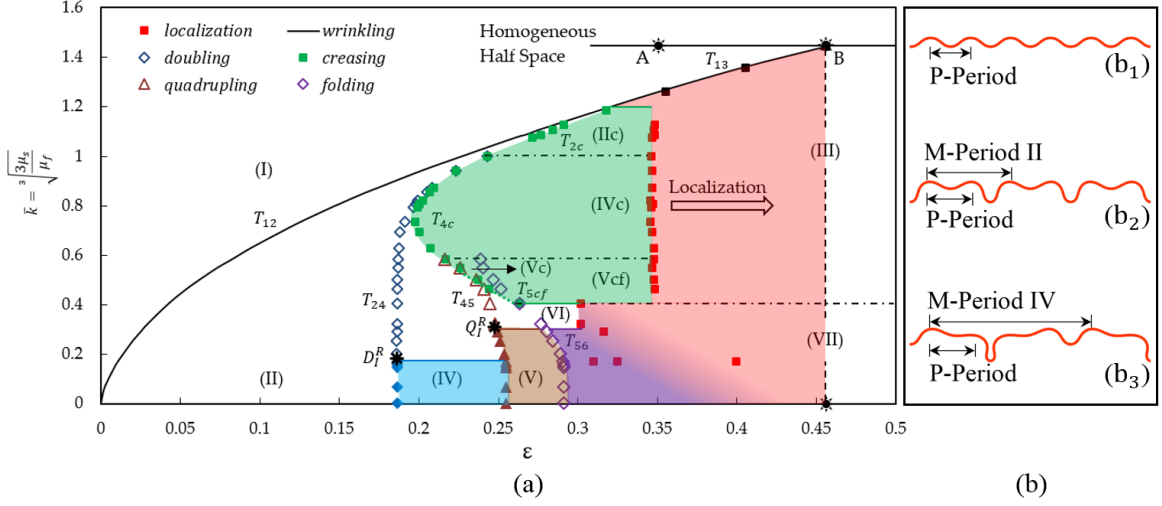
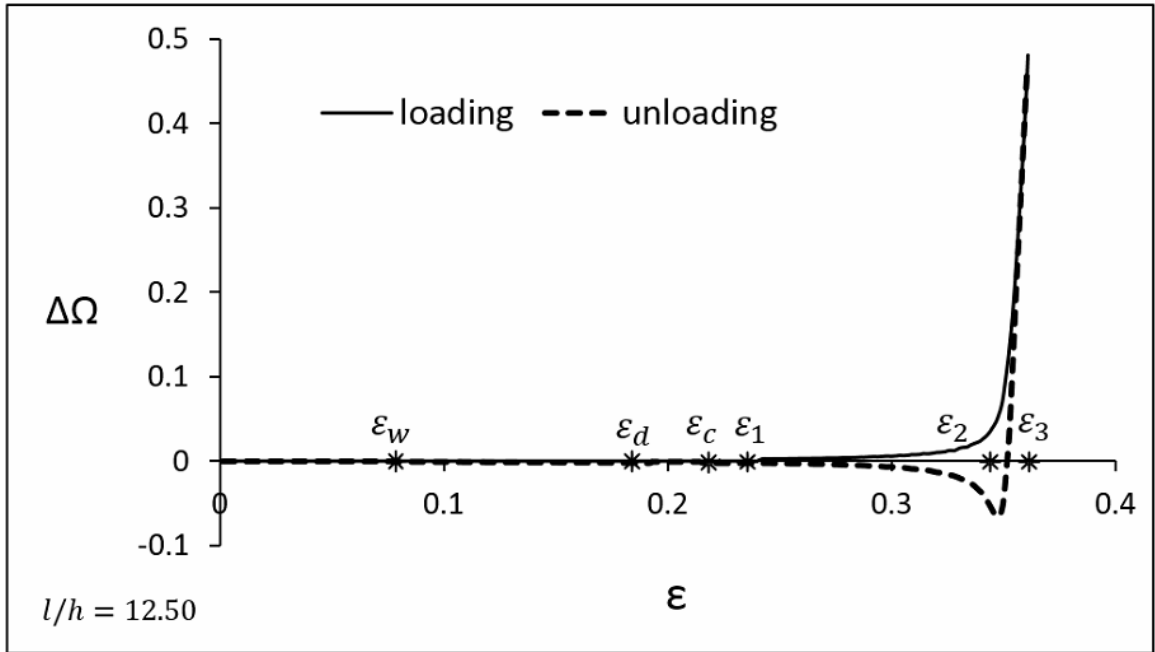


Figure 3.1. The primary ruga-phase diagram: \bar{k} ; scaled stiffness ratio, ϵ ; compressive strain: (I) flat phase, (II) single-mode wrinkle phase, (III) global crease localization, (IV) double-mode wrinkle phase, (V) quadruple-mode wrinkle phase, (VI) fold phase, (VII) global fold localization, (IIc), (IVc) & (Vc); three setback-crease phases, (Vcf) crease-fold phase, A; subcritical crease strain limit, B; Biot critical strain of creasing, D_I^R ; M-period doubling limit, Q_I^R ; M-period quadrupling limit. The five colored regions represent irreversible ruga-phases.

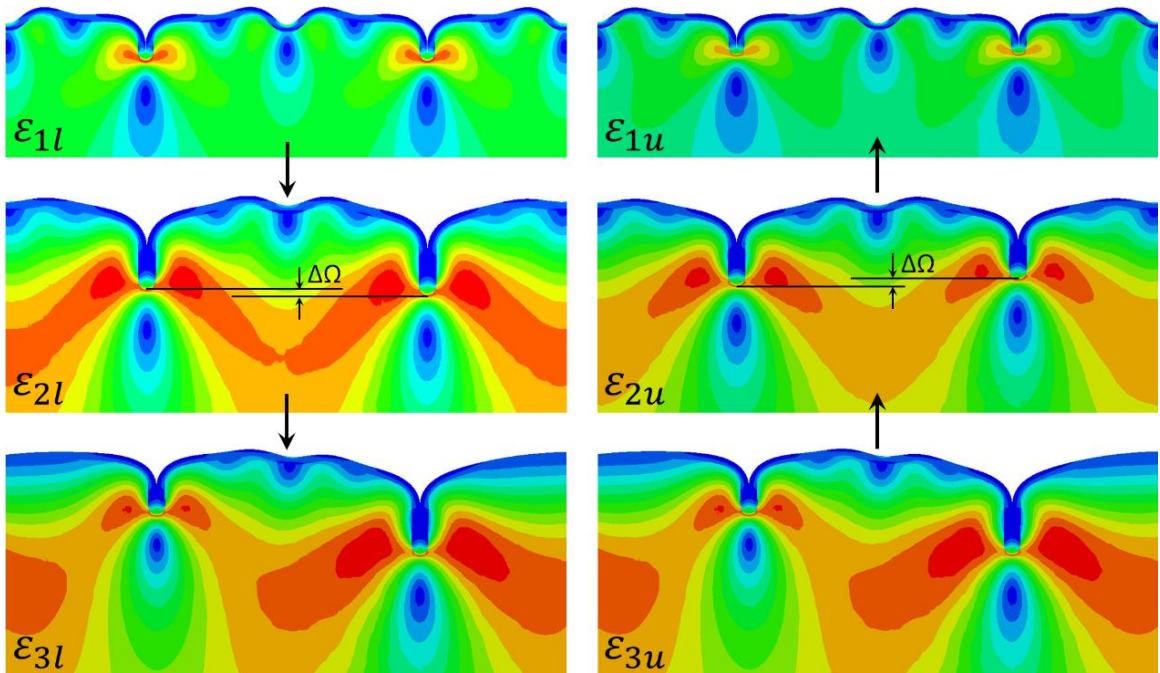
3.2.1. Irreversible ruga-phases of cooperative-mode creases

Fig. 3.2a shows variations of the normalized crease-depth difference, $\Delta\Omega$, between near-neighbor creasing valleys in four P-period as a function of the nominal compressive strain, ϵ , for $\bar{k} = 0.59$, across the initiation point of global creasing at $\epsilon \approx 0.35$ during a

loading-unloading cycle. Throughout this chapter, $\Delta\Omega$ is normalized by the P-period (wavelength in undeformed configuration). Solid curve corresponds to loading and dashed curve to unloading, exhibiting apparent hysteresis. When the loading varies, the surface configuration maintains its translational symmetry through the SM1 wrinkle phase for $\varepsilon_w < \varepsilon < \varepsilon_d$, where ε_w and ε_d represent the critical strains of wrinkling and period doubling respectively. Once the period doubles, the DM1 wrinkle steadily grows upon further compression until ε reaches the period quadrupling strain ε_q where every four other deep valleys crease, i.e. $\varepsilon_q = \varepsilon_c$. Beyond this crease initiation, the periodic crease depths grow uniformly as shown in Fig. 3.2b- ε_{1l} until the compressive strain approaches an apparent bifurcation strain, ε_1 . At this strain, periodic creases begin to deviate from the translationally symmetric configuration. Upon, further compression $\Delta\Omega$ follows the upper bifurcation branch (solid line) in Fig. 3.2a, until the compressive strain reaches creasing strain of the substrate, 0.35, beyond which $\Delta\Omega$ grows rapidly, developing global crease localization. Upon unloading, traces of $\Delta\Omega$, closely follows the solid branch until the strain reaches a value near 0.35 at which the system jumps down to the lower parity bifurcation branch (dashed line).



(a)



(b)

Figure 3.2. Cooperative creasing irreversibility for $\bar{k} = 0.59, R = 15$. (a) $\Delta\Omega$ is the crease tips amplitude difference normalized by critical onset wrinkling wavelength. The normalization factor of the critical onset wrinkling wavelength by film thickness is shown at the bottom left corner of the table. Critical strains for wrinkling, doubling and creasing modal bifurcations are marked on the axis: $\varepsilon_W = 0.08$, $\varepsilon_D = 0.19$, $\varepsilon_C = 0.22$; $\varepsilon_1 = 0.24$, $\varepsilon_2 = 0.35$ and $\varepsilon_3 = 0.36$ are three particular strains which are chose for comparison of loading and unloading; (b) contour plot of loading and unloading FEM results for ε_1 , ε_2 and ε_3 .

Fig. 3.2b (ε_{2u}) shows the parity bifurcation configurations observed during a loading-unloading cycle across the critical 0.35 strain. As shown in the insets of ε_{1l} and ε_{2l} in Fig. 3.2b, symmetry of the cooperative crease mode is broken beyond ε_1 , and $\Delta\Omega$ grows rapidly across the 0.35 strain to reach the configuration of ε_{3l} . Upon unloading, variation of the configuration from ε_{3u} to ε_{2u} changes the sign of $\Delta\Omega$ in ε_{2u} , compared to that of ε_{2l} . Then, further unloading recovers the periodic configuration of ε_{1u} same as ε_{1l} . We believe that this parity bifurcation is primarily caused by fictitious viscosity that we employed in our FEM model to stabilize convergence of the numerical solution. In the limit of no viscosity, the two traces may merge and transit vertically at the compressive strain of 0.35.

Regarding the initial crease formation, the critical strain, ε_c , strongly depends on the critical wave number \bar{k} in the range of $0.40 < \bar{k} < 1.44$; on the other hand, the transition of the cooperative film-crease mode towards the global crease localization of the

substrate is consistently triggered at a fixed strain value of $\varepsilon \approx 0.35$ for $0.40 < \bar{k} < 1.20$. Starting from homogeneous half space ($\bar{k} = 1.44$), for $1.20 < \bar{k} < 1.44$, the flat surface of the film develops instantaneous creases through transition T13. For $0.40 < \bar{k} < 1.20$, a SM1 wrinkle develops periodic local setback creases on the free surface of the film in every four other wrinkle valleys. The setback creasing transitions are denoted as wrinkle-setback crease across T2c for $1.00 < \bar{k} < 1.2$; double-setback crease across T4c for $(0.60 < \bar{k} < 1.00)$; quadruple-setback crease across T5c and the fold-setback crease generated by further loading across T5cf for $0.40 < \bar{k} < 0.60$. All these transitions lead to uniform stable growth of periodic film crease tips up to 0.35 compressive strain for $0.40 < \bar{k} < 1.20$, crossing the green zone in Fig. 3.1a, followed by global localization of substrate creasing beyond the 0.35 strain (pink zone in Fig. 3.1). Our FEM simulations reveal that the periodic film creasing occurs through unstable snap jump at a critical strain during loading cycle, while the crease phase locks in its mode across the critical strain during unloading cycle. Then, the periodic crease tip configuration maintains its mode down to a subcritical strain at which the periodic crease phase snaps back to the wrinkle phase [74, 12, 164]. In contrast, the global creasing exhibits a different irreversibility phenomenon – modal instability in growth or recession of the periodic crease tips. The modal irreversibility of creasing is often amplified by viscosity effect on the interactions among the film creases and the substrate crease.

3.2.2. Irreversible ruga-phases of multi-mode wrinkles

Besides above-discussed creasing irreversibility, we have also investigated irreversibility of multi-mode wrinkling transitions: M-period doubling (II-IV) through transition T24; M-period quadrupling (IV-V) through T45; folding (V-VI) through T56; fold localization (VI-VII). Our FEM results show that reversibility of the various modes (DM1, QM1, and F) depends mainly on the modulus ratio of the bilayer system, $R(= \mu_f/\mu_s)$. Therefore, we have run FEM simulations of the loading-unloading cycle for the whole range, $0 < \bar{k} < 0.40$ ($\infty > R > 45$), within which M-period multiplications occur.

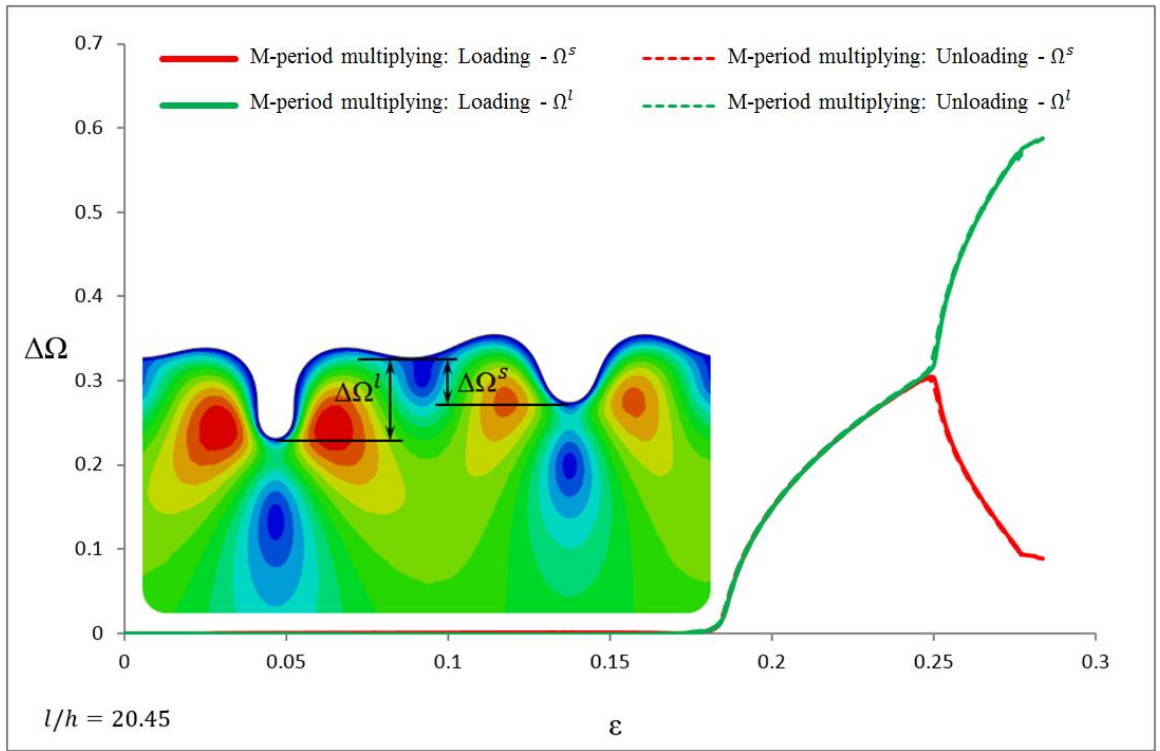
Our simulations reveal two distinct characteristic wavenumbers, $\bar{k} = 0.29$ ($R = 120$) and $\bar{k} = 0.17$ ($R = 600$) denoted as Q_I^R and D_I^R respectively in Fig. 3.1a. Within $0.29 < \bar{k} < 0.40$, i.e. above Q_I^R , the system undergoes reversible transitions from flat state (I) to fold (VI) through multi-mode wrinkling phases. We only observe pronounced rate-dependent irreversibility when folding localizes in (VII), which is triggered by creasing of the substrate. In other words, transitions from SM1, DM1, QM1, and F within this characteristic wavenumber region are all reversible with no hysteresis. This particular reversible corridor of $0.29 < \bar{k} < 0.40$ and $0 < \varepsilon < 0.30$ allows controllability of the fold patterns. This feature is expected to be technologically very attractive for various applications such as stretchable electronics and soft robotics [3, 165]. For $0.17 < \bar{k} < 0.29$, M-period doubling is reversible, while M-period quadrupling and folding processes are irreversible. For very stiff film bilayers, $\bar{k} < 0.17$, the transitions of M-period multiplication, $\text{II} \rightarrow \text{IV} \rightarrow \text{V} \rightarrow \text{VI} \rightarrow \text{VII}$, are all irreversible, which engender hysteresis in ruga evolution under cyclic loading, with mode locking in unloading cycle. The irreversible multi-mode wrinkle phases are marked in blue, brown and purple on the PB-RPD in Fig.

3.1a. In the following section, detailed analyses of the irreversibility and their implications on formation and evolution of various modes are presented.

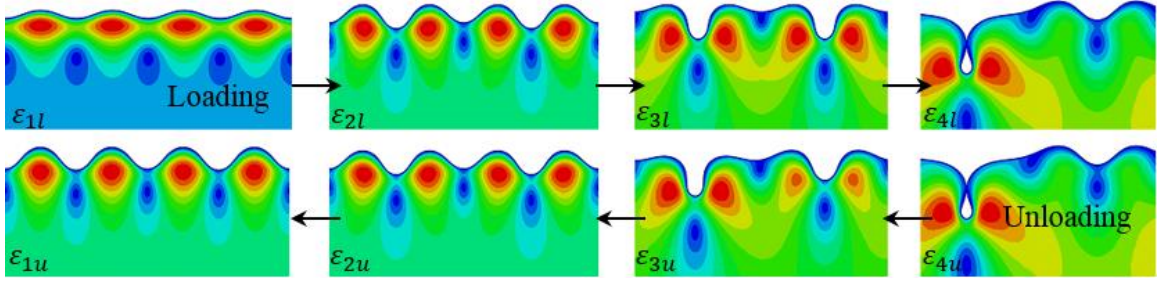
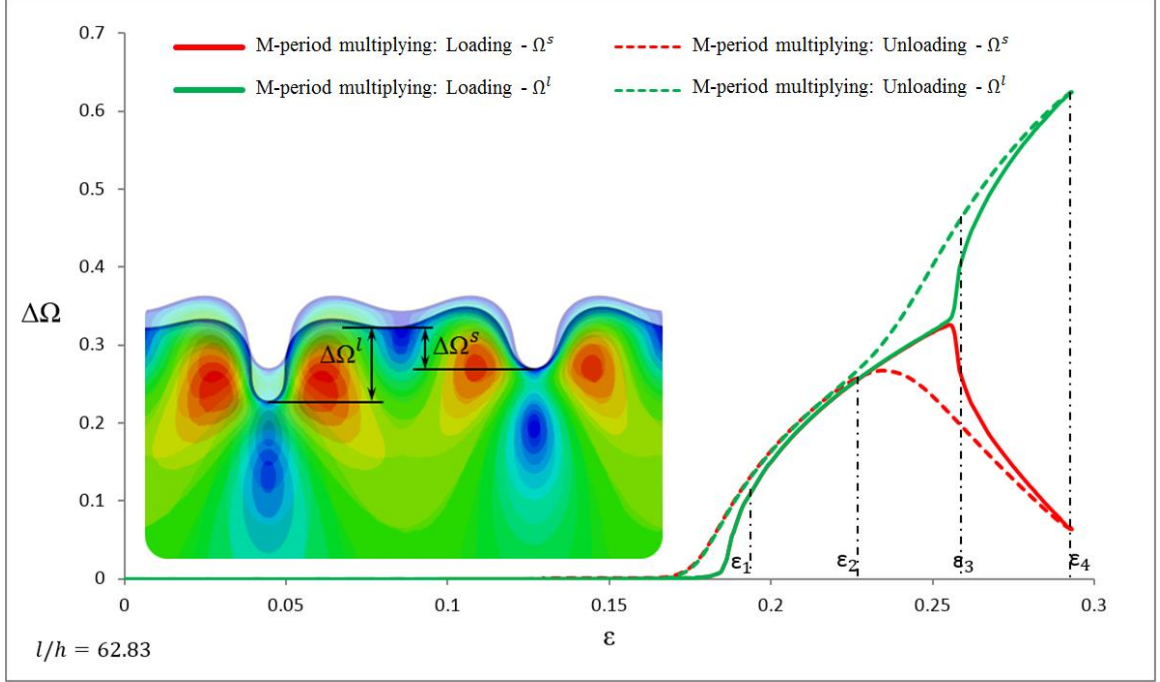
3.3. Irreversible transitions of multi-mode wrinkles of PB without strain mismatch

Transitions between various pairs of ruga modes occur through symmetry breaking of height variations in the wrinkle configuration. Therefore, we have traced the evolution of the height differences between a wrinkle valley and its two adjacent valleys, denoted by $\Delta\Omega^l$ and $\Delta\Omega^s$ respectively, as shown in the insets of Fig. 3.3. Here, the super script l and s denote large and small respectively. Figure 3.3a shows traces of $\Delta\Omega^l$ and $\Delta\Omega^s$, during a loading-unloading cycle for a bilayer system with the stiffness ratio $R = 90$ ($\bar{k} = 0.32$). During loading, the SM1 wrinkle symmetry is conserved until the critical strain for period doubling is attained at $\varepsilon \approx 0.18$, at which the SM1 symmetry is broken and a DM1 configuration emerges. Then, another higher-mode bifurcation occurs at a strain ($\varepsilon \approx 0.26$) at which the DM1 bifurcates into a QM1. As shown in Fig. 3.3a, both traces of $\Delta\Omega^l$ and $\Delta\Omega^s$ coincide for loading (solid line) and unloading (dashed line), indicating reversibility of period doubling and quadrupling for the bilayer system with $R = 90$. However, for a bilayer system with a high stiffness ratio, $R = 3000$ ($\bar{k} = 0.10$), the traces of $\Delta\Omega^l$ and $\Delta\Omega^s$ in Fig. 3.3b do not coincide for loading (solid line) and unloading (dashed line), showing hysteresis of the ruga configuration in the cyclic loading. This configurational irreversibility is clearly shown in Fig. 3.3b with the simulation frames taken at the same strains, $\varepsilon_1, \dots, \varepsilon_4$, of loading and unloading. Although the small fictitious viscosity

employed in our FEM model to stabilize convergence obscures the sharp jumps at the doubling and the quadrupling points of the mode, the distinct hysteresis loops are evident for a highly stiff-film PB without strain mismatch. The results indicate that the unloading transitions undergo with *mode locking* as shown in the frames captured at particular strains ε_1 , ε_2 , ε_3 and ε_4 . Now, questions arise. Does irreversibility always manifest itself through *mode locking*, or it may lead to excitement of other modes that are not accessible during loading?



(a)



(b)

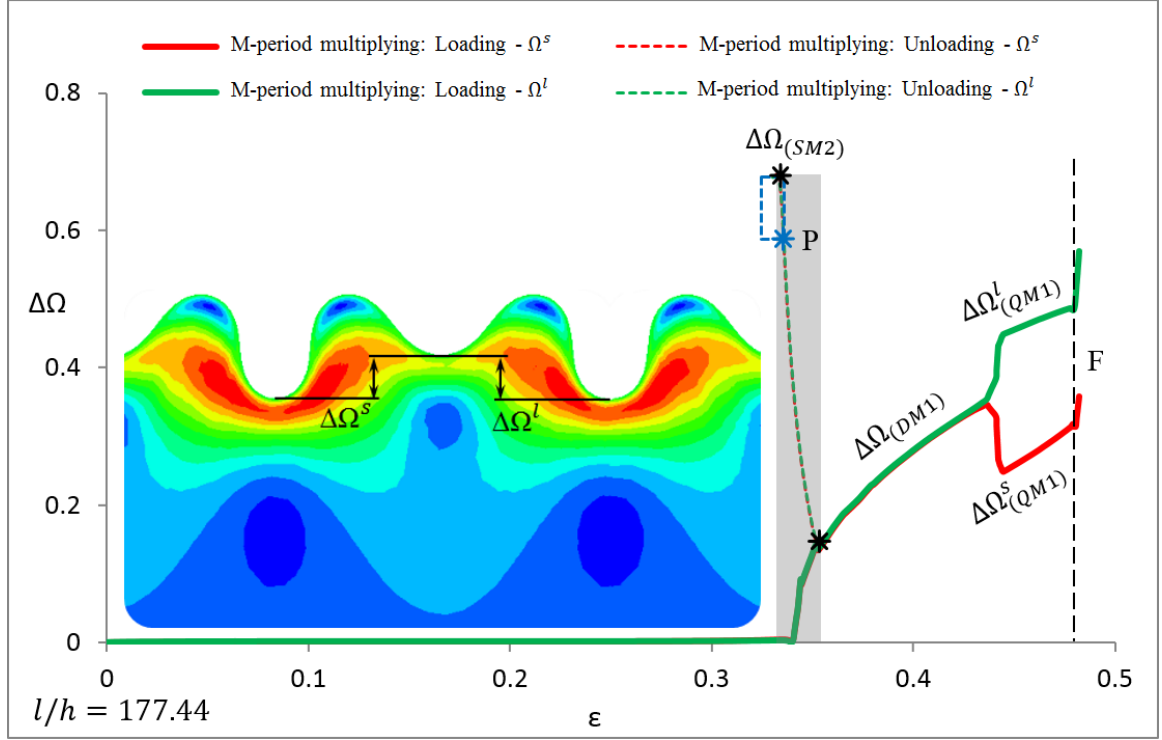
Figure 3.3. Reversibility of the ruga modes on the surface of the bi-layer system without strain mismatch at the interface. $\Delta\Omega$ is the amplitude difference normalized by critical onset wrinkling wavelength. Reversibility is checked by plotting the traces, $\Delta\Omega^s$ and $\Delta\Omega^l$, of the vertical normalized amplitude difference between the period doubling valley and respectively the single mode valley and the quadrupling valley, as a function of the global nominal strain during a loading-unloading cycle. The normalization factor of the critical onset wrinkling wavelength by film thickness is shown at the bottom left corner of the

table. (a) bilayer with modulus ratio $R = 90$ ($\bar{k} = 0.32$): the traces coincide during the loading-unloading cycle indicating reversibility of the ruga modes; (b) bilayer with modulus ratio $R = 3000$ ($\bar{k} = 0.10$): both DM2 and QM2 exhibit hysteretic behavior during unloading leading to mode locking; the FEM contour plots show the ruga phases under four specific compressive strains ε_1 , ε_2 , ε_3 and ε_4 during loading and unloading.

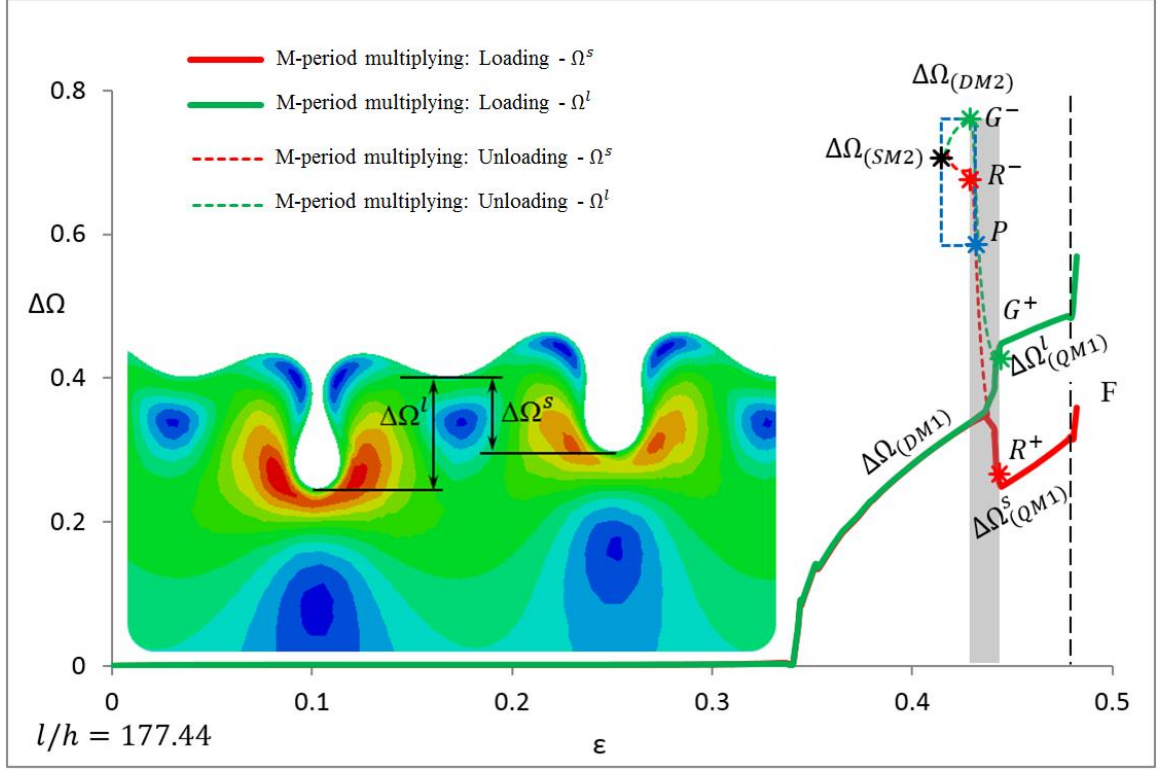
3.4. Primary-period switching jumps in cyclic ruga evolution of PB with strain mismatch

In previous sections, we showed that synergistic effects of viscosity and large nonlinear deformation can substantially enhance irreversibility of ruga *mode transitions* in PB without strain mismatch. Here, in this section, we present excitation of *P-period switching jumps*, triggered by minute increase in viscosity, that further enhance irreversibility in cyclic ruga evolution of PB with strain mismatch. In our simulations, the strain mismatch is implemented by pre-stretching the substrate and subsequently attaching a stress-free layer on the surface of the substrate. Upon releasing the pre-stretch of the substrate, the film is compressively loaded to make the flat state unstable and a SM1 wrinkle mode emerges. The FEM-plot insets in Fig. 3.4a and Fig. 3.4b show typical multi-mode wrinkle configurations, DM1 and QM1, observed during loading cycle of a bilayer system with stiffness ratio $R = 10^5$ ($\bar{k} = 0.07$) and substrate pre-stretch ratio $\lambda_{ps}=1.4$. In the graphs of Fig. 3.4, the horizontal axis represents nominal compressive strain of the film, measured with respect to the pre-stretched configuration. The vertical axis $\Delta\Omega$ denotes the depth difference between the neighboring shallow and deep valleys, normalized by the P-

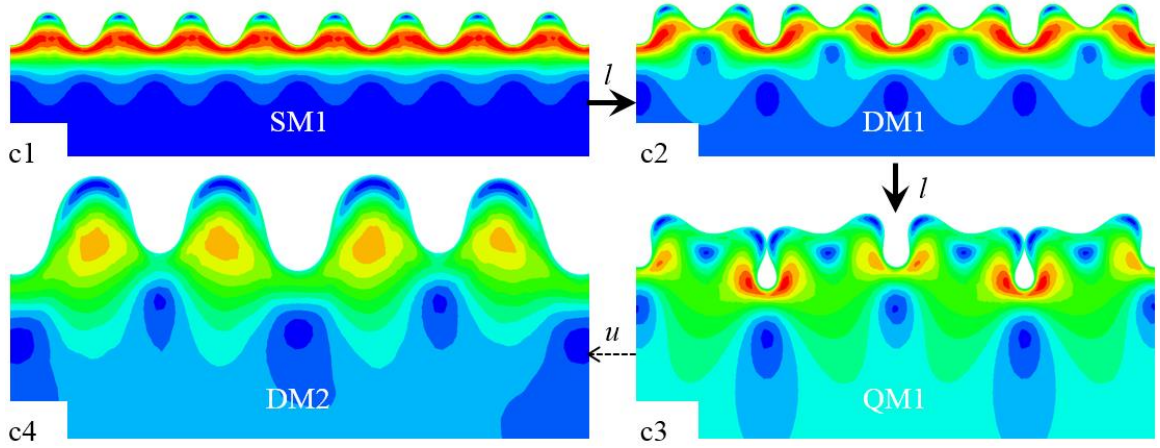
period wavelength. If the pre-stretch for the strain mismatch were greater than approximately 1.5 for the stiff film, ridging instability would trigger different types of irreversible ruga evolution such as order disorder transitions in ridging and crumpling [32, 78, 79, 151-157].



(a)



(b)



(c)

Figure 3.4. P-period switching irreversibility of PB with strain mismatch ($R = 10^5$ and pre-stretch ratio $\lambda_{ps} = 1.4$) during loading/unloading cycle: $\Delta\Omega$; amplitude difference normalized by critical onset wrinkling wavelength l , ε ; compressive strain, $(\Delta\Omega^s, \Delta\Omega^l)$;

normalized amplitude difference between shallow wrinkling valley and two neighboring deep valleys, Solid curves; loading ($DM1 \rightarrow QM1 \rightarrow F$), Dashed curves; unloading, P ; critical point where shallow wrinkle valley becomes flat. (a) Unloading from M-period doubling ($DM1 \rightarrow SM2$). (b) Unloading from M-period quadrupling ($QM1 \rightarrow DM2 \rightarrow SM2$): (G^+ , R^+); unloading starting points of two quadrupling bifurcations, (G^- , R^-); points of excited-mode DM2, Black star; configuration of excited-mode SM2. (c) FEM contour plots of ruga evolution during a loading-unloading cycle: ($c1$, $c3$); primary modes through transition ($SM1 \rightarrow DM1 \rightarrow QM1$), $c4$; excited-mode DM2 during unloading by snap-buckling from QM1.

During compressive loading on the film, the bilayer system develops ruga-phase evolution ($SM1 \rightarrow DM1 \rightarrow QM1 \rightarrow F$) similar to the case of high stiffness ratio PB with no strain mismatch, as shown with solid curves in Fig. 3.4a and Fig. 3.4b. However, the critical strains for period doubling and quadrupling, 0.34 and 0.44, are respectively larger than their corresponding strains, 0.18 and 0.26, for the same stiffness-ratio bilayer system without strain mismatch. For this stiff film, the transitions from single mode (SM1) to double mode (DM1) and from double mode (DM1) to quadruple mode (QM1) both exhibit unstable bifurcation of snap buckling, similar to those of the same stiffness-ratio bilayer system with no strain mismatch. However, unlike the latter without strain mismatch which makes mode locking during unloading cycle, the former with strain mismatch exhibits *P-period switching jumps* promoted by viscosity upon unloading as described below in detail. In order to see sensitivity of unloading bifurcation on viscosity, in Fig. 3.4, we

present unloading ruga-phase evolution stimulated by a minute but not negligible viscoelastic loss tangent of 2×10^{-4} .

The dashed lines in Fig. 3.4a show traces $\Delta\Omega$ transitions during *unloading* the compressive strain of the film from a state of DM1 at a strain very close to the mode-doubling critical strain. The ruga configuration reversibly follows the (green) solid curve between the critical points of mode doubling and mode quadrupling, until it reaches a strain within 1 % from the mode-doubling critical strain, as marked lower * in Fig. 3.4a. At this point, it makes a snap buckling transition to a completely new mode, SM2, which is a single mode but it has its period two times the period of the SM1. The P points in Fig. 3.4a and Fig. 3.4b denote the moments of local buckling at which the shallow valleys transit to peaks. At the transition point P, shallow valleys turn flat to have zero curvature locally. Subsequently, they bulge out and become peaks. The dotted box contains the unloading process after P point. That is to say, within the dotted box, we measure $\Delta\Omega$ as the depth difference between the deep valley and the newly formed peak.

Similarly, in unloading the system from QM1, shown in Fig. 3.4b, as the strain approaches the critical quadrupling strain within 1 %, G^+ and R^+ , the system experiences a *snap buckling* transition from QM1 to DM2. Upon further unloading, another transition from DM2 to SM2 was also observed. The FEM simulation configurations of the snap buckling transitions (SM1 \rightarrow DM1 \rightarrow QM \rightarrow DM2) are exhibited in the frames (c1-c4) of Fig. 3.4c. This unloading bifurcation process of QM \rightarrow DM2 is made in competition between the local bifurcation process of shallow valley pop ups, QM1 \rightarrow DM2, and the modal bifurcation process of the long range interaction mode, QM1 \rightarrow DM1. In this competition,

a small fluctuation of the configuration evolution caused by material inhomogeneity or viscosity can bias the bifurcation. In particular, it is found that material viscosity plays significant role to bias the bifurcation towards $QM1 \rightarrow DM2$. Once it bifurcates to DM2, the amount of unloading strain to reach SM2 is much smaller than the difference between the critical strains of $SM1 \rightarrow DM1$ and $DM1 \rightarrow QM1$ transitions. Then, upon further unloading, SM2 maintains its mode in a metastable state. Although SM2 is a higher energy mode than SM1, the energy barrier from SM2 to SM1 by doubling the frequency is not negligible and the SM2 sustains the mode as a metastable state. Direct doubling of the frequency from SM2 to SM1 for every crust has very high activation barrier, while frequency doubling through snaky adjustment by propagation of wrinklons [120-122] is considered to have lower energy barrier. However, the latter energy barrier is considered to depend on the lateral boundary conditions and the specimen size.

3.5. Enhancements in cyclic ruga irreversibility: causes and consequences

We discussed in section 3.3 that mode locking in reverse loading near a critical point can instigate ruga irreversibility, and in section 3.4 that P-period switching jumps can dramatically boost cyclic irreversibility of ruga evolution. In this section, we examine how viscosity triggers P-period switching jumps to enhance the cyclic irreversibility, and what are the consequences of the mode-locking and the P-period switching mechanisms on attaining cyclic stability of ruga configuration hysteresis.

3.5.1. Viscosity effect on Primary-period switching jumps in cyclic ruga-evolution

As discussed in the previous section, different bifurcation mechanisms such as mode-locking and P-period switching can compete near a certain critical strain during unloading cycle. Bifurcation of an autonomous local deformation mode, e.g. local curvature flipping of shallow wrinkle valleys, can occur while a transition is made in a long range interaction cooperative mode, e.g. double or quadruple modes, etc. Then, such an autonomous local mode bifurcation can substantially enhance irreversibility of cooperative ruga modes in cyclic loading of PB with strain mismatch. In particular, material viscosity can delay relative evolution speed of a certain mode to trigger an unexpected autonomous mode which would not be activated if the material were elastic. Here, we show that such an autonomous mode bifurcation can trip cyclic instability of ruga evolution, leading to cyclic divergence or cyclic shake down of ruga modes.

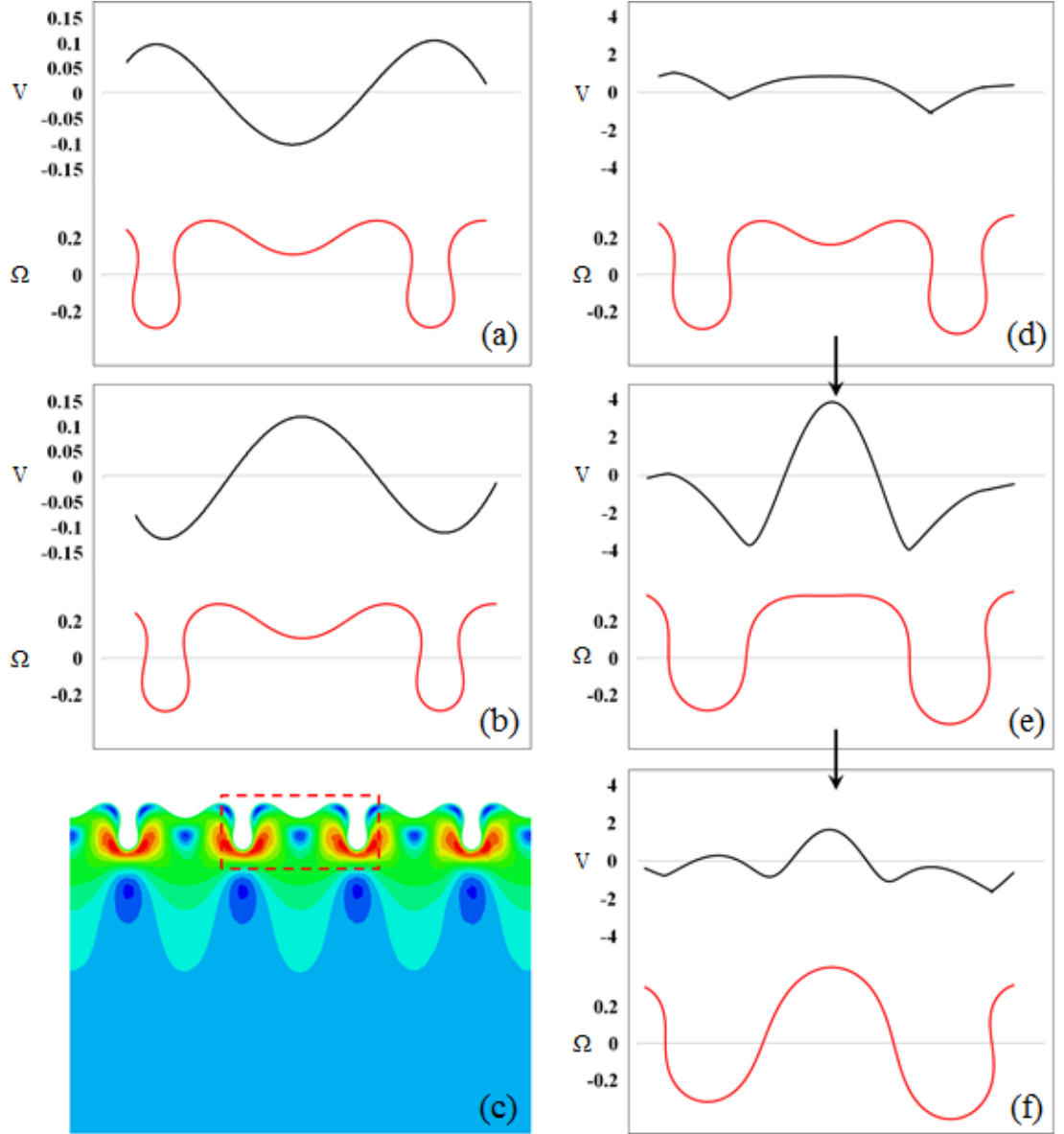


Figure 3.5. Vertical surface velocity of P-period switching: Upper curves of (a, b, d, e, f); velocity profile of a selected range marked by dashed red box in (c), Lower curves; corresponding surface profiles (Ω normalized by critical onset wrinkling wavelength l). (a) Unloading from QM1 to current DM1 with small viscosity. (b) Loading to current DM1: (d-f); unloading from QM1 to SM2 with viscoelastic loss tangent of 2×10^{-4} .

Figures 3.5(a-b) respectively show nearly reversible unloading and loading states of surface velocity V and configuration Ω of a DM1 ruga surface of a low viscosity system with 2×10^{-5} loss tangent, while Figs. 3.5(c-e) display those of irreversible unloading process in a relatively high viscosity system with 2×10^{-4} loss tangent. Here the surface velocity is defined as change in vertical surface displacement normalized by the P-period, with respect to global strain increment. The configurational deformation amplitude Ω is normalized by the P-period. As illustrated in Fig. 3.5a for unloading of the low viscosity system, the shallow valley is moving upward while the neighboring deep valleys are moving downward, exactly opposite to the loading case (Fig. 3.5b). For the low viscosity system, materials are considered to experience nearly reversible deformation. In contrast, the unloading surface velocities shown in Figs. 3.5(c-e) for the high viscosity system are out of phase with respect to the velocity shown in Fig. 3.5a. The criticality of the velocity bifurcation is noticed in Fig. 3.5d; the velocity of the shallow-valley surface is just reversed to that in Fig. 3.5a. Figures 3.5(e-f) show that upon further unloading the shallow valley snaps out while its adjacent valleys reverse their motion albeit at smaller speed. This local snapping is believed to be caused by viscosity effect for different deformation rates along the corrugated surface.

3.5.2. Cyclic stability of ruga configuration hysteresis and coexistence of ruga-phases

Fig. 3.6 collectively shows schematic configurations of various ruga-phases that can appear on the surface of a PB system under repeated cycles of loading and unloading. The three major PB ruga localization types are illustrated in Fig. 3.6a – the crease, the fold, and

the ridge localizations. *The PB crease localization* is a global localization. It commences at the Biot strain (0.46) on a smooth surface of a homogeneous incompressible neo-Hookean half space, and at 0.35 strain for the half space with a surface imperfection. Such an imperfection includes single or multi-layer thin films, graded modulus distribution, surface singularity and defects. *The PB fold localization* is induced by substrate crease localization, but the onset strain widely varies depending on self-contact conditions of local folds elicited by the folding process. For a PB system with $0 < \bar{k} < 0.6$, the surface layer generates periodic local folds at every fourth wrinkle valley, but the critical strain of global fold localization varies depending on smoothness of the local fold fronts. (i) When $0.4 < \bar{k} < 0.6$, each local fold generates a crease tip on its advancing front. The crease tip tends to stabilize *cooperative parallel growth* of the local crease tips until the substrate globally creases at the compressive strain of 0.35. (ii) When $0 < \bar{k} < 0.4$, the local folds grow with a smooth fold fronts, which easily induce instability with high imperfection sensitivity in cooperative growth of the local folds. Such instability can occur at any compressive strain between the local-folding and the Biot strains. These two kinds of folding localizations --- *crease tip guided localization* and *smooth fold localization*, have different characteristics in configurational energetics. Crease tips on a fold front make lateral configurational sliding of the tips difficult, in contrast to smooth fold fronts. Easy lateral configurational sliding of smooth fold fronts causes high imperfection sensitivity in triggering global fold localization, and thus large uncertainty in the critical strain of global fold localization. *The PB ridge localization* is a growth-limiting localization which sprouts out instead of sinking into the substrate. It is usually caused by strain mismatch between the film and the substrate, and growth of ridge height is intrinsically limited.

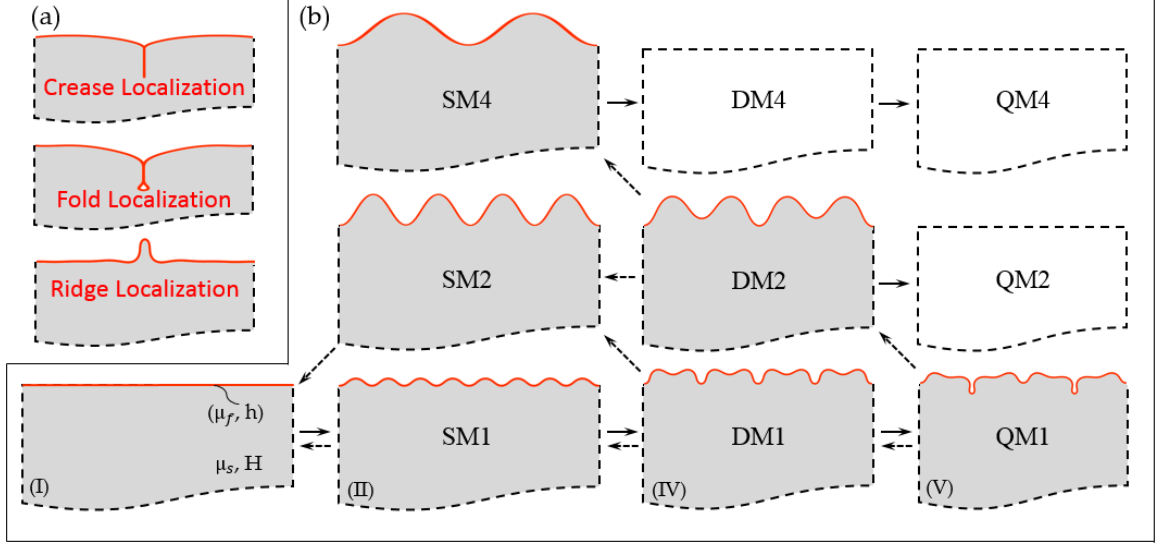


Figure 3.6. Schematics of ruga-modes on the surface of a neo-Hookean bilayer system, composed of a thin film with modulus μ_f and a deep substrate with modulus μ_s , subject to a loading-unloading cycle. (a) Three types of global ruga localization, crease, fold and ridge; (b) Mode transitions during the loading-unloading cycle, where solid and dashed arrows represent loading and unloading processes respectively, the bottom row shows ruga evolution pathway for a bilayer system during the loading segment of the cycle, (I) flat phase, (II) primary single-mode wrinkle phase SM1, (IV) primary double-mode wrinkle phase DM1, (V) primary quadruple-mode wrinkle phase QM1; the other ruga modes denoted by (SMi), (DMi) and (QMi), $i=2,4$, denote corresponding excited-modes observed in simulation during unloading; the dashed boxes represent other possible excited-modes that are not detected by our simulations.

For a PB system of $\bar{k} < 0.40$ without strain mismatch, no crease manifest on the film surface, and the ruga phase evolves along the pathway (SM1 \rightarrow DM1 \rightarrow QM1) as shown in the bottom row of Fig. 3.6b. For PBs with negligible viscosity, unloading follows the

bottom row configurations ($QM1 \rightarrow DM1 \rightarrow SM1$) either with or without hysteresis, depending on the stiffness ratio. However, for an appreciably viscoelastic PB system of $\bar{k} < 0.40$ with strain mismatch, P-period switching makes the ground modes, DM1 and QM1 set off to SM2 and DM2 respectively during unloading. Various possible P-period switching transitions are illustrated in Fig. 3.6b. We denote these modes by SM_i , DM_i , QM_i , $i = 1, 2, 3, \dots$, for which modal translational symmetry holds in every single, double and quadruple primary period(s). The index, i , stands for the ratio of the primary period of the mode with respect to the primary period of the ground mode. For example, the set-off modes SM2, DM2 and QM2 have the same geometric mode configurations as the ground modes SM1, DM1, and QM1, correspondingly; however, the primary period is doubled. When SM2 generated by P-period switching of DM1 in the unloading cycle is reloaded by compression, the mode will bifurcate to DM2 instead of returning back to DM1. The energy barrier is too high to directly flip the convex curvature of the SM1 wrinkle peak to a concave curvature of a wrinkle valley. Therefore, it is likely that if the viscosity is properly matched for the loading rate, the wrinkle modes would diverge under cyclic loading, following $SM1 \rightarrow DM1 \rightarrow SM2 \rightarrow DM2 \rightarrow SM4 \rightarrow DM4$. This mechanism can excite the ground mode (SM1, DM1, QM1) to a higher energy modes (SM_i , DM_i , QM_i , $i = 2$ or $4, \dots$) by tuning the loading rate for a given viscosity.

As discussed above, if the viscosity and the loading rate are properly matched, cyclic loading can make the ruga-phase diverge to those of high-energy metastable configurations or shake down to a certain energy-level metastable configuration. Furthermore, this mechanism can generate variety of coexistent ruga-phases of PB with spatial imperfections in its property, geometry or loading conditions.

3.6. Conclusion

We have revisited the primary bilayer ruga-phase diagram (PB-RPD) [13] to investigate configurational reversibility of various ruga-phases under cyclic loading. Our extensive finite element simulations of single loading-unloading cycle reveal that many metastable ruga states exist, and many phases (SM1, DM1, QM1 and F) on PB-RPD are irreversible in their configurational variations under the cyclic loading, despite the system is locally elastic everywhere. It is also found that the cyclic irreversibility is enhanced by initial film/substrate strain mismatch and material viscosity. The cyclic irreversibility is classifiable, in large, by ‘*localization irreversibility*’ and ‘*modal irreversibility*’.

The localization irreversibility is found to be associated with *unstable* creasing of either the film surface or the substrate. The film surface creasing typically emerges as periodic setback creasing of wrinkle or fold valleys within a range of the normalized critical wave number, $0.4 \leq \bar{k} \leq 1.44$, while the substrate creasing induces global localization. When the set-back creases globally localize later, sharp tips of the periodic film creases stabilize uniform *cooperative parallel growth* of the tips up to the subcritical creasing limit strain, 0.35, of the neo-Hookean half space. On the other hand, easy lateral configurational sliding of smooth fold valleys erratically prompts instability in the *cooperative growth* of the fold fronts, depending on the self-contact friction of the fold surfaces. Such erratic instability elicits large uncertainty in determining the starting strain of fold localization.

On PB-RPD of $\bar{k} < 0.40$, the film surface does not crease, and period multiplications and folding of a wrinkle are found reversible in the corridor of $(0.29 < \bar{k} < 0.40; 0 < \varepsilon < 0.30)$, which is considered useful for various technological applications. Modal irreversibility is observed for $0 < \bar{k} < 0.29$; the critical \bar{k} of irreversible DM1 and QM1

period multiplications are determined as $D_I^R (\bar{k} = 0.17; R = 600)$ and $Q_I^R (\bar{k} = 0.29; R = 120)$ below which DM1 mode and QM1 modes become irreversible respectively. Mode locking during unloading is found the main irreversibility characteristics of the PB system without film/substrate strain mismatch. In contrast, a PB of high film/substrate ratio (*e.g.*, $R = 10^5$) with sufficient strain mismatch (*e.g.*, $\varepsilon_{ps} = 0.4$) and viscosity (*e.g.*, loss tangent $= 2 \times 10^{-4}$) experiences P-period switching from DM1 and QM1 to SM2 and DM2 respectively during unloading. It is found that material viscosity inhibits relative deformation rate of deep valleys of multi-mode wrinkles to that of shallow valleys, and in turn it promotes flipping the curvature of shallow valleys during the unloading cycle. Such flipping triggers P-period switching which provides a jumping mechanism of a multi-mode wrinkle towards a higher energy metastable wrinkle configuration. Here, we expect that excitation of various P-period switching can control stability of cyclic multi-mode configuration hysteresis – cyclic divergence or shake-down. The results may inspire designing new systems with unprecedented surface modes and lead to a new way for period control of various ruga phases.

Chapter 4

The Primary Bilayer Ruga-Phase Diagram

III: Ridging Transitions and Mobility

Bifurcations of Ridges*

*: Part of the results in this chapter had been presented by the author in NewMech workshop 2015 and SES conference 2015.

4.1. Introduction

In the previous chapters, we have constructed a Primary Ruga Phase Diagram for PB system that encompasses all possible ruga-phases and their evolution pathways. The phase diagram was represented by the relationship between the normalized characteristic wavenumber $\bar{k} = \sqrt[3]{3\mu_s/\mu_f}$ and the nominal compressive strain ε . Herein, ruga-instability of a PB system with strain mismatch between the substrate and the film is analyzed. Fig. 4.1 illustrates the primary bilayer system (PB) with initially pre-stretched substrate. As shown in the schematic, a thick substrate with initial length L and thickness $H = 10L$ is subject to a pre-stretch ratio, $\lambda_{ps} > 1$. The initial configuration is shown in Fig. 4.1a_i. It is pre-stretched to the length $\lambda_{ps}L$ in Fig. 4.1a_{ii}. Then, a stress-free film of thickness h and length $\lambda_{ps}L$ is attached to the top surface of the substrate as illustrated in Fig. 4.1a_{iii}. The

two materials are incompressible neo-Hookean materials with shear modulus μ_s and μ_f respectively. Then the imposed pre-stretch on the system is released as schematically shown in Fig. 4.1a_{iv}. We introduce two strain measurements ε_f and ε_s to describe the loading process of the PB system. The substrate loading strain ε_s has the reference of initial specimen length, L , before pre-stretch. Its measurement starts from the no-stretch axis which is marked in Fig. 4.1b. The film loading strain ε_f uses the stretched configuration as the reference state, and it begins at the no-film-strain axis which is marked in red in Fig. 4.1b. The released specimen, Fig. 4.1a_{iv} has the length of $\lambda_{ps}L(1 - \varepsilon_f)$. We define loading direction to have positive strain which gives $\varepsilon_f \geq 0$ and ε_s is negative when substrate is under tension. The two strain measurements thus have the following relationship:

$$(1 - \varepsilon_f)\lambda_{ps} = 1 - \varepsilon_s \quad (4.1)$$

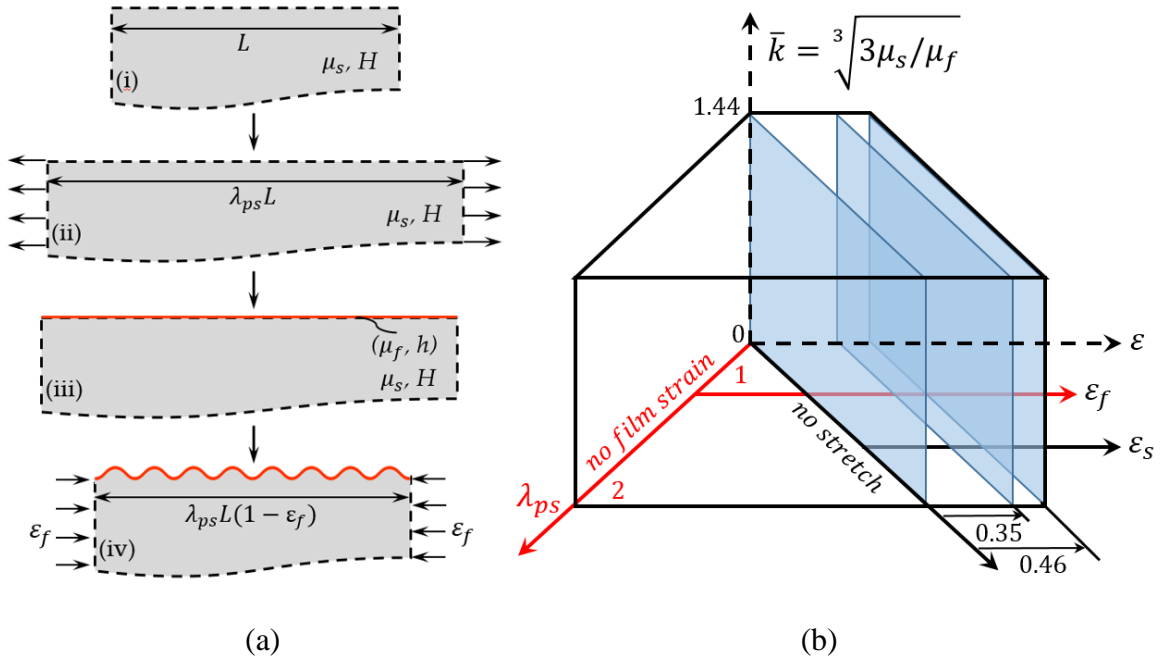


Figure 4.1. Schematics of ruga formation with pre-stretch. Column (a) PB loading system with pre-stretch: (i) initial substrate configuration with length L , depth H and modulus μ_s ; (ii) stretched configuration with final length of $\lambda_{ps}L$; (iii) stress free film with modulus μ_f and thickness h is attached to the stretched substrate; (iv) loaded configuration. Column (b) investigation domain: \bar{k} denotes the normalized characteristic wavenumber; ε is the loading strain and λ_{ps} represents the substrate pre-stretch ratio. ε_f and ε_s axis are the measurements for film strain and substrate strain respectively. ε_s starts from the no stretch axis where the substrate is fully released. The $\varepsilon_s = 0.35$ creasing plane and $\varepsilon_s = 0.46$ Biot plane is marked in the plot.

Previously, we had have constructed a Primary Ruga Phase Diagram for the PB system to show all possible ruga evolution pathways. The phase diagram represented the relationship between the normalized characteristic wavenumber \bar{k} and compressive strain ε . For PB system with substrate strain mismatch, Fig. 4.1b extends the investigation boundary for pre-stretch ratio λ_{ps} and the normalized characteristic wavenumber \bar{k} . \bar{k} is defined as $\bar{k} = \sqrt[3]{3\mu_s/\mu_f}$. The upper bound of \bar{k} is 1.44 which denotes the homogenous half space, while \bar{k} approaching zero represents a stiff film on a soft substrate. Pre-stretch ratios from 1.0 (no stretch) to 2.05 are tested at maximum intervals of 0.1. Three specific planes are marked in the schematic Fig. 4.1b: the zero stretch plane has $\varepsilon_s = 0$ where the specimen has been fully released; the $\varepsilon_s = 0.35$ plane and $\varepsilon_s = 0.46$ plane denote the crease localization plane and the Biot strain plane respectively.

Although it is well known that film ridging is an outcome of substrate pre-stretched PB system and experimental and numerical studies have reported on ridge formation, the

underlying mechanisms of ridging and post-ridging are still unclear. In the following study, we will attempt to answer the following questions: i) Is ridging localization stable? ii) How does ridge evolve under continuous loading? iii) What is the critical pre-stretch for ridging? iv) Is pre-stretch ratio the only governing factor for ridging? Based on the partial understanding of PB system with strain mismatch, in this chapter, we will address the above questions by performing detailed computations and experiments using well-defined systems.

4.2. Computational implementation

The implementation of the simulation of pre-stretch effect on plan strain bi-layer system deformation is based on the computational approach that introduced in previous chapters. The length of the simulation sample is set to be L in X_1 direction and H in the X_2 direction. According to the literature [7, 169], the critical wavenumber for the wrinkling of a stiff film with substrate pre-stretch is

$$k_0 = \frac{1}{h} \sqrt[3]{\Lambda \frac{3\mu_s}{\mu_f}}, \quad (4.2)$$

$$\frac{2\pi h}{l} = \sqrt[3]{\Lambda \frac{3\mu_s}{\mu_f}}, \quad (4.3)$$

$$\Lambda = \frac{1}{2}(1 + \lambda_{ps}^2). \quad (4.4)$$

where h is the film thickness and l is the critical film buckling wavelength; μ_s and μ_f are the neo-Hookean shear modulus of substrate and film; respectively; Λ is the pre-stretch coefficient. Then the dimensionless group is $\frac{h}{l}$ and $\frac{\mu_s}{\mu_f}$. The substrate is first stretched from the initial length L_0 to a specific length L , with pre-stretch ratio $\lambda_{ps} = L/L_0$. A thin film

with length L and thickness h is subsequently perfectly attached to the substrate with stress free condition. The whole system is then released together. Initially, a film material with extremely small shear modulus is applied in order to create a stress-free condition after the whole model is stretched to the pre-defined length. Then, the film material is replaced by the real film material with pre-calculated constants via “model change” command in ABAQUS. Prior to substrate stretching, a small sinusoidal perturbation in displacement in the X_2 direction is applied to the film surface to probe any instability in the system. The stiffest film simulated is 10^4 times stiffer than the substrate. Two other independent variables in the simulation are the pre-stretch ratio(λ_{ps}) and the releasing/compressive strain (ϵ) of the substrate. The pre-stretch ratio varies from 1 to 2.05 in small increments.

4.3. Ruga period and mode control under pre-stretch effect

Evolution of various ruga phases for the PB system without strain mismatch [13] was presented in Chapter 2. Setback creasing instability of the film surface for PB system with $\bar{k} \leq 1.20$ takes place at every four wrinkle valleys when a critical lateral compressive strain is reached for film creasing. Fig. 4.2a1 shows an example where creasing occurs in an interval of four wrinkle valleys for the PB system with $\bar{k} = 0.87$ ($R = 4.5$). For PB systems with $\bar{k} > 1.20$, instantaneous crease is developed with a period even longer than every four wrinkle periods. Homogenous half space ($\bar{k} < 1.44$) creasing has no crease wavelength scale and crease instability happens at Biot strain ϵ . For stiff film PB system ($0 < \bar{k} < 0.40$), the film of the PB without substrate pre-stretch does not crease; instead, folding wrinkles are observed at every four wrinkle valleys after mode quadrupling of the

wrinkle. Fig. 4.2 b1 shows the four-wrinkle-valley-crease for the PB system with $\bar{k} = 0.17$ ($R = 600$).

The question we address now is: If substrate pre-stretch is introduced to the PB system, will the ruga mode and phase development follow the similar evolution pathways as they are observed in pure compression system?

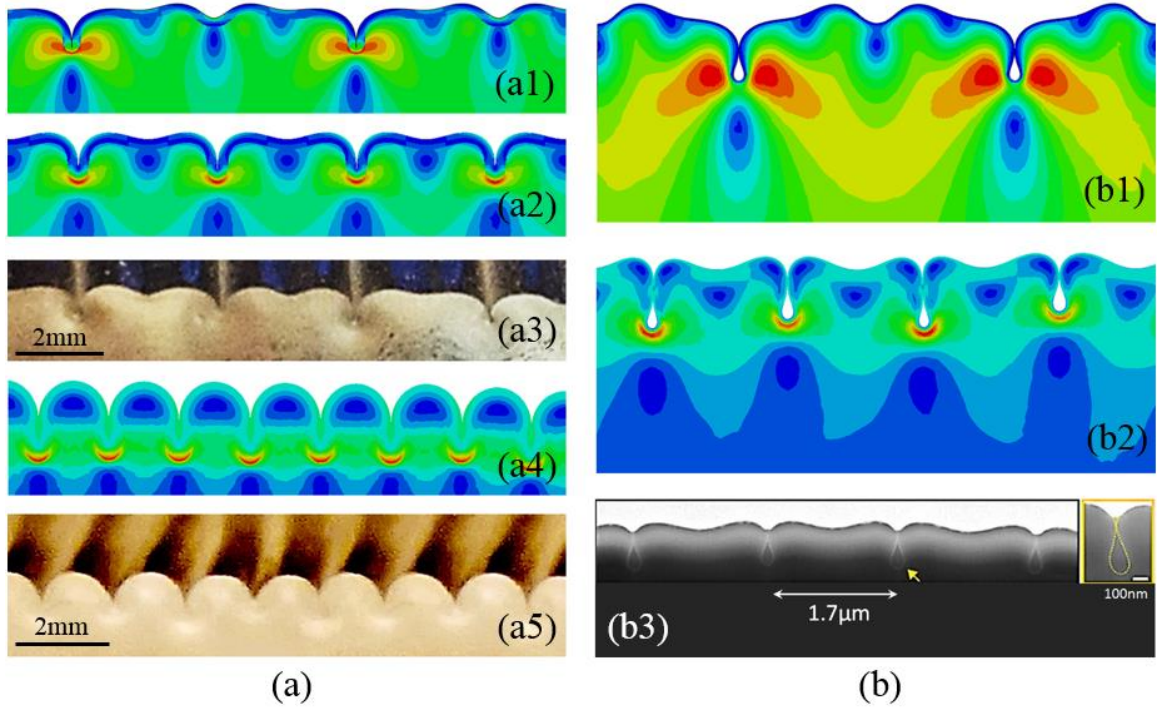


Figure 4.2. Ruga phase period control under pre-stretch effect. Column (a) crease period control; (a1) contour plot of every four valley crease for PB without strain mismatch ($R = 4.5$, $\bar{k} = 0.87$, $\lambda_{ps} = 1.0$); (a2) contour plot of every other valley crease for PB with strain mismatch ($R = 30$, $\bar{k} = 0.46$, $\lambda_{ps} = 1.2$); (a3) experimental results of every other valley crease; (a4) contour plot of every valley crease for PB with strain mismatch ($R = 30$, $\bar{k} = 0.46$, $\lambda_{ps} = 1.8$); (a5) experimental results of every valley crease. Column (b) fold period

control; (b1) contour plot of every four valley fold for PB without strain mismatch ($R = 600, \bar{k} = 0.17, \lambda_{ps} = 1$); (b2) contour plot of every other valley fold for PB with strain mismatch ($R = 1000, \bar{k} = 0.14, \lambda_{ps} = 1.5$); (b3) experimental results of every other valley fold of a stiff skin formed on soft PDMS substrates [165].

4.3.1. Ruga period and mode control for $R > 1$

For a PB system that is under a certain amount of strain mismatch, the strain energy is accumulated in the film before it buckles. This stored energy produces high amplitude aspect ratio wrinkling deformation during continuous loading. These high amplitude aspect ratio wrinkles have large curvature in the valleys which promotes the creasing localization process. Unlike every four wrinkle valley crease that was observed in pure compression PB systems (Fig. 4.2a1), setback creasing can happen at every other valley or even every valley as shown in Fig. 4.2a2 and Fig. 4.2a4 for PB systems that incorporate substrate strain mismatch. The modulus ratio R of the film to substrate in both Fig. 4.2a2 and Fig. 4.2a4 is 30 and the normalized characteristic wavenumber $\bar{k} = 0.46$, while the pre-stretch ratios are 1.2 and 1.8. This implies that the crease period of a PB system with specified modulus ratio can be controlled by substrate pre-stretch level. The system will proceed to global creasing localization under further lateral compression [13]. Experimental verifications of creasing at every other valley and each valley of the PB are shown in Fig. 4.2a3 and Fig. 4.2a5. In the experiment, both the film and the substrate of the PB system are PDMS. The substrate is made by mixing silicone 184 with its curing agent at ratio of 33:1. The modulus ratio of the film to the substrate is roughly 15. The cured substrate is stretched to 120% and a thin layer of liquid mixture of silicone 184 with its curing agent in the ratio of 2:1 is then

attached to the substrate surface. Then the whole specimen is cured in the oven before the substrate is fully released. Further compression is needed to observe film surface creasing. Similarly, in Fig. 4.2b1, for the case of a PB with a stiff film under no strain mismatch, folds are observed at every fourth valley in the presence of a large compressive strain. In a PB system with sufficient strain mismatch, the fold period is reduced by further compressing the fully released substrate as seen in the contour plot in Fig. 4.2b2. This statement has been verified by experiments [165] and results are presented in Fig. 4.2b3. In general, the aspect ratio of wrinkles depends on the pre-stretch ratio. Thus, by controlling the pre-stretch ratio, the period of creasing and folding localization can be designed.

4.3.2. Crease period control for equi-modulus bilayer

For a homogeneous neo-Hookean half space, surface crease is supercritical with respect to defect-induced creasing, and smooth-surface creasing happens at the Biot strain (0.46 compressive strain). The creasing process is global localization, and the evolution is shown in Fig. 4.3a. Fig. 4.3a_i to a_{iii} illustrate the single crease development sequence. The periodic surface strain shown in Fig.4.3 a_i represents the imposed initial perturbation. If we next consider a PB with the same film and substrate material properties, except that the substrate is provided a fixed pre-stretch, will the system still crease at Biot strain?

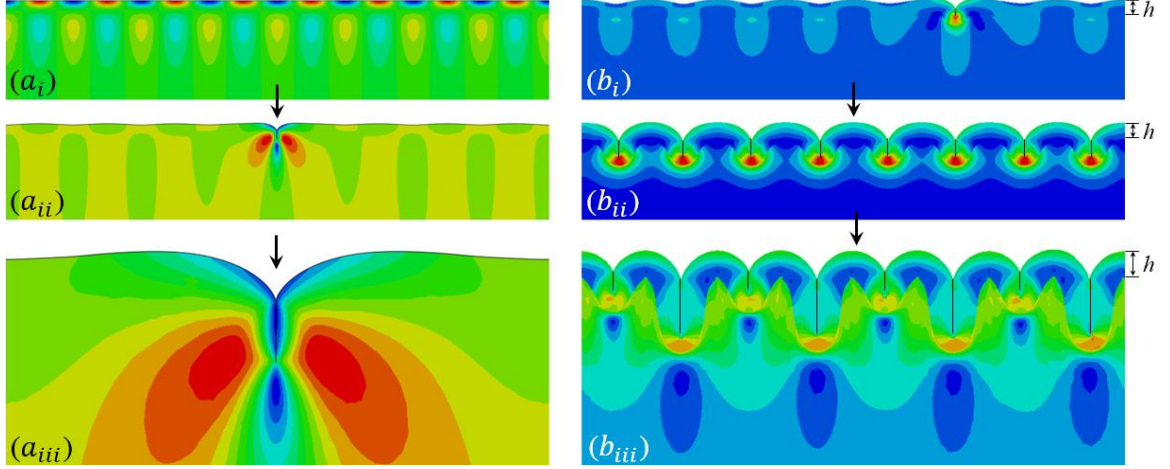


Figure 4.3. Pre-stretch effect on creasing of equi-modulus bilayer. Column (a) represents the crease evolution sequence for homogeneous PB without substrate pre-stretch: (a_i) flat state; (a_{ii}) crease at $\varepsilon_s = 0.45$; (a_{iii}) crease growth at same strain. Column (b) illustrates the crease evolution sequence for equi-modulus bilayer with substrate pre-stretch $\lambda_{ps} = 2.0$: (b_i) single crease initiation at $\varepsilon_f = 0.36$; (b_{ii}) crease frequency multiplication at $\varepsilon_f = 0.50$; (b_{iii}) crease period multiplication and growth at $\varepsilon_f = 0.64$.

During loading, a single crease shown in Fig. 4.3 b_i is observed first when the local film compressive strain reaches the critical strain for creasing. This regional localization is followed by crease frequency multiplication shown in Fig. 4.3 b_{ii} . Since a large strain energy is stored in the substrate before it loses its anisotropy effect to the system, further crease localizations occur when the substrate is released. It is energetically localize in multiple locations elsewhere instead of localizing at the existing crease by growing the creasing amplitude. Why does this happen? For a homogeneous PB without strain mismatch, subcritical crease is global localization of substrate and that requires sufficient energy to be stored in the substrate in order to drive crease growth. On the contrary, for

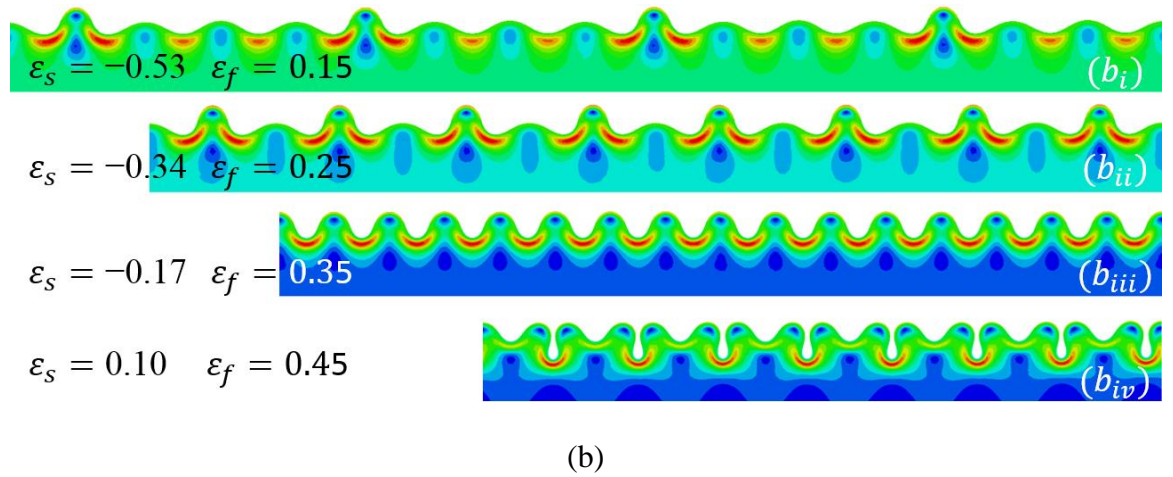
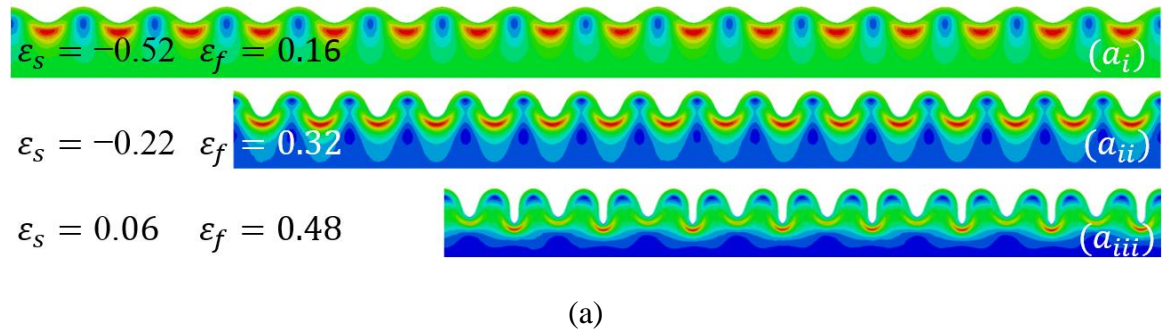
equi-modulus bilayer with large strain mismatch, the energy pre-stored in the substrate is transferred into the film to trigger film surface creasing. While the energy in the substrate is being released, the film experiences compressive strain and develops creases, but the film crease cannot extend into the substrate since the substrate is still under tension. Thus, there is not a viable condition to trigger global localization and global crease localization is suppressed. Consequently, the film can only release the large strain energy from lateral compression by generating multiple creases along the surface. The number of creases would keep increasing until the substrate pre-stretch is almost fully relaxed. With further imposed compression, period multiplication of creasing (doubled crease) shown in Fig. 4b_{iii} is seen.

4.4. Ridging and order-disorder transition

Ridge is a ruga phase which is regarded as a surface outward localization with higher aspect ratio compares to wrinkle. It is well known that ridging is a product of substrate strain mismatch [7]. J. Zang et al. shows that for a PB of neo-Hookean material with a stiff film, ridge localization takes place after wrinkling when the pre-stretch ratio exceeds 1.5 [32, 78]. During substrate release, incipient ridging is usually followed by ridge frequency multiplication. Analogous to the crease frequency multiplication we discussed previously in Fig. 4.3b, ridging is a regional film localization process. Within the pre-stretch effective region, substrate anisotropy will always cause the system to have regional localization followed by frequency multiplication, no matter whether it is ridging or creasing process. In order to release the strain energy transferred to the film from the substrate, the film develops multiple regional localizations. The global localization phenomenon is suppressed for different reasons: For the case of a compliant film PB with large strain

mismatch, it is due to the fact that the substrate is under tension and substrate strain ε_s cannot reach the global creasing strain; for the case of a stiff film PB system, the ridge height limitation suppresses the ability of a single ridge to have global localization. This leads to nucleation of more ridges instead of global localized deformation such as substrate creasing.

With respect to the details of the the ridging process, we next determine if pre-stretch ratio is the only controlling factor to trigger ridging, and what would happen beyond ridge frequency multiplication?



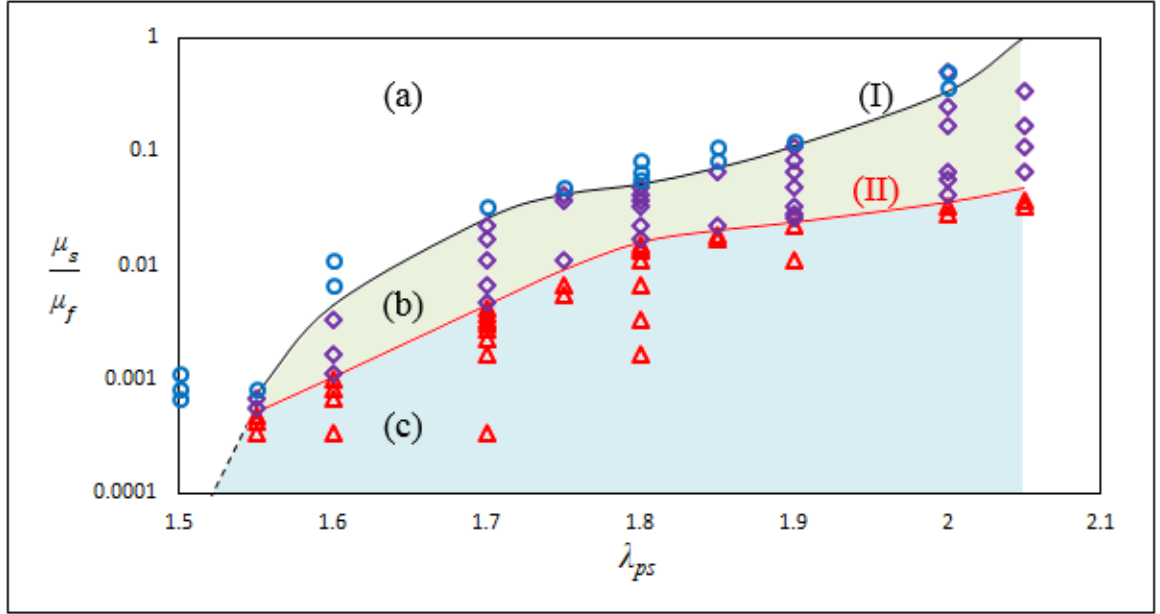
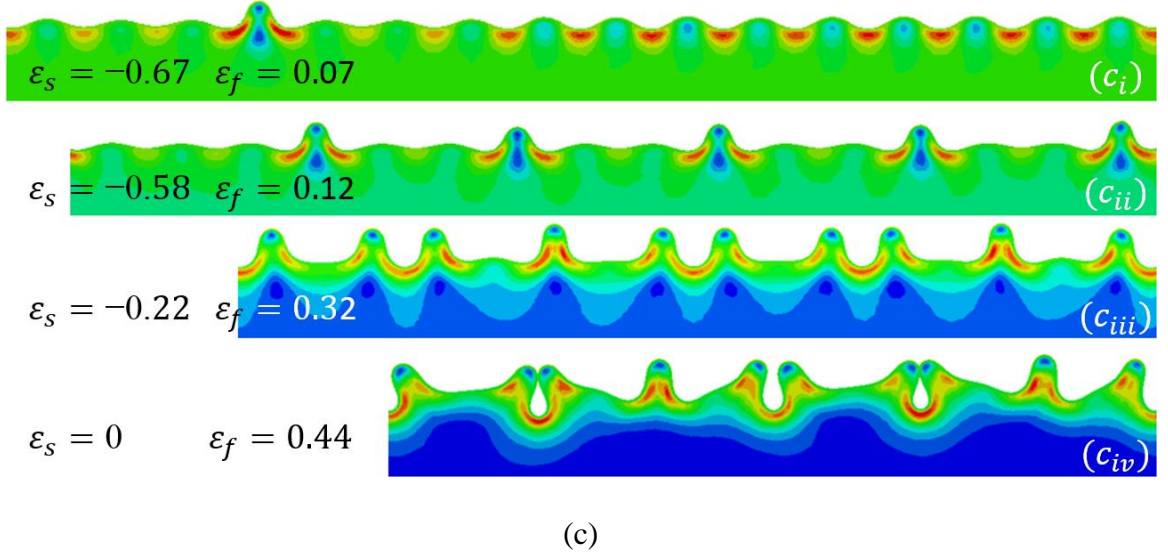


Figure 4.4. Wrinkle-ridge (I) and order-disorder (II) transitions under substrate pre-stretch.

(a-c) shows difference morphological response for pre-stretch ratio $\lambda_{ps} = 1.8$ of various bilayer stiffness ratio R . (a) sequence of normal wrinkle evolution for $R = 18$ ($\bar{k} = 0.55$): (a_i) wrinkling phase at $\varepsilon_s = -0.52$, $\varepsilon_f = 0.16$; (a_{ii}) wrinkle growth at $\varepsilon_s = -0.22$, $\varepsilon_f =$

0.32; (*a*_{iii}) doubling wrinkle phase at $\varepsilon_s = 0.06$, $\varepsilon_f = 0.48$; (b) sequence of ordered-ridge evolution for $R = 60$ ($\bar{k} = 0.37$): (*b*_i) ridging at $\varepsilon_s = -0.53$, $\varepsilon_f = 0.15$; (*b*_{ii}) ridge frequency multiplication at $\varepsilon_s = -0.34$, $\varepsilon_f = 0.25$; (*b*_{iii}) secondary wrinkle at $\varepsilon_s = -0.17$, $\varepsilon_f = 0.35$; (*b*_{iv}) uniform period doubling at $\varepsilon_s = 0.10$, $\varepsilon_f = 0.45$; (c) order-disorder transition of ridging for $R = 600$ ($\bar{k} = 0.17$): (*c*_i) ridging at $\varepsilon_s = -0.67$, $\varepsilon_f = 0.07$; (*c*_{ii}) ridge frequency multiplication at $\varepsilon_s = -0.58$, $\varepsilon_f = 0.12$; (*c*_{iii}) onset of period multiplication $\varepsilon_s = -0.22$, $\varepsilon_f = 0.32$; (*c*_{iv}) disorder and coexistence ruga phases at $\varepsilon_s = 0$, $\varepsilon_f = 0.44$. (d) Phase diagram for wrinkle-ridge and order-disorder transitions: blue circles are data points have no ridging process during releasing; purple diamonds are data points for ridging with order transition; red triangles are data points for ridging with disorder transition; black curve denotes the critical moduli ratio ($1/R$) for ridging respect of substrate pre-stretch λ_{ps} ; red curve represents the boundary for order-disorder transition. The previous three cases (a), (b), (c) are marked in the phase diagram. The boundaries (I) and (II) represent loci of wrinkle-ridge (I) and order-disorder (II) transitions respectively.

4.4.1. Wrinkle-ridge and order-disorder transitions

In our simulations, a wide range of PB modulus ratio R was tested with different values of substrate strain mismatch. It turns out that for substrate pre-stretch ratio larger than 1.50 ($\lambda_{ps} > 1.5$), the PB modulus ratio R needs to be large enough to trigger ridging once the system buckles under loading. Take $\lambda_{ps} = 1.8$ as an example; here, normal wrinkle evolution has been observed for a small modulus ratio, $R = 18$. In this case, the normalized characteristic wavenumber is large and the onset strain of wrinkling is also relatively large according to the Primary Ruga Phase Diagram for bilayer system [13] in Chapter 2. By the

time the film surface buckles, the substrate has already released most of the strain energy stored from the large initial pre-stretch. Under this circumstance, only high amplitude aspect ratio wrinkles are developed due to small substrate anisotropy effect and the wrinkling process is followed by period multiplication as shown by the sequence of normal wrinkle evolution in Fig. 4.4a. Period control of ruga modes as discussed previously in Fig. 4.2 is observed with increasing lateral loading. When the PB has larger modulus ratio ($R = 60$), the strain energy that is stored in the substrate is released during compressive loading on the film, and it is sufficient to cause regional ridging localization after the system wrinkles uniformly. The localization process of ridging concentrates the energy from nearby wrinkles during further release of the pre-stretch and the frequency of the regional ridging localization grows. Subsequently, the substrate gradually loses its anisotropy and the loading strain is still within the reversible zone (Chapter 3). Regional localization is no longer possible at this stage and the system keeps realigning the existing ridges till loading reaches the critical strain for the next level instability---doubling. This process shown in Fig. 4.4b is defined as *ordered-ridge evolution*. By increasing the PB modulus ratio to $R = 600$ which has very small normalized characteristic wavenumber, the system wrinkles at a very early stage, and ridging process takes place right after wrinkling because the large substrate anisotropy leads to enormous potential for regional localizations. As long as the incipient ridging occurs, ridge frequency multiplication and surface self-realignment follows during further release of the pre-stretch. Due to the high stiffness of the film, the ridge amplitude aspect ratio is much higher and large curvature valleys are formed between ridges during the ridge frequency multiplication. However, with further loading, the compressive strain reaches the critical strain for higher instabilities before the surface can

realign the patterns to uniform configuration. For example, according to the PBPD I, the critical strain for doubling decreases with increasing stiffness ratio R . For stiff film system, it doubles at a very early stage so that the ridge frequency multiplication process does not complete to have ordered ridges, and consequently, the surface patterns are highly disordered. If two ridges are close to each other, they form a high curvature valley in between, vice versa. The larger compressive strain in the valleys that have higher curvatures elicits higher instabilities more easily. This process breaks the ridge morphological symmetry and highly irregular surface patterns bring disordering to the system. Ridge folds are eventually formed through ridge contact due to further localizations. This evolution of high amplitude aspect ratio ridges shown in Fig. 4.4c is defined as **order-disordered transition of ridging**. From the three different deformation paths that have been discussed above, we have shown that the evolution paths and ridge modes are highly determined by three factors: magnitude of substrate mismatch strain λ_{ps} , stiffness ratio R and the loading strain ε . The boundary of normal wrinkle evolution, order-ridge evolution and order-disordered transition of ridging for substrate pre-stretch ratio from 1.50 to 2.05 is delineated in Fig. 4.4d. In this plot, $1/R$ is calculated to describe the stiffness ratio and logarithm plot is used to represent the critical modulus reciprocal for each deformation behavior. Above the black curve is ordered-wrinkling evolution zone, where initial wrinkles evolve to doubling wrinkle; between the black and red curve is the ordered ridging zone, where initial wrinkles create ridges which develop ordered folding; below the red curve is the order-disorder transition zone, where initial wrinkles make transition to disordered ridge-folds. A PB system with smaller substrate strain mismatch needs larger PB modulus ratio R to trigger ridging. When substrate pre-stretch ratio λ_{ps}

is less than 1.5, no ridging process is observed under continuous loading. Moreover, in Chapter 3, we discussed that for stiff film systems which reveal irreversibility in higher mode instabilities, the irregularity of surface patterns are also caused by the lack of system self-alignment ability which is due to irreversibility. This leads to multi-period ruga phases and other coexistent phases as shown in Fig. 4.4 c. By this way, disordered ruga patterns will develop. This order-disorder zone separated by the red curve in Fig. 4.4d provides a guide map for engineering manufacturing of well aligned ruga patterns.

It is notable that ruga folds are commonly seen when large deformation is encountered. In pure compression and in the normal wrinkling zone for PB with strain mismatch, a fold is regarded as the production of wrinkle period multiplication. In large stiffness ratio PB systems without strain mismatch, periodic fold only happens in every fourth wrinkling valley. Period of periodic folding can be controlled by introducing small substrate pre-stretch as illustrated in a previous section. With large substrate pre-stretch for a high stiffness ratio PB system, disordered ridge fold can manifest during ridge frequency multiplication at very small releasing strain. Moreover, ruga folding is a delocalization process that prevents further localization by inducing surface self-contact force. Global localization is concentrated deformation and it releases the strain energy that is stored in adjacent ruga patterns. For a PB with large strain mismatch, the high amplitude aspect ratio ridges can easily form ridge folds when disordering takes place during loading. Thus it is very hard to observe global localization in this kind of a bilayer system.

4.4.2. Detection of order-disorder patterns and coexistence of phases

To detect the surface evolution pathways, Fast Fourier Transform (FFT) is used to accurately monitor each transition of ruga modes. Here we choose substrate loading strain

ε_s to investigate the ruga evolution when the PB system is under substrate tension and compression. The vertical axis in the FFT plots represents the amplitudes of all existing wavelengths. Under sufficient strain mismatch of the system, competition of ridging and wrinkle growing can be observed during loading. Initially, wrinkling perturbation with 24 period is applied to the film surface. The critical wavelength λ_0 for wrinkling of the PB system is calculated by equation (4.3). Thus, the total system length is $L = 24\lambda_0$. The major wave frequencies are calculated by

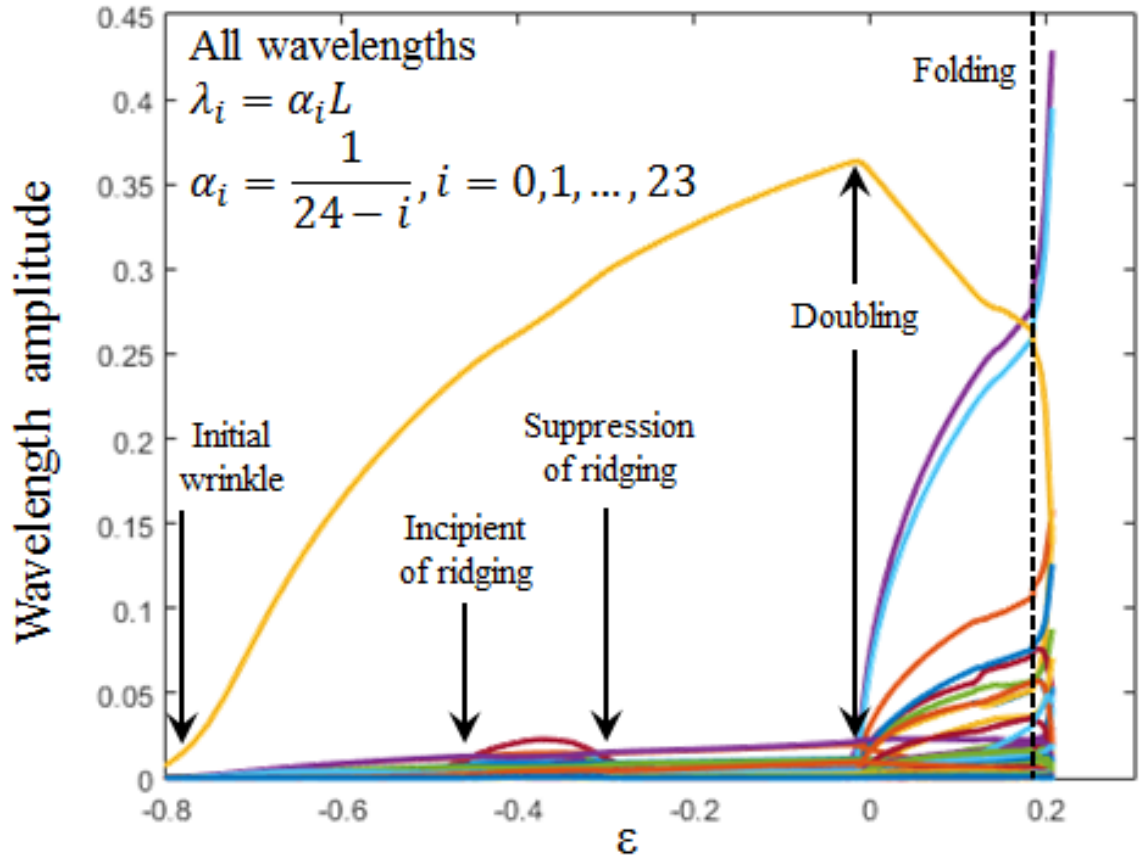
$$\lambda_i = \alpha_i L, \quad (4.5)$$

Where

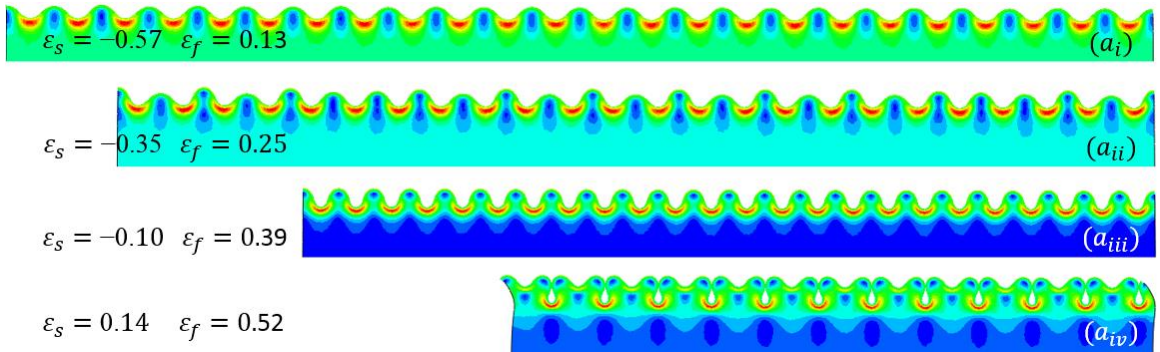
$$\alpha_i = \frac{1}{24 - i}, \quad i = 0, 1, 2, 3, \dots$$

In Fig. 4.5a1, the PB system has properties of $R = 60$ and $\lambda_{ps} = 1.8$. When the system is released from the lateral side, initial wrinkling dominates the surface deformation and the corresponding wave sequence is $\alpha_0 = \frac{1}{24}$. During further loading, the substrate is still under tension while the film is accumulating strain energy and this provides the potential for regional localization to trigger ridging. Though the film surface intends to ridge at a substrate strain of $\varepsilon_s = -0.52$, ridging is soon suppressed by wrinkle-dominated deformation at strain of $\varepsilon_s = -0.30$. The negative value of loading strain means that the substrate is still under tension during the releasing process. This process is marked by incipient ridging and suppression of ridging in Fig. 4.5a1. Further on, the anisotropic effect fades away with increasing loading strain and ridging becomes unlikely. The PB system follows normal wrinkling evolution process and goes through doubling process at a strain of $\varepsilon_s = -0.02$. The corresponding doubling wave sequence is $\alpha_{12} = \frac{1}{12}$. The

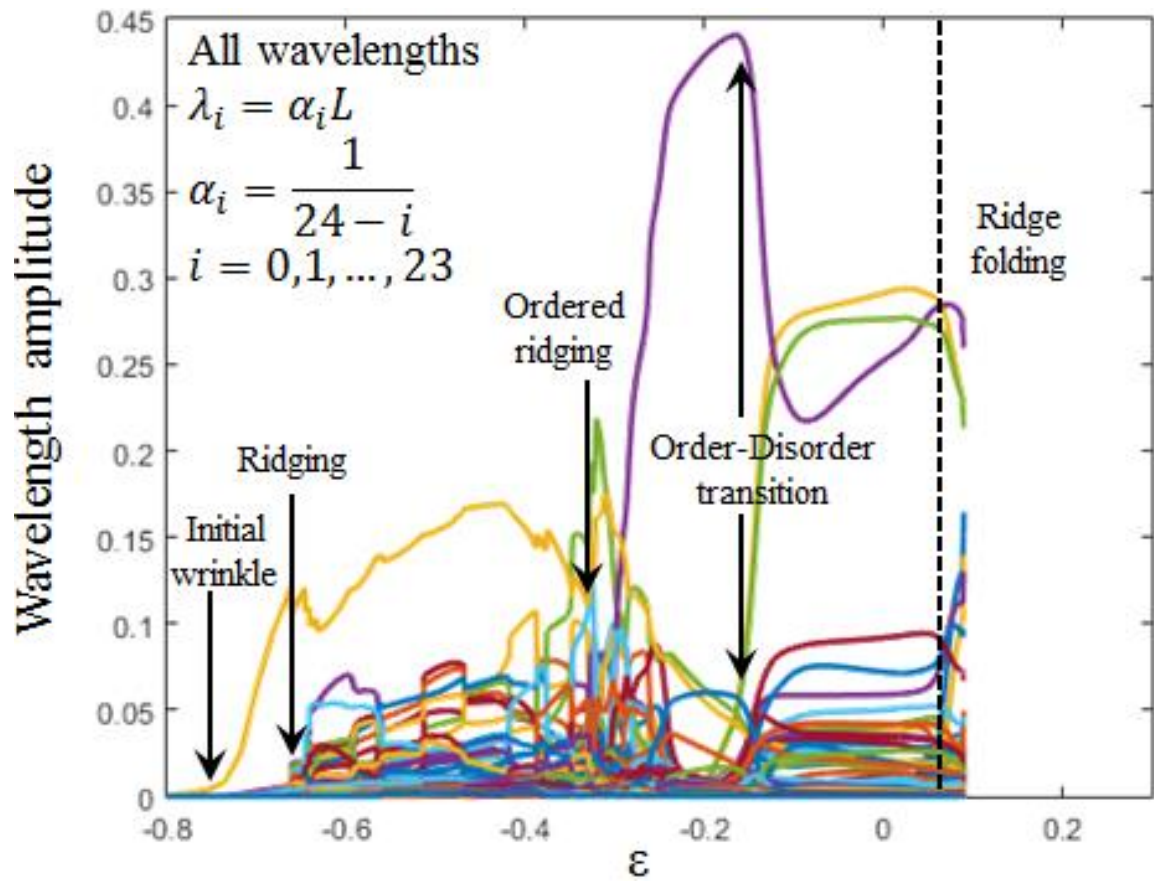
corresponding ruga evolution is called wrinkle-guided deformation and its sequence is illustrated by Fig. 4.5a₂ from (*a_i*) to (*a_{iv}*). Periodic folding wrinkles are observed under further compression.



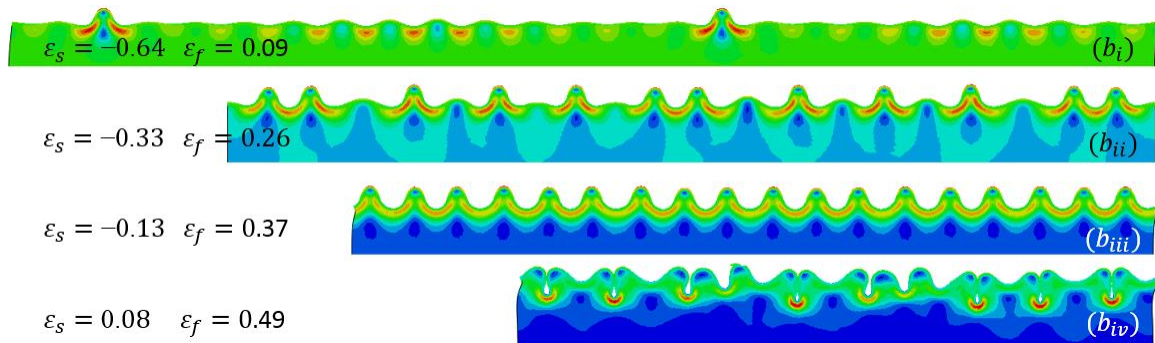
(a₁)



(a₂)



(b₁)



(b₂)

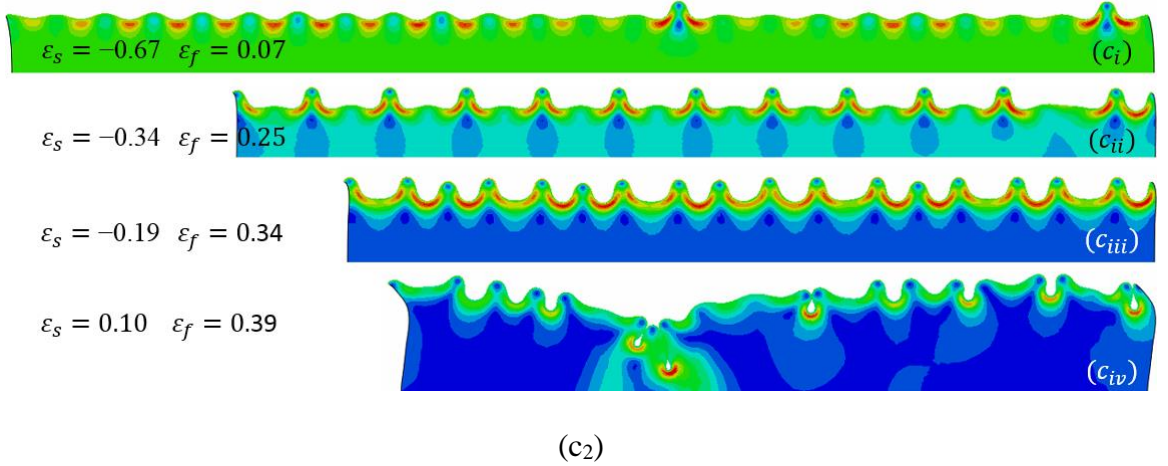
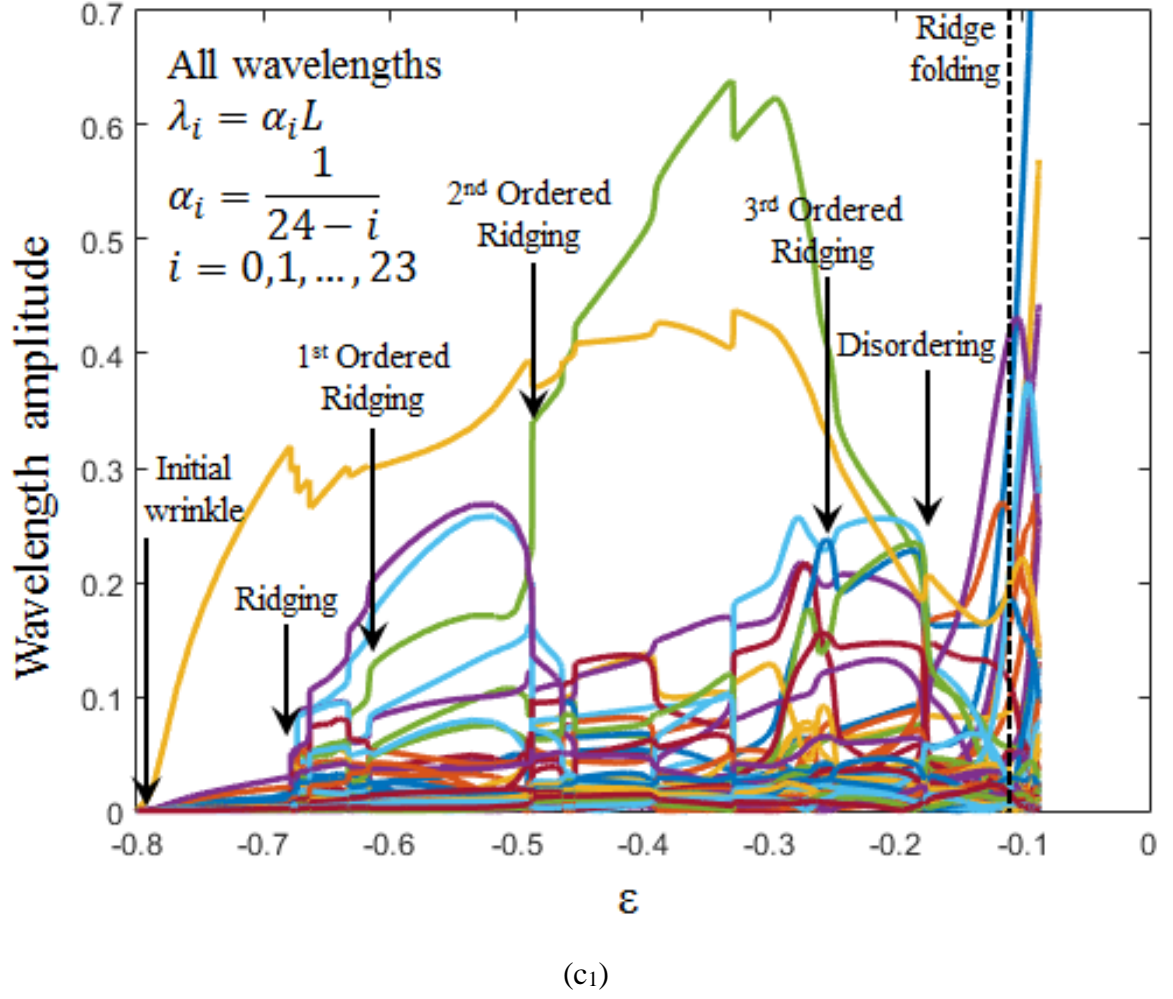


Figure 4.5. Imperfection and film-modulus effects on wrinkle-ridge and order-disorder transitions. (a₁) shows the FFT plot of normal wrinkle evolution of bilayer system ($R = 60$,

$\bar{k} = 0.37$, $\lambda_{ps} = 1.8$) with relative large imperfection amplitude; (a₂) shows the corresponding evolution sequence: (a_i) uniform wrinkling at $\varepsilon_s = -0.57$, $\varepsilon_f = 0.13$, (a_{ii}) incipient ridging at $\varepsilon_s = -0.35$, $\varepsilon_f = 0.25$, (a_{iii}) suppression of ridging at $\varepsilon_s = -0.10$, $\varepsilon_f = 0.39$, (a_{iv}) uniform folded wrinkle at $\varepsilon_s = 0.14$, $\varepsilon_f = 0.52$. (b₁) illustrates ridge order-disorder transition of bilayer system ($R = 60$, $\bar{k} = 0.37$, $\lambda_{ps} = 1.8$) with relative small imperfection amplitude; (b₂) shows the corresponding evolution sequence: (b_i) ridging at $\varepsilon_s = -0.64$, $\varepsilon_f = 0.09$, (b_{ii}) ridge frequency multiplication at $\varepsilon_s = -0.33$, $\varepsilon_f = 0.26$, (b_{iii}) ordered ridge at $\varepsilon_s = -0.13$, $\varepsilon_f = 0.37$, (b_{iv}) disordering and co-existent phases at $\varepsilon_s = 0.08$, $\varepsilon_f = 0.49$. (c₁) shows the order-disorder transition of bilayer system ($R = 600$, $\bar{k} = 0.17$, $\lambda_{ps} = 1.8$); (c₂) shows the corresponding evolution sequence: (c_i) ridging at $\varepsilon_s = -0.67$, $\varepsilon_f = 0.07$, (c_{ii}) ridge frequency multiplication at $\varepsilon_s = -0.34$, $\varepsilon_f = 0.25$, (c_{iii}) ordered ridge at $\varepsilon_s = -0.19$, $\varepsilon_f = 0.34$, (c_{iv}) disordering at $\varepsilon_s = 0.10$, $\varepsilon_f = 0.39$.

When the imperfection amplitude applied to the film surface is reduced, wrinkle-guided contribution to surface deformation is suppressed. As shown in Fig. 4.5b₁ for the PB system with $R = 60$ and $\lambda_{ps} = 1.8$, initial wrinkling with the wave sequence of $\alpha_0 = \frac{1}{24}$ happens at a loading strain of $\varepsilon_s = -0.75$. Instead of following the normal wrinkling evolution, ridging initiates as regional localization at a strain of $\varepsilon_s = -0.67$. With further loading, ridging dominates the post buckling process and the system goes through much more complicated evolutions which are illustrated by FEM contour plot in Fig. 4.5b₂. After incipient ridging, ridge frequency multiplication is triggered. Each small wavelength

amplitude kink in the plot represents a frequency multiplication. In the meantime, the surface keeps realigning the intervals between every other ridge to reach periodic and uniform configuration. The corresponding dominating wave sequence is $\alpha_6 = \frac{1}{18}$. At the strain of $\varepsilon_s = -0.33$, the number of ridge localizations ceases to grow due to the lack of substrate anisotropy contribution, and ordered ridges stably grow their amplitudes under loading. When the local compressive strain at some of the ridge valleys reaches the critical strain for higher instability, the surface localizes irreversibly and this leads to disordering of the system at strain of $\varepsilon_s = -0.15$. At this point, all the wave frequencies start to grow simultaneously and that leads to snap jump. The disordered ridges grow in amplitude with increasing strain till the system is fully relaxed to the length before substrate pre-stretch. With further compression after complete relaxation, the localized ridges generate ridge folds eventually at the strain of $\varepsilon_s = -0.08$ as it is shown in the last frame of Fig. 4.5b₂ from (b_i) to (b_{iv}).

Within the order-disorder transition zone in Fig. 4.4d, ridging governs the surface deformation after the system wrinkles at a very early stage. In the case shown in Fig. 4.5c₁, $R = 600$ and $\lambda_{ps} = 1.8$. Incipient ridging takes place at a strain of $\varepsilon_s = -0.68$. Ridge frequency grows with increasing loading strain and is coupled with simultaneous surface self-realignment. The first ordered ridging configuration is reached at a strain of $\varepsilon_s = -0.63$ and is followed by ridge amplitude growth during continuous loading. At a strain of $\varepsilon_s = -0.49$, a second ordered ridging period begins, resulting in another level of ridge frequency growth. The third ordered ridging process commences at a strain of $\varepsilon_s = -0.25$ with the final number of ridges for this specific system before the lateral loading strain reaches the critical value for higher order instabilities. The disordering transition causes by

random regional localization is observed at a strain of $\varepsilon_s = -0.18$, and it forms ridge folds with progressive releasing. The whole surface evolution from ordered wrinkling to disorder ridge folding is completed during the course of the relaxation of the initial substrate pre-stretch. The evolution sequence is shown in the last frame of Fig. 4.5c₂ from (*c_i*) to (*c_{iv}*).

4.4.3. Ruga mobility bifurcations

The previous discussions show that ridge evolution starts from single ridge localization and evolves into ridge frequency multiplication followed by order-disorder transitions. Ridging, is a growth limiting localization. Energetically speaking, if the energy provided by lateral compression cannot surmount the energy barrier to make an existing ridge grow higher, the system will nucleate new ridges elsewhere to release the energy. When the ridge number grows with increasing loading strain, the existing ridges have very high mobility to move around and realign the intervals between each other in order to reach a uniform patterning configuration. Configurational driving forces enable two ridges to interact with each other through the stress field. They can either push away or pull close to each other. While moving a self-symmetric ridge, the energy loss of the front of a ridge can be gained at the back. On the contrary, when translating an asymmetric ruga feature, the energy change from the front and back is not balanced, and that makes it difficult for it to move around. Its mobility goes down. Before disordering, the ridges have equal mobility and the system retains relatively ordered and well-aligned patterns. During the order-disorder transition however, the higher instability deformation triggers localizations at the valley of ridge pairs. Some ridges lose their symmetry in some locations and other don't. This will bring the inhomogeneity of the ruga mobility along the surface and system becomes disordered. The order-disorder transition is then considered to be mobility bifurcating

process. Energetically, there are two modes for ridge evolution after its frequency multiplication: *symmetry breaking mode* and *translational moving mode*. When a single ridge breaks its self-symmetry, it can no longer move around since it is energetically more favorable to move a symmetric feature along the surface. For a distorted ridge, recovery of the symmetry is needed before moving it along the surface. However, once the ridge is distorted through higher instability deformations, it is not likely to recover its symmetric shape with increasing lateral loading. Instead, it localizes deeper at the valley and loses its translational mobility permanently.

If we consider the ruga evolution energetically from the very beginning of loading to very large deformation of the surface, the system basically goes through five energy transfer states. (i) Ridging forming state: at very early loading stage, the strain energy is released by forming a single regional surface upward localization, which we called a ridge; (ii) Ridge amplitude growth state: increasing energy leads to ridge amplitude growth till its height limitation; (iii) Ridges realigning state: when a single ridge reaches its growth limitation, the accumulated energy causes the nucleation of ridges elsewhere far away from the previous ridge, and it is followed by realignment of ridges with full mobility. The current mobility mode is translational mode; (iv) Distorting state: with further lateral loading, the local compressive strain in some locations along the surface reaches the critical strain for higher instability, and the energy used to create relative movement of the ridges in the previous state is now transferred to distort ridges. The translational moving mobility mode of a ridge then turns to symmetry breaking mobility mode and brings disordering to the system; (v) Further localizing state: the disordered ruga phases keep developing through the strain energy released from the lateral compression.

4.5. Ruga order-disorder transition for 2D systems

In a two-dimensional (2D) PB system subjected to biaxial loading, the deformations in two directions couple to form much more complicated ruga. We constructed a 2D neo-Hookean bilayer to investigate the ruga evolution under equi-biaxial loading. Fig. 4.6 compares computational and experimental results. In the simulation, a bilayer block with the stiffness ratio $R = 80$ and square cross section in the XY plane and infinite depth in the Z direction is used. Surface imperfection with very small amplitude ζ is applied to the film top and is described by

$$z = \zeta \cos(\pi X/\omega) \cos(\pi Y/\omega) \quad (4.6)$$

where ω is the critical wavelength and follows the same calculation as for the 1D PB system; the amplitude ζ has the following expression

$$\zeta/\omega = 0.0001 \quad (4.7)$$

The ruga evolution in 2D system can be expressed by “I-L-T-Y” transitions. “I”, “L”, “T”, “Y” are possible ruga junction types that have been observed in the evolution. As shown in Fig. 4.6a_{it}^t, “I” shape ruga is initiated at the early buckling stage when the compressive strain is $\varepsilon_s = 0.05$. At this moment, surface deformation is dominated by 1D wrinkling. “I” shape rugae group up and connect with other “I” groups at right angle to form periodic patterns. With increasing loading, “L” shape ruga develops from “I” junctions by herringbone transition. Due to the coupling of two dimension loading, multiple constant slope crinkles are found during labyrinth transition from “L” to “T” junctions. These ruga features can be seen at the cross sections of the 2D specimen in the experiment (Fig. 4.6b_{it}^c) and in the simulation (Fig. 4.6a_{it}^c). Disordered patterning gradually shows up by out of

plane corrugation is illustrated in the film top view in Fig. 4.6a_{ii}^t with compressive strain $\varepsilon_s = 0.16$. Upon further compression, more complicated higher order instability combined with two dimensional deformation coupling leads to crumpling transition from “T” to “Y” junctions. This gives more out-of-plane corrugation, and at the compressive strain of $\varepsilon_s = 0.24$, the surface is fully disordered by grouping of high frequency folding as shown by the top view FEM contour plot in Fig. 4.6a_{iii}^t, together with the experimental results in Fig. 4.6b_{iii}^t. The corresponding cross section views are shown in Fig. 4.6a_{ii}^c and Fig. 4.6b_{iii}^c. Since 2D ruga evolution is closely related to the decaying and growing of the four possible junctions, the loading configuration can be identified by analyzing the population density of each junction type.

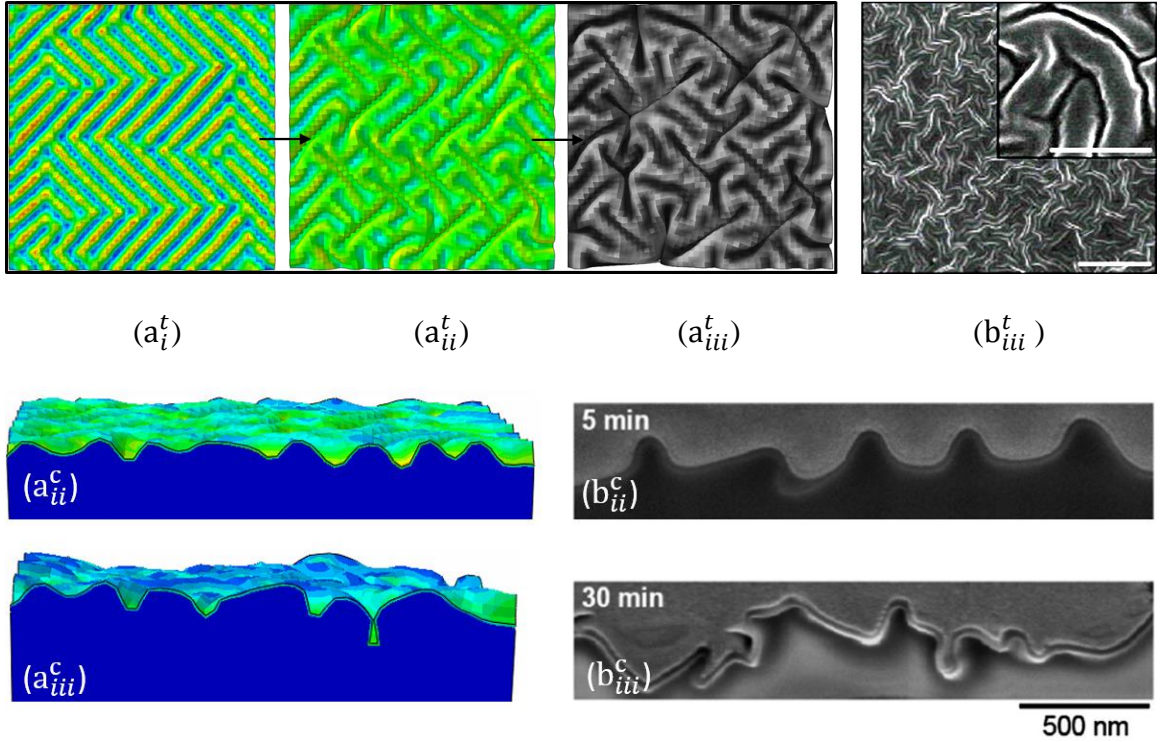


Figure 4.6. Order-disorder transitions of 2D ruga: simulation and experiment. (a_i^t) to (a_{iii}^t) shows the top view of 2D ruga evolution under compressive loading; (b_{iii}^t) is the experimental comparison for (a_{iii}^t) , shows SEM micrograph of the wrinkle patterns on PDMS substrates with amorphous carbon deposition time $t = 30$ s; (a_{ii}^c) and (a_{iii}^c) are the corresponding cross section view for (a_{ii}^t) and (a_{iii}^t) ; (b_{ii}^c) and (b_{iii}^c) are the experimental cross section comparison [10] for (a_{ii}^c) and (a_{iii}^c) , showing FIB cross-sectional image of an amorphous carbon film on PDMS with different deposition times.

Upon even larger deformation strain, “Y” junctions start to overlap with each other and the tessellation transition forms a layer of new global film with an effective stiffness [10]. This newly generated bi-layer system generates the possibility to have longer wavelength deformation when the system is compressed further. This hierarchical disordering is found in experiment with multi-wave corrugations [158] which has been shown in Fig. 1.1d. Biaxial loading is more complicated compared to one dimensional loading. What we have discussed above is the special case of equi-biaxial loading where the specimen is loaded at the same strain in both X and Y directions simultaneously. There are however many other loading modes such as asynchronous biaxial loading and biaxial loading with different strains in each of the two directions. The deformation coupling from two-direction corrugation will be diverse with different loading strategy, and will delineate the loading path dependency of 2D ruga evolution.

4.6. Conclusion

Different consequences of various strain mismatch to a model PB system regarding changing stiffness ratio has been investigated in this chapter. A phase diagram for ridging is constructed accordingly. Ridging occurs beyond the critical pre-stretch and is a function of stiffness ratio. The relationship between the critical moduli ratio for ridging for pre-stretch ranging from 1.5 to 2.05 is provided. For $\lambda_{ps} > 2.0$, ridging can happen with any modulus ratio. Out of the ridging zone, period of particular ruga phases such as crease and fold can be controlled by tuning the intrinsic modulus ratio R and extrinsic substrate pre-stretch of a PB. For equi-modulus bilayer, the surface has a single crease in the beginning and goes through frequency multiplication just as post ridging at an early stage. Further period multiplication of creases is observed after the substrate is fully released or even subject to small compression. Within the ridging zone, order-disorder transition of ridge folding has been discovered in high stiffness ratio bilayers. In the order transition zone, the system realigns the surface patterns after ridging to have uniform stable secondary wrinkles which is followed by period multiplications; in the disorder transition zone, realignment of ruga pattern at the early stage is incomplete when the compressive strain reaches the critical strain for higher buckling instabilities such as doubling and quadrupling. Regional localization prefers to take place at valleys with larger curvature, and this leads it one step further to break the surface symmetry and periodicity of ruga phases. Disordered patterns and coexistent ruga phases will develop upon further compression. Moreover, the surface follows wrinkle-guided deformation with large initial imperfection amplitude and goes through normal post buckling evolution under progressive loading. This provides a way to avoid regional ridging localization under large substrate pre-stretch and keeps the

regularity and periodicity of demanded ruga patterns with controllable wavelengths. Finally, the order-disorder transition concept is verified in a 2D bilayer equi-biaxial loading system with experimental comparison. “I-L-T-Y” transitions are introduced to characterize the ruga evolution and by analyzing the population density of each junction, it is possible to identify the current loading stage. Tessellation and hierarchical disordering with longer wavelength will be found with large deformation strain. The patterning of 2D ruga evolution is highly path dependent due to the diversity of biaxial loading methods.

Chapter 5

Ruga Morphological Control

5.1. Introduction

In previous chapters, bi-layer system surface deformation is discussed for both pure compression case and the case with substrate strain mismatch. Various ruga phases such as doubling [3], quadrupling [3], folding [6], creasing [38, 73, 90, 92, 105] have been found experimentally in recent studies. Ruga phases and their distributions varies with the type of soft material system and the physical properties of the system. Following review states the possible existing configuration of various surface ruga phases before the global localization. It is well understood that for homogeneous half space, the only possible ruga phase is crease. As we discussed in Chapter 2, creases and folds can only take place at every four wrinkle valleys for a PB without strain mismatch; period multiplication starts with single mode wrinkling to doubling, and it stop at quadrupling due to the contact force induced by folding. In Chapter 4, we show that with substrate pre-stretch, ridge can be triggered for systems have large enough modulus ratio. Knowing the existing ruga phases based on current studies, now question arises: how do we control the ruga morphology in a soft material system? From what kind of system can we get desired ruga phase with specific morphological and physical properties? In Chapter 3, excited ruga mode switching is found through cyclic loading when the system is subject to sufficient viscosity and strain mismatch. In the fourth chapter, we use bi-layer PDMS to experimentally verify that ruga

phase period can be controlled with substrate pre-stretch ratio and modulus ratio of the PB. Every other wrinkle valley crease and every wrinkle valley crease are observed. Similarly, fold is found to occur at every other wrinkle valley of a stiff skin formed on soft PDMS substrates [165] instead of every fourth wrinkle valley fold in pure compression system. This chapter will try to solve the following question: Other than ruga period control, what else aspects of ruga morphology can we control to make better use of the soft material systems? Can ruga transition such as ridging be suppressed even the soft substrate is encountered very large pre-stretch?

This chapter aims to link all the ruga phases that we have observed from different soft material systems in previous chapters together and investigate their potential controlling aspects. A specific ruga morphological controlling will be shown experimentally through a loading test of a PDMS specimen with oxidized top surface and large strain mismatch. The corresponding control factors for various ruga control aspects are discussed and summarized to guide the broad range of applications in both industrial and researches.

5.2. Experimental setup

The home-made loading device is used to implement uniaxial stretching/ releasing of PDMS samples. It is designed to fit in the UV light chamber for oxidation when the specimen is loaded under tensile stress. The manufactured assembly is shown in Fig. 5.1a. The loading device is composed of three main parts: stationary base plate (A), self-tightening grip pair (B) and the translational stage (C) with attached removable actuator (D) and its control module (E). The translational stage connects to self-tightening grip

through a universal joint, to avoid any locking of movement that caused by slightly non-collinearity error from the manufactured parts. The self-tightening grips are tied with springs, which ensure sufficient pressure applying on the specimen surface to avoid sliding. The gap between the two rollers from a single grip narrows, when the specimen thickness decreases upon stretching. The grip pair is able to slide smoothly along the slot in the base plate through the bearings. The PDMS specimen can be loaded/ unloaded at a demanded rate that controlled by the actuator attached to the translational stage. Fig. 5.1b illustrates the design of the self-tightening grip pair. The four rollers are used to have direct contact with the soft specimen and their surfaces are gridded to enlarge the contact roughness. The relative position of translational stage can be locked after the specimen is pre-stretched to required length. Without the actuator and its controller, the whole device can fit into the UV light chamber for surface oxidizing process. The fitted configuration is illustrated in Fig. 5.1c.

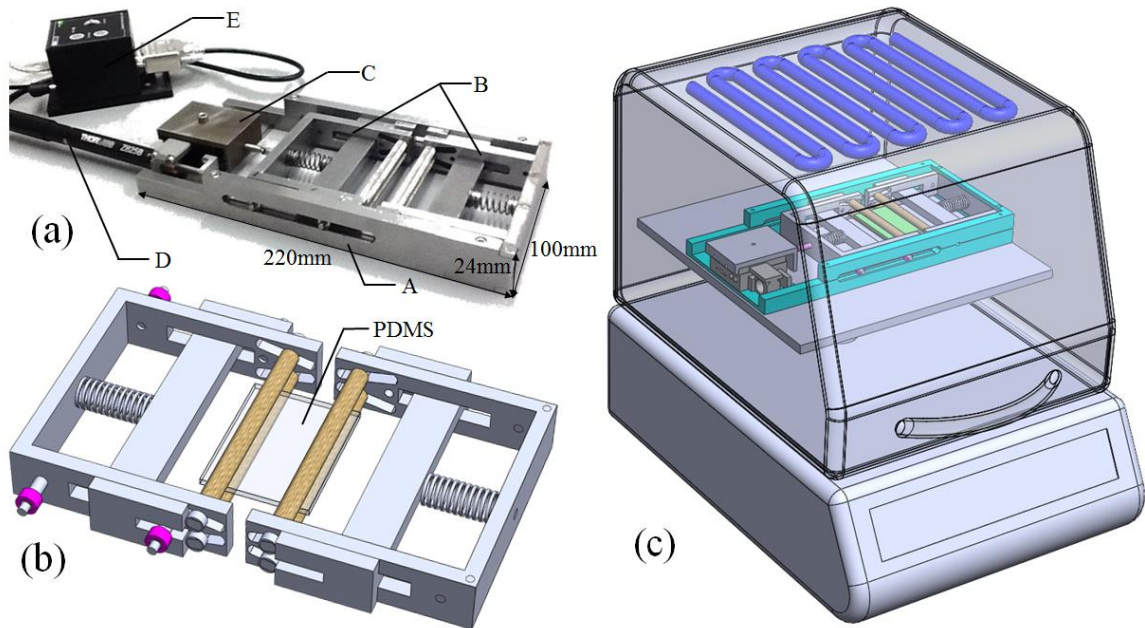


Figure 5.1. Experimental setup. (a) Manufactured self-tightening loading device: (A) base plate, (B) grip pair, (C) translational stage, (D) actuator, (E) control module; (b) exaggerated view of grip design; (c) loading device fit in UV light chamber.

The PDMS sample has the silicon base and curing agent mixture ratio of 10:1. After well mixing, the mixture is sent to the vacuum chamber to be deoxidized for 20 minutes. Then it is cured in the oven overnight at the temperature of 75F. After cooling down, the PDMS is cut to a rectangular shape which has the size of 20 mm \times 10 mm with thickness 1.5 mm. It is then stretched by the homemade self-tightening loading device to 200% ($\lambda_{ps} = 2.0$) and then treated by UV light for 2 hours. A very stiff layer is generated on the top surface due to oxidation. The PDMS sample is then released gradually on the loading device. The releasing rate and amount is controlled by the actuator attached to the loading device and the whole deforming procedure is recorded in situ by the camera on the interference microscope.

5.3. Results and discussions

In this section, experimental observations of surface ruga features are discussed. Since the oxidized PDMS has a very stiff film on top surface, it is compared with bi-layer system which we have investigated in previous chapter. For a stiff film bi-layer system with very large substrate pre-stretch, ridging initiates at very early stage of loading. Disordering is found during releasing which reflects to highly distorted and asymmetric surface patterning. In the case of oxidized PDMS, will it follow the ridging transitions as what we

expect in bi-layer system? By comparison, we will delineated the different behavior of these two soft systems by analyzing their physical property discrepancies.

5.3.1. Ridge suppression in graded modulus system with large strain mismatch

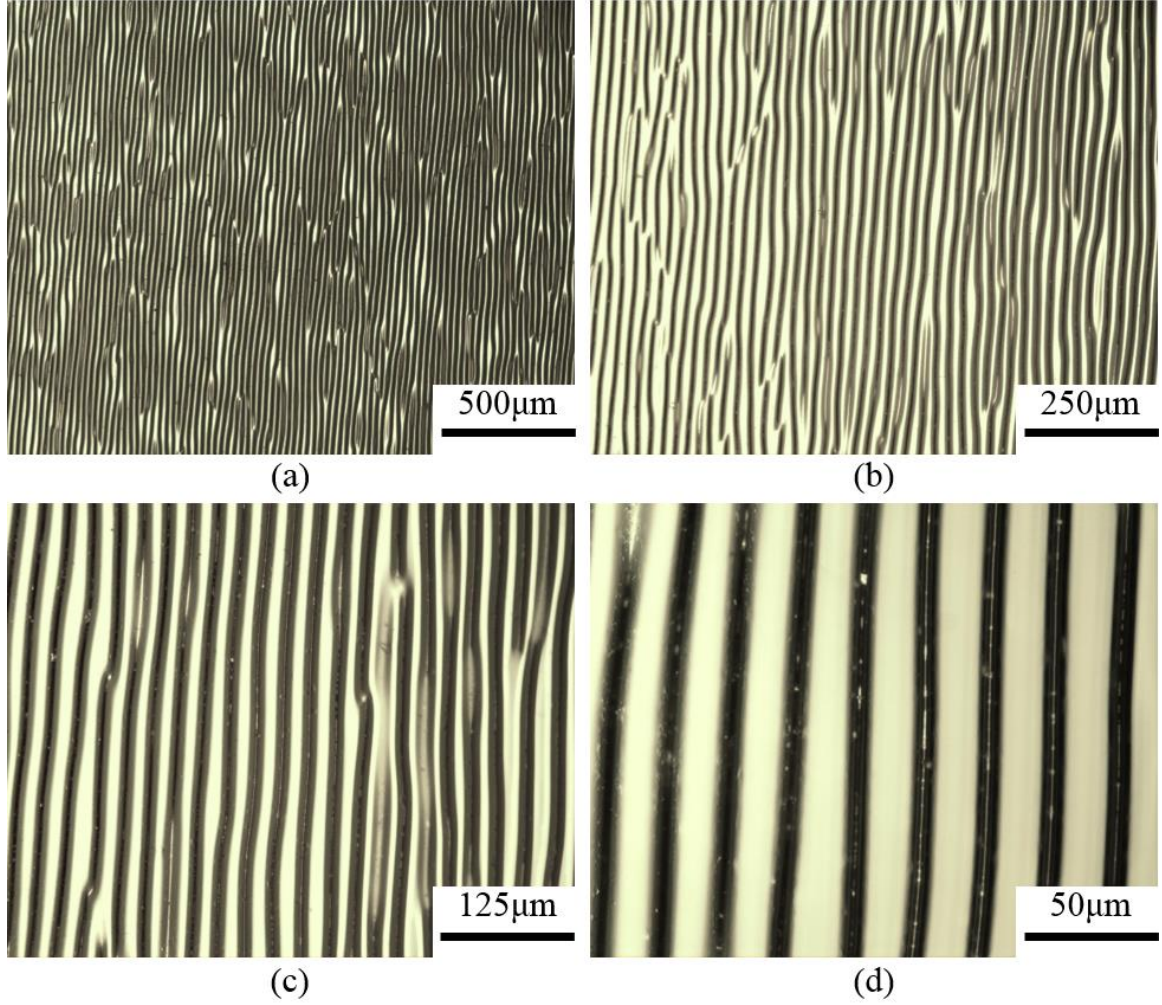


Figure 5.2. Ruga patterns on a pre-stretched oxidized PDMS surface detected by regular optics. The magnification rate increases from (a) to (d).

Fig. 5.2 shows the ruga patterns on the PDMS surface after it has been fully released. The magnification increases from (a) to (d). The ruga patterning indicates that ridging can be avoided in multi-layer structures even the soft substrate has enormous pre-stretch. In

Fig. 5.2a and Fig. 5.2b, a large number of wrinklons are seen on the surface. A wrinklons is a junction of two wrinkles. It is triggered when two wrinkles merge to one or one wrinkle branches out into two. During releasing, wrinkles start to form regionally on the PDMS surface and spread out with increasing loading strain. When the wrinkling groups meet with each other, the misalignment of wrinkling strips leads to wrinklons junctions while merging. The wrinklons transitions cause variation of local effective compressions which leads to inhomogeneity. Some surface region has more compression and some has less. The high compression zones are more likely to trigger period multiplications and the less compression zones remain normal single period deformation. More of coexistence will be discussed in following parts. Wrinklons are also mysteriously commonly found as groups in which they line up at oblique angles. During oxidation, the sample experiences complicated chemical processes. At different depth to the sample surface, material has different Poisson ratios (needs verification). When the sample is been released from the stretched direction, the free lateral direction will try to expand back to initial size. If the lower layer expansion is less than the upper layer expansion, strain mismatch will be induced during loading. This leads to relative compression on the free lateral side and it couples with loading direction deformation to create a 2D loading system upon small strain. Recall the early loading stage of a 2D bilayer system, orthogonal herringbone shape ruga is observed at 45 degree to the loading direction. Similarly, the lined up wrinklons are also found to be at 45 degree lines and their lining directions varies from region to region just like herringbone patterning. Why is the 2D deformation behavior revealed at the place where wrinklons group up? In the experiment, 1D wrinkling evolution dominates the deformation, while the condition for 2D deformation patterning is to break the translational

symmetry of wrinkling stripes. It is very difficult to perturb a perfect wrinkle pattern without large external force. On the contrary, wrinkle itself is regarded as an asymmetry factor in the system. Thus, the herringbone shape caused by 2D small strain deformation is more likely to happen within wrinkle groups. This 2D deformation behavior brings another kind of coexistence phases with 1D dominated surface deformations.

In order to investigate the morphological features of the deformed oxidized PDMS surface, higher resolution interference microscope Zygo is used. A rectangular region 0.140mm x 0.105mm with five uniformly aligned ruga stripes is scanned as shown in Fig. 5.3. In this figure, (a) shows the top view of ruga patterning which is obtained from the interference fringes in (b). Fig. 5.3c illustrates the oblique view, from which we can have a direct understanding of the shape of stripes. The average wavelength and amplitude of each stripe can be calculated with the data in Fig. 5.3d: $l = 25\mu\text{m}$, $h = 6.4\mu\text{m}$. Due to the fact that the stripes are very close to each other and crease or folded wrinkle feature may exist at the valleys, there is not enough light to get to the deeper part of the stripes. But we can still observe the zigzag shape at the lower part of the visible stripe. Will that be another generation of wrinkles? To prove this hypothesis, we need even higher resolution equipment which will be discussed later.

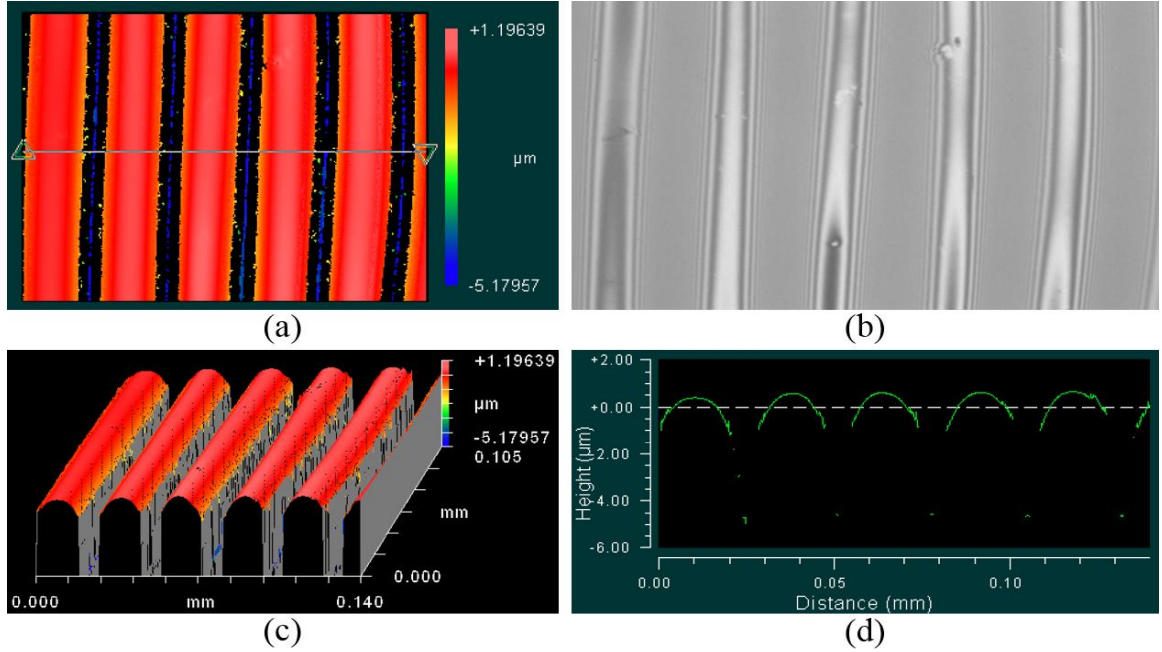


Figure 5.3. Ruga shape observed by interference microscope Zygo: (a) top view of ruga stripes; (b) interference fringes of scanned region; (c) oblique view of (a); (d) the amplitude and wavelength measurement of the ruga patterns.

According to previous chapters, for a bilayer system with very large substrate pre-stretch, ridge should be expected during releasing. With large loading strain, order-disorder transition will take place and reflects to ridge fold eventually. On the contrary, in our experiment, no ridge formation is observed during releasing as shown in Fig. 5.2. Why does this happen? A recent research study on modulus measurement of a PDMS specimen with oxidized surface [4] implies that, UV light treated PDMS cannot be correctly represented by simple bi-layer system. In Fig. 5.4, the modulus distribution of the oxidized PDMS along the depth direction indicates the multi-layer film property of oxidized PDMS. Fig. 5.4 A and (C) show the AFM measured contact stiffness along the fractured surface of sample. The X_2 axis is in the depth direction. Fig. 5.4A shows the measurements of the

region $(0 - 5)\mu\text{m}$ which is very close to the surface. The corresponding Young's modulus plot is shown in Fig. 5.4B, from which we can clearly identify a very stiff thin film followed by a soft layer before it goes back to stiff again and gradually decay with the depth. This kinked modules distribution is due to the chemical reaction process during PDMS oxidation. Fig. 5.4C illustrates the decayed modulus surface with a stepped decreasing trend far from the top surface. The Young's modulus distribution is shown in (D).

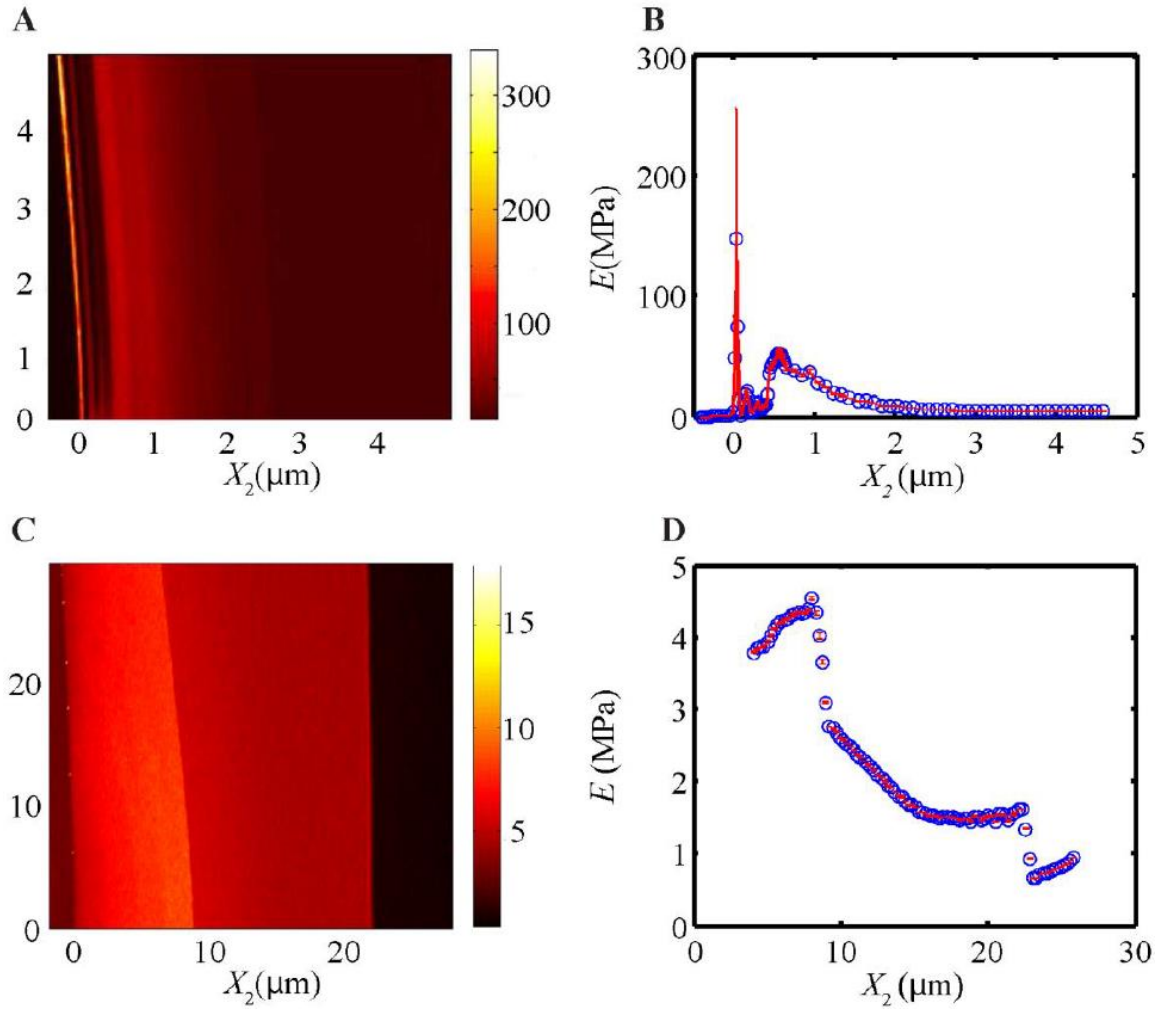


Figure 5.4. AFM measurements of Young's modulus of the oxidized PDMS as a function of depth from the free surface. A, C: a contour plot of the contact stiffness along the fractured surface of the sample as measured by AFM; B, D: corresponding Young's modulus as a function of depth from the free surface [4].

5.3.2. Hierarchical wrinkles and co-existent phases in graded material with kinked modulus distribution

In the past decade, hierarchical wrinkles has been observed by Efimenko et. al [9]. Later, the hierarchical wrinkles could be experimentally reproduced by M. Diab, et al. [4], and their careful measurement of elastic modulus distribution along the depth of the film revealed that the hierarchical wrinkles are made by multi-layer effect not by sequential bifurcation of wrinkles. Based on the existing literatures and the discussions from previous section, we have following questions: Does the discrepancy of modulus distribution elicit the different path of ruga evolution? What are the necessary conditions for hierarchically wrinkling? Based on the oxidized PDMS modulus measurement (Fig. 5.4 [4]), at least three effective dominating film layers together with the soft substrate and their corresponding thicknesses should be taken into consideration to model the multi-layer system. Fig. 5.5 simulates the oxidized PDMS with substrate strain mismatch ($\lambda_{ps} = 2.0$). It is model by multi-layer structure and the modulus distribution follows the measurements in Fig. 5.4. As illustrated in Fig. 5.5a, attached to the soft substrate, there are three thin layers l_1 , l_2 and l_3 . The corresponding modulus for each film layer is $\mu_{l1} = 260MPa$, $\mu_{l2} = 5MPa$ and $\mu_{l3} = 60MPa$ according to the data in Fig. 5.4B. Substrate modulus is set to be $\mu_s = 1MPa$. The thickness ratio of the layers is $h_1:h_2:h_3:h_s = 1:3:6:\infty$. The model simulates

24 waves at onset of wrinkling. The coloring of contour plots in Fig. 5.5 represents the maximum in plane principal strain. Plots (b1)-(d1) illustrate the ruga evolution of this three layer/ substrate structure. (b2)-(d2) show the corresponding exaggerated wrinkle valleys which clearly reveal higher frequency waves due to large local compressive strain. We introduce two strain measurements ε_f and ε_s to describe the loading process. The film loading strain ε_f use stretched configuration as reference state. The released specimen has the length of $\lambda_{ps}L(1 - \varepsilon_f)$. We define loading direction to have the positive strain value which give $\varepsilon_f \geq 0$ s. While ε_s is negative when substrate is under tension. The two strain measurements have the following relationship:

$$(1 - \varepsilon_f)\lambda_{ps} = 1 - \varepsilon_s \quad (5.1)$$

Consistent to what we have observed in the experiment, no ridge or high amplitude aspect ratio wrinkle has been found on the surface during releasing. Instead, uniform wrinkles are developed with higher frequency 2nd generation wrinkles formed at the valleys (shown in Fig. 5.5b1 and Fig. 5.5b2 at film strain of $\varepsilon_f = 0.16$). Recall the necessary conditions for ridging in Chapter 4, for a specific substrate pre-stretch ratio, there exists a critical stiffness ratio, beyond which ridge can be triggered. For the oxidize PDMS system with large initial pre-stretch, although a very stiff top layer is likely to active ridging transition, it doesn't contribute to large stiffness ratio as it does in a bi-layer system. The graded modulus PDMS can be not rigorously divided into a number of separated bi-layer systems along the PDMS thickness direction. Even if μ_{l1}/μ_s is large enough to initiate ridging in bi-layer system, the effective stiffness ratio for each sub bi-layer is much smaller and it is much harder to trigger ridging. Generally, by intentionally designing the modulus grading, ridge can be

suppressed effectively. Moreover, for soft systems with smoothly decaying modulus, it is not likely to have ridge no matter how large the strain mismatch is.

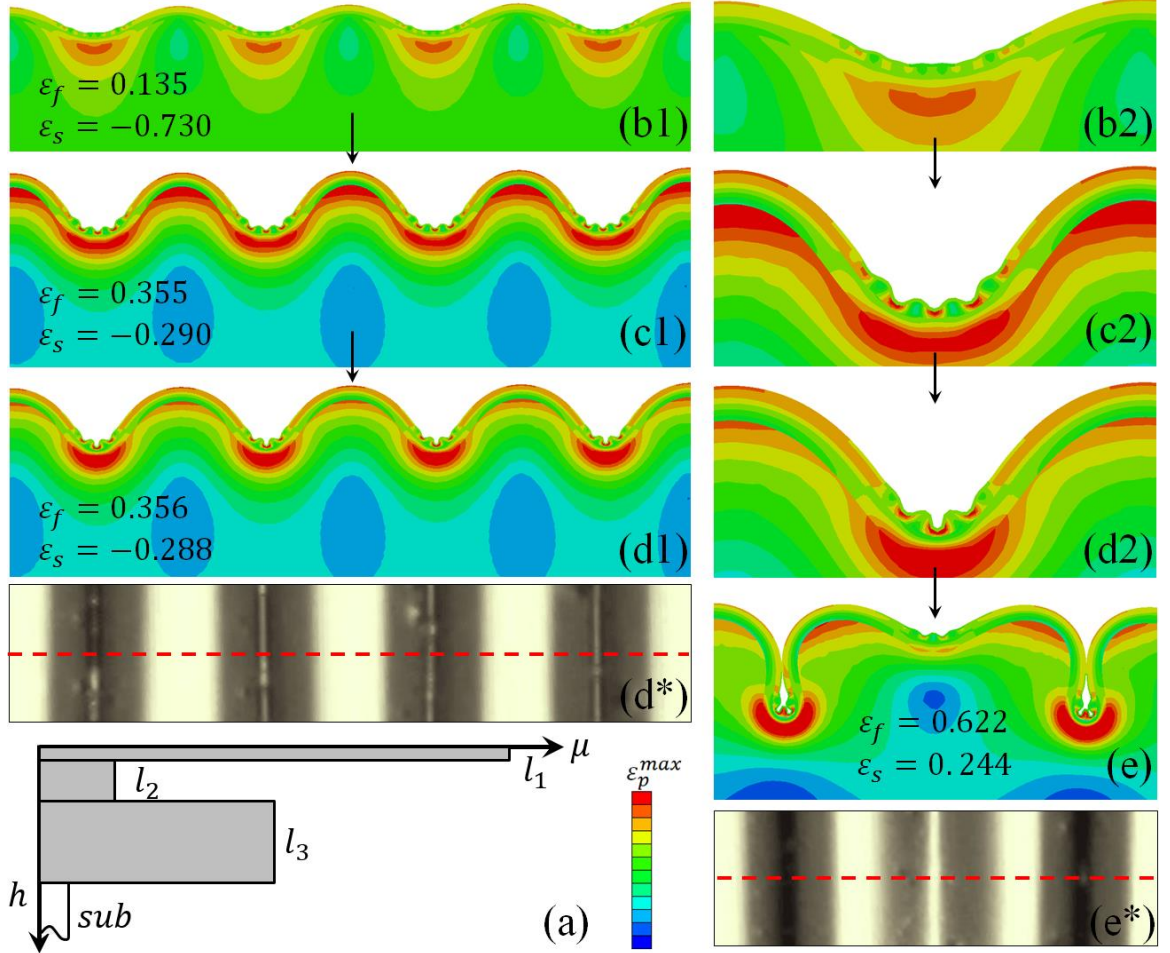
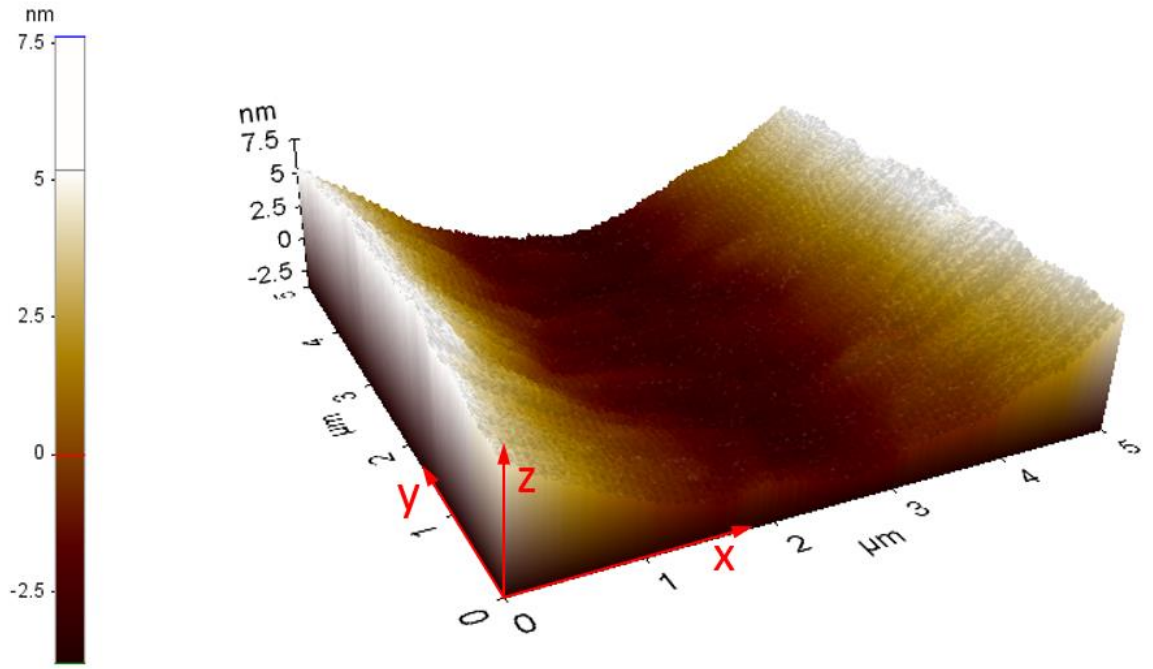


Figure 5.5. Multi-layer structure simulation to mimic oxidized PDMS at substrate pre-stretch ratio $\lambda_{ps} = 2.0$. (a) the schematics of modulus and thickness distribution of the finite element model; (b1) Ruga state at strain of $\epsilon_f = 0.135$, $\epsilon_s = -0.730$; (b2) is the zoomed in figure of the valleys in (b1); (c1) Ruga state at strain of $\epsilon_f = 0.355$, $\epsilon_s = -0.290$; (c2) is the zoomed in figure of the valleys in (c1); (d1) Ruga state at strain of $\epsilon_f = 0.356$, $\epsilon_s = -0.288$; (d2) is the zoomed in figure of the valleys in (d1); (d*) the

experimental verification of (d1); (e) folded ruga during further compression $\varepsilon_f = 0.622$, $\varepsilon_s = 0.244$; (e*) the experimental verification of (e).

In the exaggerated valley picture (b2), eight small shallow wave can be seen at current strain level. With increasing loading strain $\varepsilon_f = 0.355$ shown in (c1), wrinkle amplitude grows and the 2nd generation wrinkles nucleate at large wrinkle valleys. (c2) shows four higher frequency wrinkles are generated at the valley. At this strain level, 2nd generation wrinkles nucleate very fast at current local compressive strain and this nucleation leads to large curvature at the 1st generation wrinkle valley. In the meantime, the curvature of the peak of 1st generation wrinkles decrease and the multi-layer structure loses its global sinusoidal wrinkling shape (shown in (d1) at strain of $\varepsilon_f = 0.356$). The exaggerated wrinkle valley (d2) reveals two significantly growing wrinkles and two shallow ones on the sides. From the top view (d*) of optical measured PDMS sample, we can match it with simulation result (d1). While the higher frequency wrinkles cannot be observed by regular optics. Under further compressive load, the global wrinkle period multiplication will take place and eventually multi-scale fold is generated, as shown in (e) at strain of $\varepsilon_f = 0.622$. Due to the surface compression inhomogeneity, some region has larger compressive strain as we have discussed previously. The high compression zones are more likely to trigger period multiplications. The experimental result in (e*) is captured from the zoomed in optical measurement in Fig. 5.2c, showing that at these high compressive strain regions, doubling can indeed happen locally. While the less compression zones remain normal single period deformation. The coexistence of single mode (SM1) and double mode (DM1) is a reflection of compressive strain inhomogeneity.

To see the hierarchical wrinkles with possible generations experimentally, AFM is used to detect much smaller waves. The specimen is tested after it is fully released from the stretched configuration. We apply contact mode and scan a square region with size of $5\mu\text{m} \times 5\mu\text{m}$ at scan rate 0.2 Hz. The scanned surface is shown in Fig. 5.6a, the loading direction is along the x axis and the curved surface is the oxidized PDMS surface.



(a)

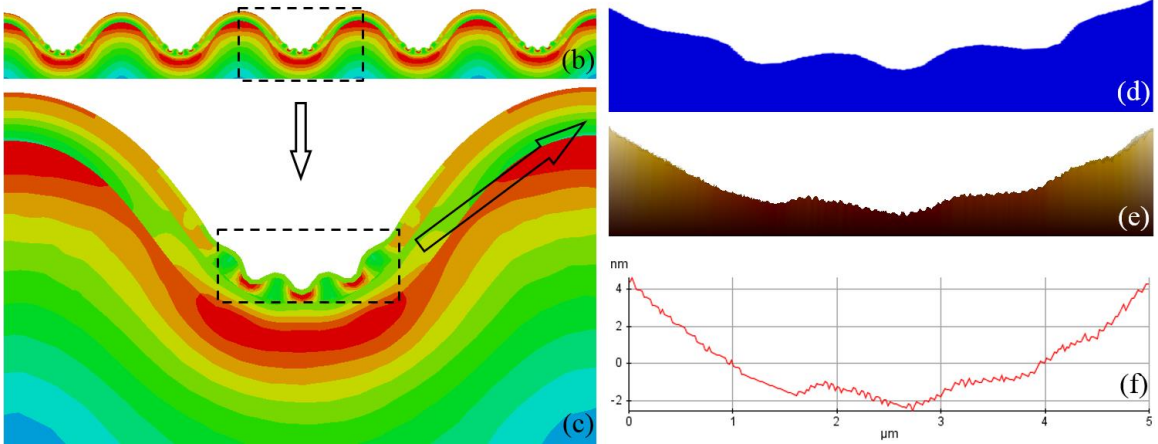


Figure 5.6. AFM measurement of hierarchical wrinkles on oxidized PDMS surface and its comparison with FEM results. (a) scanned region of PDMS surface ($5\mu\text{m} \times 5\mu\text{m}$); (b) FEM result of a pre-stretched ($\lambda_{ps} = 2.0$) multi-layer film system with kinked modulus distribution; (c) exaggerated view of the large wrinkle valley from the dotted box in (b); (d, e) comparison of simulation with AFM measurement: (d) shows the exaggerated view from the dotted box in (c) subject to certain shrinkage amount to fit with (e); (f) the corresponding amplitude data of measurement in (e).

In Fig. 5.6a, it clearly indicates two major wave generations and one very high frequency wave generation on the cross section face $y = 0$. By inspection of the larger wrinkle valley shown in (a), the higher frequency wrinkles which has the average wavelength $l = 1\mu\text{m}$ is observed with high amplitude aspect ratio at the bottom due to the higher compressive strain presented at the large curvature region. Away from the bottom, the wrinkle amplitude becomes smaller. Our FEM result shown in Fig. 5.6 has high consistency with the AFM observation. Fig. 5.6c is the exaggerated view of a global wrinkle valley from (b). If we further zoom in the second generation wrinkles as illustrated in Fig. 5.6d, it is comparable with the cross section of AFM measurement in Fig. 5.6e. Its corresponding length scale is shown in Fig. 5.6f. The formation of this hierarchical surface wrinkle is due to the distinctive modulus distribution of the oxidized PDMS. The soft middle layer plays an important role in determining the distribution of hierarchical wrinkle generations. According to our simulation on multi-layer (three film layer and soft substrate) structure with gradually decayed modulus distribution $\mu_{l1} > \mu_{l2} > \mu_{l3}$, no hierarchical wrinkles were observed. Instead, surface goes through single mode wrinkle to double mode

transition, which is followed by mode switching even without viscosity. Along y direction, the wrinkle like shape on the cross section $x = 5\mu\text{m}$ is scanning error due to the fluctuation of the atom form microscope. The cantilever tip scans the sample along the x direction and sweep over y direction. During data collecting, a little ambient perturbation will cause the discrepancy along y direction but it won't affect the results along x direction.

5.4. Summary of ruga morphologies control aspects and factors

As discussed in previous sections and chapters, the surface morphology can be controlled from various aspects by tuning the configuration of its affiliated soft system. Herein, we list the possible combinations in table 5.1 according to our studies.

Table 5.1. Ruga morphological control aspects and factors

Control aspects	Control factor
Ruga phase	Stiffness ratio
Ruga period	Stiffness ratio, pre-stretch ratio
Aspect ratio of ruga	Pre-stretch ratio
Ruga phase hierarchical distribution	Multi-layer structure
Critical ruga phases triggering strain	Stiffness ratio, Boundary condition
Suppression of certain transitions	Graded or multi-layer structure
Ruga mode switching	Loading history, viscosity

An example of ruga phase and period control is demonstrated both experimentally and numerically in Chapter 4 Fig. 4.2. Adjusting the bi-layer stiffness ratio determines what

kind of ruga phase we can get out of the soft material system. For instance, surface creasing happens when the normalized characteristic wavenumber $\bar{k} \geq 0.41$, identical to modulus ratio $R < 45$ [13]. When $\bar{k} < 0.41$, instead of having creasing ruga phase, double mode or quadruple mode wrinkle phases will be observed with sufficient loading strain. Substrate pre-stretch amount controls the period of ruga phases by forming higher aspect ratio ruga features. It is worthy mention that for a bi-layer system with specific stiffness ratio, period controlling is only valid outside the disorder transition zone in Fig. 4.4. Larger strain mismatch leads to smaller ruga period, which means more regional localizations. This then results in global delocalization, since large number of regional localizations makes the surface difficult to nucleate energy to one single point. Under this circumstance, uniformly distributed patterns with high symmetry level can be maintained even the system is subject to large loading strain. Another aspect of ruga distribution is the hierarchical wrinkles controlled by well-designed multi-layer structure. It allows the surface not to have very large global deformation even at very large loading strain. In the meantime, it preserves surface area by forming higher frequency rugae on the global ruga features. According to Chapter 2, the critical triggering strains for various surface ruga instabilities are closely related to the stiffness ratio and distribution of the soft material system [13]. Boundary conditions such as specimen size, also affects the onset strain for ruga phase transitions. The ruga irreversibility study in Chapter 3 provides an efficient way to reach excited ruga modes by inducing sufficient viscosity to the soft material system. The excited modes have even number times of the based mode wavelength and the surface ruga configuration is highly loading history dependent. Based on our simulation and experimental results, general ridging transition can be suppressed by assigning multi-layer or graded modulus

structure to the system, even the system is configured with very large strain mismatch. In our simulation, we presented how ridging is suppressed in neo-Hookean multilayer material, which experiences hyperelastic material behavior. Based on our unrepresented simulation, certain rubber like material that represented by Ogden model can also suppress ridge formation. Other possible suppressive factors such as plastic deformation and viscoelastic material behavior may reflect to different surface ruga evolution which will be accompanied with ridging suppression during loading. The details of these transitions require further investigation.

5.5. Conclusion

In this chapter, we pointed out the importance of investigating the aspects of ruga morphologies control. As an example, various microscopes with different resolution levels are used to detect the ruga features of an oxidized PDMS surface with strain mismatch. Regular optics shows stripes with highly localized valleys along the surface and groups of wrinkles are observed lining up to herringbone shape due to the 2D small strain deformation. Unlike stiff film bi-layer system, the AFM measured results shows that the oxidized PDMS is a multi-layer film/ substrate structure with kinked modulus distribution. A very soft film layer is sitting in between the top stiffest and the second stiffest layers. This specific property suppresses ridging, even the specimen is experiencing very large substrate pre-stretch. Hierarchical wrinkles with higher frequency generations are observed by AFM and verified by our simulation results. The soft middle layer, which results in the kinked PDMS modulus distribution, is the key factor that brings hierarchy deformation to the system. Our simulations show that the multi-layer structure with gradually decayed

modulus distribution cannot elicit hierarchical wrinkles. Finally, we sort out the ruga morphologies control aspects and discuss their control factors systematically.

Chapter 6

Conclusions and Perspectives

6.1. Overall conclusions

Various ruga phase evolutions together with their distinct properties are investigated using finite element method. Experiments verified a lot of phenomena that we observed in simulations.

In Chapter 2, we constructed a ruga phase diagram for primary bilayer (PB) system under pure compressive lateral loading. Regarding to the characteristic wavenumber of the PB system in the phase diagram, eight ruga phases are sorted, which are: wrinkle, wrinkle-setback crease, instantaneous crease, double-mode wrinkle, quadruple-mode wrinkle, quadruple-mode crease, quadruple-mode fold, quadruple-mode folded crease. We delineate the boundaries of the transitions between theses ruga phases in the phase diagram. Film creasing is found to localize at the substrate strain of 0.35, where the global crease of substrate takes place. Folding is regarded as a delocalization process which prevent further periodic multiplications. With very large compressive strain, folds can also localize with the substrate global localization.

In Chapter 3, we investigated the ruga irreversibility which includes ‘localization irreversibility’ and ‘modal irreversibility’. The localization irreversibility zones are marked in the phase diagram we construct in previous chapter showing the boundary of possible irreversibility types.

In Chapter 4, the ruga phase evolution and order-disorder transitions with substrate pre-stretch are studied. Ruga period can be controlled by adjusting the substrate pre-stretch ratio. Compared to crease at every four wrinkle valley and fold at every four wrinkle valley for pure compression PB system, every valley crease, every other valley crease and very other valley fold can be observed with PB system under strain mismatch. With sufficient substrate pre-stretch, ridge can occur when the PB system's characteristic wavenumber is large enough. Order-disorder transition is a consequence of ruga mobility bifurcation and it leads to co-existence of ruga phases in the PB system.

In Chapter 5, ruga patterning on oxidized pre-stretched PDMS is discussed. We use general optics, interferometry microscope (Zygo) and atom force microscope (AFM) to study the ruga patterns at different scales. Recent study revealed that oxidized rubbery materials develop multilayered structures. The mismatch in the stiffness between the adjacent layers, especially the soft middle layer, results in hierarchical wrinkles that span several orders of magnitude. It turns out that multi-layer structure suppresses ridging even if the system has very large substrate pre-stretch. This is contradictory to PB system under large strain mismatch. We verify the experimental results by modeling a three-layer/substrate system, and it indeed shows no ridging process during loading. Furthermore, higher frequency wrinkle generations are observed at the dominating frequency wrinkle valleys in both experiment and finite element model. Only kinked modulus distribution can trigger multi-frequency wrinkles, in other words, gradually decayed modulus distribution system has its single characteristic wavelength and it may go through mode switching to excited modes during loading.

6.2. Outlook of future research

In this thesis, we investigated the soft material system by focusing systematic study of bilayer system surface under external loading. Throughout our research work, we have presented various soft material systems such as homogeneous half space, thin film system, multi-layer system and graded modulus system. Although we have covered many aspects in soft matter study, there are still limitations of our work. For example, the irreversibility of ruga phases under viscosity effect needs more study quantitatively. The order-disorder transition in 2D system triggered by different loading method such as sequentially loading from different directions and dynamic loadings requires more consideration. Experimentally, the uncertainty of ruga phase evolution caused by defects on the surface or within the material needs further investigation.

Finally, we expect ruga pattern formation through elastic instability to offer a non-lithographic approach to construct surfaces with well-designed patterns at different scales. In addition, understanding mechanics behind ruga formation will uncover important phenomena in nature and science. To follow up to what we have investigated and uncovered in the previous chapters, here is a list of potential aspects and topics for future work.

1. Hierarchical ruga of multilayered materials is expected to have many applications such as adhesion control, wetting control with super hydrophobic/hydrophilic surfaces including anti-biofouling. More systematic study of post-buckling evolution of the multi-scale wrinkles and the interaction among them is needed. Regarding to different hierarchical ruga morphologies, it is essential to have a guide of multi-layer structure modulus design for surface pattern control.

2. There has been some progress in studying growth induced ruga in biological organs. For example, researchers have been investigating the role of ruga mechanics in the formation of brain sulci and the potential relation between irreversibility of ruga patterns and Traumatic Brain Injury (TBI). As illustrated in Fig. 1.1(e-i), bio-structures usually exhibit multilayer configuration with fiber-reinforced anisotropy. Understanding of bio-systems requires precise studies of each system with distinct physical properties. There still exists many issues on accurately detect the strain mismatch variations in anisotropic inhomogeneous soft structures during growth induced deformations.
3. On the application side, experimental frequency control of ruga structures over an appreciable area is still a great challenge. Also, new experimental techniques are still needed to use ruga for characterization of material properties under different environments. From experimental aspect, ruga mechanics under viscoelasticity, dynamic loading, combined with anisotropic and multi-material structure is still waiting to be explored.
4. Much of recent progress in ruga mechanics research was possible thanks to advancement of computational mechanics, in particular, finite element method and hybrid computational techniques for multi-scale analysis. However, more efforts are still needed to develop reliable numerical methods capable of dealing with 2D or 3D ruga calculations which require large element number and calculate time, of detecting bifurcation of equilibrium configuration of potential with multiple quasi-convexities, of simulating dynamics ruga formation and its motion.

Bibliography

- [1] M. A. Biot, 1965 Mechanics of incremental deformation. New York, NY.
- [2] A. N. Gent, I.S. Cho, Surface Instabilities in Compressed or Bent Rubber Blocks. *Rubber Chemistry and Technology* **72**, 253-262 (1999).
- [3] F. Brau, H. Vandeparre, A. Sabbah, C. Poulard, A. Boudaoud, Damman, P. Multiplelength-scale elastic instability mimics parametric resonance of nonlinear oscillators. *Nature Physics* **7**, 56-60 (2010).
- [4] M. Diab, J. Torres, M. Monn, K.-S. Kim Hidden, Forbidden and inherited wrinkles on a soft material surface (2016). to be submitted.
- [5] L. Pocivavsek, R. Dellsy, A. Kern, S. Johnson, B. H. Lin, K.Y.C. Lee, E. Cerda, Stress and fold localization in thin elastic membranes. *Science* **320**, 912-916 (2008).
- [6] J. Y. Sun, S. Xia, M. W. Moon, K.H. Oh, K.S. Kim, Folding wrinkles of a thin stiff layer on a soft substrate. *Proceedings of the Royal Society A: Mathematical, Physical and Engineering Sciences* **468**, 932-953 (2011).
- [7] Y. Cao, J.W. Hutchinson, Wrinkling phenomena in neo-Hookean film/substrate bilayers. *Journal of Applied Mechanics* **79**, 031019 (2012).
- [8] N. Bowden, S. Brittain, A.G. Evans, J.W. Hutchinson, Whitesides, G.M. Spontaneous formation of ordered structures in thin films of metals supported on an elastomeric polymer. *Nature* **393**, 146-149 (1998).
- [9] K. Efimenko, M. Rackaitis, E. Manias, A. Vaziri, L. Mahadevan, J. Genzer, Nested selfsimilar wrinkling patterns in skins. *Nature materials* **4**, 293-297 (2005).
- [10] Faruque S. Ahmed, S. Nagashima, J.Y. Lee, K.-R. Lee, K.-S Kim, M.-W. Moon, Self-assembled folding of a biaxially compressed film on a compliant substrate. *Carbon* **76**, 105-112 (2014).
- [11] M. Diab, T. Zhang, R. Zhao, H. Gao, K. S. Kim, Ruga mechanics of creasing: from instantaneous to setback creases. *Proceedings of the Royal Society A: Mathematical, Physical and Engineering Sciences* **469**, 20120753-20120753 (2013).
- [12] M. Diab, K.S. Kim, Ruga-formation instabilities of a graded stiffness boundary layer in a neo-Hookean solid. *Proceedings of the Royal Society A: Mathematical, Physical and Engineering Sciences* **470**, 20140218-20140218 (2014).
- [13] R. Zhao, T. Zhang., H. Gao, K. S. Kim. The primary bilayer ruga-phase diagram I: Localizations in ruga evolution. *Extreme Mechanics Letters* **4**, 76-82 (2015).
- [14] Z. Jia, C. Peng, J. Lou, T. Li, A map of competing buckling-driven failure modes of substrate-supported thin brittle films. *Thin Solid Films* **520**, 6576-6580 (2012).
- [15] T. Zhang, X. Li, H. Gao, Defects controlled wrinkling and topological design in graphene. *Journal of the Mechanics and Physics of Solids* **67**, 2-13 (2014).
- [16] Z. Zhang, T. Li, Determining graphene adhesion via substrate-regulated morphology of graphene. *Journal of Applied Physics* **110**, 083526 (2011).
- [17] S. Zhu, T. Li, Hydrogenation-assisted graphene origami and its application in programmable molecular mass uptake, storage, and release. *ACS nano* **8**, 2864-2872 (2014).

- [18] S. Zhu, T. Li, Wrinkling Instability of Graphene on Substrate-Supported Nanoparticles. *Journal of Applied Mechanics* **81**, 061008 (2014).
- [19] J. Y. Chung, J. P. Youngblood, C.M. Stafford, Anisotropic wetting on tunable microwrinkled surfaces. *Soft Matter* **3**, 1163-1169 (2007).
- [20] E. P. Chan, E. J. Smith, R. C. Hayward, A. J. Crosby, Surface Wrinkles for Smart Adhesion. *Advanced materials* **20**, 711-716 (2008).
- [21] D. H. Kim, J. H. Ahn, W. M. Choi, H. S. Kim, T. H. Kim, J. Song, Y. Y. Huang, Z. Liu, C. Lu, J.A. Rogers, Stretchable and foldable silicon integrated circuits. *Science* **320**, 507-511 (2008).
- [22] H. C. Ko, M. P. Stoykovich, J. Song, V. Malyarchuk, W. M. Choi, C. J. Yu, J.B. Geddes, J. Xiao, S. Wang, Y. Huang, et al. A hemispherical electronic eye camera based on compressible silicon optoelectronics. *Nature* **454**, 748-753 (2008).
- [23] P.-C. Lin, S. Vajpayee, A. Jagota, C.-Y. Hui, S. Yang, Mechanically tunable dry adhesive from wrinkled elastomers. *Soft Matter* **4**, 1830 (2008).
- [24] K. Khare, J. Zhou, S. Yang, Tunable open-channel microfluidics on soft poly(dimethylsiloxane) (PDMS) substrates with sinusoidal grooves. *Langmuir* **25**, 12794-12799 (2009).
- [25] Y. Rahmawan, M. W. Moon, K.S. Kim, K. R. Lee, K. Y. Suh, Wrinkled, dual-scale structures of diamond-like carbon (DLC) for superhydrophobicity. *Langmuir* **26**, 484-491 (2010).
- [26] J. A. Rogers, T. Someya, Y. Huang, Materials and mechanics for stretchable electronics. *Science* **327**, 1603-1607 (2010).
- [27] A. Chen, D. K. Lieu, L. Freschauf, V. Lew, H. Sharma, J. Wang, D. Nguyen, I. Karakikes, R. J. Hajjar, A. Gopinathan, et al. Shrink-film configurable multiscale wrinkles for functional alignment of human embryonic stem cells and their cardiac derivatives. *Advanced materials* **23**, 5785- 5791 (2011).
- [28] J. B. Kim, P. Kim, N.C. Pégard, S.J. Oh, C.R. Kagan, J.W. Fleischer, H.A. Stone, Y.-L. Loo, Wrinkles and deep folds as photonic structures in photovoltaics. *Nature Photonics* **6**, 327-332 (2012).
- [29] T. Zhang, Z. Zhang, K. S. Kim, H. Gao, An accordion model integrating self-cleaning, strong attachment and easy detachment functionalities of gecko adhesion. *Journal of Adhesion Science and Technology* **28**, 226-239 (2012).
- [30] Z. Zhang, T. Zhang, Y.W. Zhang, K. S. Kim, H. Gao, Strain-controlled switching of hierarchically wrinkled surfaces between superhydrophobicity and superhydrophilicity. *Langmuir* **28**, 2753-2760 (2012).
- [31] R. Li, H. Yi, X. Hu, L. Chen, G. Shi, W. Wang, T. Yang, Generation of diffraction-free optical beams using wrinkled membranes. *Scientific reports* **3** (2013).
- [32] C. Cao, H. F. Chan, J. Zang, K. W. Leong, X. Zhao, Harnessing localized ridges for highaspect-ratio hierarchical patterns with dynamic tunability and multifunctionality. *Advanced materials* **26**, 1763-1770 (2014).
- [33] D. Terwagne, M. Brojan, P. M. Reis, Smart morphable surfaces for aerodynamic drag control. *Advanced materials* **26**, 6608-6611 (2014).
- [34] P. Wang, F. Casadei, S. Shan, J.C. Weaver, K. Bertoldi, Harnessing Buckling to Design Tunable Locally Resonant Acoustic Metamaterials. *Physical review letters* **113** (2014).

- [35] D. K. Cullen, K. D. Browne, Y. Xu, S. Adeeb, J. A. Wolf, R. M. McCarron, S. Yang, M. Chavko, D.H. Smith, Blast-induced color change in photonic crystals corresponds with brain pathology. *Journal of neurotrauma* **28**, 2307-2318 (2011).
- [36] S. Budday, C. Raybaud, E. Kuhl, A mechanical model predicts morphological abnormalities in the developing human brain. *Scientific reports* **4**, 5644 (2014).
- [37] T. Tallinen, J.Y. Chung, J.S. Biggins, L. Mahadevan, Gyrification from constrained cortical expansion. *Proceedings of the National Academy of Sciences of the United States of America* **111**, 12667-12672 (2014).
- [38] J. Dervaux, Y. Couder, M.-A. Guedeau-Boudeville, M. Ben Amar, Shape Transition in Artificial Tumors: From Smooth Buckles to Singular Creases. *Physical review letters* **107** (2011).
- [39] B. Li, Y.-P. Cao, X.-Q Feng, H. Gao, Mechanics of morphological instabilities and surface wrinkling in soft materials: a review. *Soft Matter* **8**, 5728 (2012).
- [40] S. Pruss, M. Fraiser, D.J. Bottjer, Proliferation of Early Triassic wrinkle structures: Implications for environmental stress following the end-Permian mass extinction. *Geology* **32**, 461 (2004).
- [41] H. Porada, E.H. Bouougri, Wrinkle structures—a critical review. *Earth-Science Reviews* **81**, 199-215 (2007).
- [42] K. Li, D. Ge, S. Cai, Gravity-induced wrinkling of thin films on soft substrates. *EPL (Europhysics Letters)* **100**, 54004 (2012).
- [43] G. Mariotti, S. B. Pruss, J. T. Perron, T. Bosak, Microbial shaping of sedimentary wrinkle structures. *Nature Geoscience* **7**, 736-740 (2014).
- [44] M. A. Biot, Instability of a continuously inhomogeneous viscoelastic half-space under initial stress. *Journal of the Franklin Institute* **270**, 190-201 (1960).
- [45] M. A. Biot, Surface instability of rubber in compression. *Applied Scientific Research* **12**, 168– 182 (1963).
- [46] J. L. Nowinski, On the Surface Instability of an Isotropic Highly Elastic Half-space, Department of Mechanical and Aerospace Engineering, University of Delaware (1968).
- [47] H. G. Allen, Analysis and design of structural sandwich panels. New York, NY, Pergamon press (1969).
- [48] T. W. Shield, K.S. Kim, R. T. Shield, The Buckling of an Elastic Layer Bonded to an Elastic Substrate in Plane Strain. *Journal of Applied Mechanics* **61**, 231 (1994).
- [49] D. J. Steigmann, R.W. Ogden, Plane deformations of elastic solids with intrinsic boundary elasticity. *Proceedings of the Royal Society A: Mathematical, Physical and Engineering Sciences* **453**, 853-877 (1997).
- [50] E. Cerda, L. Mahadevan, Conical surfaces and crescent singularities in crumpled sheets. *Physical review letters* **80**, 2358-2361 (1998).
- [51] R. Huang, Z. Suo, Wrinkling of a compressed elastic film on a viscous layer. *Journal of Applied Physics* **91**, 1135 (2002).
- [52] R. Huang, Z. Suo, Instability of a compressed elastic film on a viscous layer. *International Journal of Solids and Structures* **39**, 1791-1802 (2002).
- [53] E. Cerda, L. Mahadevan, Geometry and physics of wrinkling. *Physical review letters* **90**, 074302 (2003).
- [54] R. Huang, Kinetic wrinkling of an elastic film on a viscoelastic substrate. *Journal of the Mechanics and Physics of Solids* **53**, 63-89 (2005).

- [55] Z. Y. Huang, W. Hong, Z. Suo, Nonlinear analyses of wrinkles in a film bonded to a compliant substrate. *Journal of the Mechanics and Physics of Solids* **53**, 2101-2118 (2005).
- [56] J. Huang, M. Juskiewicz, W. H. de Jeu, E. Cerda, T. Emrick, N. Menon, T.P. Russell, Capillary wrinkling of floating thin polymer films. *Science* **317**, 650-653 (2007).
- [57] D. Lee, N. Triantafyllidis, J. R. Barber, M. D. Thouless, Surface instability of an elastic half space with material properties varying with depth. *Journal of the Mechanics and Physics of Solids* **56**, 858-868 (2008).
- [58] J. Song, H. Jiang, Z. J. Liu, D.Y. Khang, Y. Huang, J. A. Rogers, C. Lu, C. G. Koh, Buckling of a stiff thin film on a compliant substrate in large deformation. *International Journal of Solids and Structures* **45**, 3107-3121 (2008).
- [59] E. K. Hobbie, D. O. Simien, J. A. Fagan, J. Y. Huh, J. Y. Chung, S. D. Hudson, J. Obrzut, J. F. Douglas, C. M. Stafford, Wrinkling and Strain Softening in Single-Wall Carbon Nanotube Membranes. *Physical review letters* **104**, 125505 (2010).
- [60] J. Yin, X. Chen, Elastic buckling of gradient thin films on compliant substrates. *Philosophical Magazine Letters* **90**, 423-433 (2010).
- [61] C. S. Davis, A. J. Crosby, Mechanics of wrinkled surface adhesion. *Soft Matter* **7**, 5373 (2011).
- [62] H. King, R. D. Schroll, B. Davidovitch, N. Menon, Elastic sheet on a liquid drop reveals wrinkling and crumpling as distinct symmetry-breaking instabilities. *Proceedings of the National Academy of Sciences of the United States of America* **109**, 9716-9720 (2012).
- [63] Y.-C. Chen, A. J. Crosby, Wrinkling of inhomogeneously strained thin polymer films. *Soft Matter* **9**, 43 (2013).
- [64] M. R. Semler, J. M. Harris, E. K. Hobbie, Wrinkling and folding of nanotube-polymer bilayers. *The Journal of chemical physics* **141**, 044901 (2014).
- [65] W. T. Koiter, On the stability of elastic equilibrium (in Dutch with English summary). Techn. Univ. of Delft (1945).
- [66] J. W. Hutchinson, W. T. Koiter, Post-buckling theory. *Applied Mechanics Reviews* **23**, 1353- 1366 (1970).
- [67] B. Budiansky, Theory of Buckling and Post-Buckling Behavior of Elastic Structures. *Advances in Applied Mechanics* **14**, 1-65 (1974).
- [68] J. W. Hutchinson, The role of nonlinear substrate elasticity in the wrinkling of thin films. *Philosophical transactions. Series A, Mathematical, physical, and engineering sciences* **371**, 20120422 (2013).
- [69] Y. Cao, J. W. Hutchinson, From wrinkles to creases in elastomers: the instability and imperfection-sensitivity of wrinkling. *Proceedings of the Royal Society A: Mathematical, Physical and Engineering Sciences* **468**, 94-115 (2011).
- [70] C. M. Stafford, C. Harrison, K. L. Beers, A. Karim, E. J. Amis, M. R. VanLandingham, H.C. Kim, W. Volksen, R.D. Miller, E.E. Simonyi, A buckling-based metrology for measuring the elastic moduli of polymeric thin films. *Nature materials* **3**, 545-550 (2004).
- [71] H. J. Choi, J. H. Kim, H. J. Lee, S. A. Song, H. J. Lee, J. H. Han, M. W. Moon, WrinkleBased Measurement of Elastic Modulus of Nano-Scale Thin Pt Film

- Deposited on Polymeric Substrate: Verification and Uncertainty Analysis. *Experimental Mechanics* **50**, 635-641 (2009).
- [72] E. B. Hohlfeld, Creasing, post-bifurcations, and the spontaneous breakdown of scaleinvariance, Harvard University (2008).
 - [73] W. Hong, X. Zhao, Z. Suo, Formation of creases on the surfaces of elastomers and gels. *Applied Physics Letters* **95**, 111901 (2009).
 - [74] E. Hohlfeld, L. Mahadevan, Unfolding the Sulcus. *Phys Rev Lett* **106** (2011).
 - [75] E. Hohlfeld, L. Mahadevan, Scale and Nature of Sulcification Patterns. *Physical review letters* **109**, 025701 (2012).
 - [76] E. Hohlfeld, Coexistence of Scale-Invariant States in Incompressible Elastomers. *Physical review letters* **111** (2013).
 - [77] W.-K. Seong, J.-Y.L., K.-R. Lee, J. Bae, J.-H. Jung, M. Diab, M.-W. Moon, K.-S. Kim, J. Ihm 2014 Conformational evolution of compressed graphene on Soft Substrates. To be submitted.
 - [78] J. F. Zang, X. H. Zhao, Y. P. Cao, J. W. Hutchinson, Localized ridge wrinkling of stiff films on compliant substrates. *J Mech Phys Solids* **60**, 1265-1279 (2012).
 - [79] A. Takei, L. Jin, J. W. Hutchinson, H. Fujita, Ridge localizations and networks in thin films compressed by the incremental release of a large equi-biaxial pre-stretch in the substrate. *Advanced materials* **26**, 4061-4067 (2014).
 - [80] M. W. Moon, H. M. Jensen, J. W. Hutchinson, K. H. Oh, A.G. Evans, The characterization of telephone cord buckling of compressed thin films on substrates. *Journal of the Mechanics and Physics of Solids* **50**, 2355-2377 (2002).
 - [81] L. B. Freund, S. S. Thin Film Materials: Stress, Defect Formation and Surface Evolution, Cambridge University Press (2003).
 - [82] M. W. Moon, K. R. Lee, K. H. Oh, J. W. Hutchinson, Buckle delamination on patterned substrates. *Acta Materialia* **52**, 3151-3159 (2004).
 - [83] H. Mei, R. Huang, J.Y. Chung, C.M. Stafford, H.-H. Yu, Buckling modes of elastic thin films on elastic substrates. *Applied Physics Letters* **90**, 151902 (2007).
 - [84] J. Zang, S. Ryu, N. Pugno, Q. Wang, Q. Tu, M.J. Buehler, X. Zhao, Multifunctionality and control of the crumpling and unfolding of large-area graphene. *Nature materials* **12**, 321-325 (2013).
 - [85] Q. M. Wang, X. H. Zhao, 2014 Phase Diagrams of Instabilities in Compressed Film-Substrate Systems. *Journal of Applied Mechanics* **81**, 051004 (2008).
 - [86] K. Zhang, M. Arroyo, Understanding and strain-engineering wrinkle networks in supported graphene through simulations. *Journal of the Mechanics and Physics of Solids* **72**, 61-74 (2014).
 - [87] T. Tanaka, S.-T. Sun, Y. Hirokawa, S. Katayama, J. Kucera, Y. Hirose, T. Amiya, Mechanical instability of gels at the phase transition. *Nature* **325**, 796-798 (1987).
 - [88] W. T. S. Huck, N. Bowden, P. Onck, T. Pardoen, J. W. Hutchinson, G. M. Whitesides, Ordering of Spontaneously Formed Buckles on Planar Surfaces. *Langmuir* **16**, 3497-3501 (2000).
 - [89] P.-C. Lin, S. Yang, Spontaneous formation of one-dimensional ripples in transit to highly ordered two-dimensional herringbone structures through sequential and unequal biaxial mechanical stretching. *Applied Physics Letters* **90**, 241903 (2007).
 - [90] V. Trujillo, J. Kim, R. C. Hayward, Creasing instability of surface-attached hydrogels. *Soft Matter* **4**, 564 (2008).

- [91] D. Breid, A. J. Crosby, Surface wrinkling behavior of finite circular plates. *Soft Matter* **5**, 425 (2009).
- [92] J. Yoon, J. Kim, R. C. Hayward, Nucleation, growth, and hysteresis of surface creases on swelled polymer gels. *Soft Matter* **6**, 5807 (2010).
- [93] P. Kim, M. Abkarian, H. A. Stone, Hierarchical folding of elastic membranes under biaxial compressive stress. *Nature materials* **10**, 952-957 (2011).
- [94] J. L. Nowinski, Surface Instability of a Half-space under High Two-dimensional Compression. *Journal of the Franklin Institute* **288**, 367-376 (1969).
- [95] S. A. Usmani, M. F. Beatty, On the surface instability of a highly elastic half-space. *Journal of Elasticity* **4**, 249-263 (1974).
- [96] X. Chen, J. W. Hutchinson, Herringbone buckling patterns of compressed thin films on compliant substrates. *Journal of Applied Mechanics* **71**, 597-603 (2004).
- [97] X. Chen, J. W. Hutchinson, A family of herringbone patterns in thin films. *Scripta Materialia* **50**, 797-801 (2004).
- [98] L. Mahadevan, S. Rica, 2005 Self-organized origami. *Science* **307**, 1740 (2008).
- [99] B. Audoly, A. Boudaoud, Buckling of a stiff film bound to a compliant substrate - Part I: Formulation, linear stability of cylindrical patterns, secondary bifurcations. *Journal of the Mechanics and Physics of Solids* **56**, 2401-2421 (2008).
- [100] B. Audoly, A. Boudaoud, Buckling of a stiff film bound to a compliant substrate - Part II: A global scenario for the formation of herringbone pattern. *Journal of the Mechanics and Physics of Solids* **56**, 2422-2443 (2008).
- [101] B. Audoly, A. Boudaoud, Buckling of a stiff film bound to a compliant substrate - Part III: Herringbone solutions at large buckling parameter. *Journal of the Mechanics and Physics of Solids* **56**, 2444-2458 (2008).
- [102] J. Song, H. Jiang, W.M. Choi, D. Y. Khang, Y. Huang, J. A. Rogers, An analytical study of two-dimensional buckling of thin films on compliant substrates. *Journal of Applied Physics* **103**, 014303 (2008).
- [103] S. Cai, D. Breid, A. J. Crosby, Z. Suo, J.W. Hutchinson, Periodic patterns and energy states of buckled films on compliant substrates. *Journal of the Mechanics and Physics of Solids* **59**, 1094-1114 (2011).
- [104] R. V. Kohn, H.-M. Nguyen, Analysis of a Compressed Thin Film Bonded to a Compliant Substrate: The Energy Scaling Law. *Journal of Nonlinear Science* **23**, 343-362 (2012).
- [105] T. Tallinen, J. S. Biggins, L. Mahadevan, Surface Sulci in Squeezed Soft Solids. *Physical review letters* **110** (2013).
- [106] L. Ritchie, G. Xiao, Y. Ji, T. Chen, C. Chien, M. Zhang, J. Chen, Z. Liu, G. Wu, X. Zhang, Magnetic, structural, and transport properties of the Heusler alloys Co₂MnSi and NiMnSb. *Physical Review B* **68** (2003).
- [107] X. Liu, D. Mazumdar, B. Schrag, W. Shen, G. Xiao, Magnetization reversal of submicrometer Co rings with uniaxial anisotropy via scanning magnetoresistance microscopy. *Physical Review B* **70** (2004).
- [108] M. A. Vachon, G. Koutroulakis, V. F. Mitrović, O. Ma, J. B. Marston, A. P. Reyes, P. Kuhns, R. Coldea, Z. Tylczynski, The nature of the low-energy excitations in the short-range-ordered region of Cs₂CuCl₄ as revealed by ¹³³Cs nuclear magnetic resonance. *New Journal of Physics* **13**, 093029 (2011).

- [109] T. Cao, G. Wang, W. Han, H. Ye, C. Zhu, J. Shi, Q. Niu, P. Tan, E. Wang, B. Liu, et al. Valley-selective circular dichroism of monolayer molybdenum disulphide. *Nature communications* **3**, 887 (2012).
- [110] M. P. Levendorf, C. J. Kim, L. Brown, P. Y. Huang, R. W. Havener, D. A. Muller, J. Park, Graphene and boron nitride lateral heterostructures for atomically thin circuitry. *Nature* **488**, 627-632 (2012).
- [111] Z. Liu, Y. Gong, W. Zhou, L. Ma, J. Yu, J. C. Idrobo, J. Jung, A. H. MacDonald, R. Vajtai, J. Lou, et al. Ultrathin high-temperature oxidation-resistant coatings of hexagonal boron nitride. *Nature communications* **4**, 2541 (2013).
- [112] K. Kim, Z. Lee, B. D. Malone, K. T. Chan, B. Alemán, W. Regan, W. Gannett, M. F. Crommie, M. L. Cohen, A. Zettl, Multiply folded graphene. *Physical Review B* **83**, 245433 (2011).
- [113] Y. Chen, F. Guo, Y. Qiu, H. Hu, I. Kulaots, E. Walsh, R.H. Hurt, Encapsulation of particle ensembles in graphene nanosacks as a new route to multifunctional materials. *ACS nano* **7**, 3744-3753 (2013).
- [114] Z. Qin, M. Taylor, M. Hwang, K. Bertoldi, M.J. Buehler, Effect of wrinkles on the surface area of graphene: toward the design of nanoelectronics. *Nano letters* **14**, 6520-6525 (2008).
- [115] M. Ben Amar, A. Goriely, Growth and instability in elastic tissues. *Journal of the Mechanics and Physics of Solids* **53**, 2284-2319 (2014).
- [116] A. Goriely, M. Ben Amar, Differential Growth and Instability in Elastic Shells. *Physical review letters* **94** (2005).
- [117] B. Li, F. Jia, Y.-P. Cao, X.-Q. Feng, H. Gao, Surface Wrinkling Patterns on a Core-Shell Soft Sphere. *Physical review letters* **106** (2011).
- [118] P. Ciarletta, Buckling Instability in Growing Tumor Spheroids. *Physical review letters* **110** (2013).
- [119] F. Jia, B. Li, Y.-P. Cao, W.-H. Xie, X.-Q. Feng, Wrinkling pattern evolution of cylindrical biological tissues with differential growth. *Physical Review E* **91** (2015).
- [120] H. Vandeparre, M. Piñeirua, F. Brau, B. Roman, J. Bico, C. Gay, W. Bao, C.N. Lau, P. M. Reis, P. Damman, Wrinkling Hierarchy in Constrained Thin Sheets from Suspended Graphene to Curtains. *Physical review letters* **106**, 224301 (2011).
- [121] L. Meng, Y. Su, D. Geng, G. Yu, Y. Liu, R.-F. Dou, J.-C. Nie, L. He, Hierarchy of graphene wrinkles induced by thermal strain engineering. *Applied Physics Letters* **103**, 251610 (2013).
- [122] E. A. Korznikova, S. V. Dmitriev, Moving wrinkles in graphene nanoribbons. *Journal of Physics D: Applied Physics* **47**, 345307 (2014).
- [123] Q. Cao, H.S. Kim, N. Pimparkar, J. P. Kulkarni, C. Wang, M. Shim, K. Roy, M. A. Alam, J. A. Rogers, Medium-scale carbon nanotube thin-film integrated circuits on flexible plastic substrates. *Nature* **454**, 495-500 (2008).
- [124] C. Kocabas, H. S. Kim, T. Banks, J. A. Rogers, A. A. Pesetski, J. E. Baumgardner, S. V. Krishnaswamy, H. Zhang, Radio frequency analog electronics based on carbon nanotube transistors. *Proceedings of the National Academy of Sciences of the United States of America* **105**, 1405-1409 (2008).
- [125] D. H. Kim, J. Viventi, J. J. Amsden, J. Xiao, L. Vigeland, Y. S. Kim, J. A. Blanco, B. Panilaitis, E. S. Frechette, D. Contreras, et al. Dissolvable films of silk fibroin

- for ultrathin conformal biointegrated electronics. *Nature materials* **9**, 511-517 (2010).
- [126] J. Viventi, D. H. Kim, J. D. Moss, Y. S. Kim, J. A. Blanco, N. Annetta, A. Hicks, J. Xiao, Y. Huang, D.J. Callans, et al. A conformal, bio-interfaced class of silicon electronics for mapping cardiac electrophysiology. *Science translational medicine* **2**, 24ra22 (2010).
 - [127] I. Jung, J. Xiao, V. Malyarchuk, C. Lu, M. Li, Z. Liu, J. Yoon, Y. Huang, J. A. Rogers, Dynamically tunable hemispherical electronic eye camera system with adjustable zoom capability. *Proceedings of the National Academy of Sciences of the United States of America* **108**, 1788-1793 (2011).
 - [128] D. H. Kim, N. Lu, R. Ghaffari, Y. S. Kim, S. P. Lee, L. Xu, J. Wu, R. H. Kim, J. Song, Z. Liu, et al. Materials for multifunctional balloon catheters with capabilities in cardiac electrophysiological mapping and ablation therapy. *Nature materials* **10**, 316-323 (2011).
 - [129] J. Viventi, D. H. Kim, L. Vigeland, E. S. Frechette, J. A. Blanco, Y. S. Kim, A. E. Avrin, V.R. Tiruvadi, S.W. Hwang, A. C. Vanleer, et al. Flexible, foldable, actively multiplexed, high-density electrode array for mapping brain activity in vivo. *Nature neuroscience* **14**, 1599-1605 (2011).
 - [130] F. Molina-Lopez, D. Briand, N. F. de Rooij, Decreasing the size of printed comb electrodes by the introduction of a dielectric interlayer for capacitive gas sensors on polymeric foil: Modeling and fabrication. *Sensors and Actuators B: Chemical* **189**, 89-96 (2013).
 - [131] F. Molina-Lopez, A.V. Quintero, G. Mattana, D. Briand, N.F. de Rooij, Large-area compatible fabrication and encapsulation of inkjet-printed humidity sensors on flexible foils with integrated thermal compensation. *Journal of Micromechanics and Microengineering* **23**, 025012 (2013).
 - [132] A. Romeo, Q. Liu, Z. Suo, S. P. Lacour, Elastomeric substrates with embedded stiff platforms for stretchable electronics. *Applied Physics Letters* **102**, 131904 (2013).
 - [133] H. Vandeparre, Q. Liu, I. R. Minev, Z. Suo, S.P. Lacour, Localization of folds and cracks in thin metal films coated on flexible elastomer foams. *Advanced materials* **25**, 3117-3121 (2013).
 - [134] R. A. Bernal, A. Aghaei, S. Lee, S. Ryu, K. Sohn, J. Huang, W. Cai, H. Espinosa, Intrinsic bauschinger effect and recoverable plasticity in pentatwinned silver nanowires tested in tension. *Nano letters* **15**, 139-146 (2015).
 - [135] I. R. Minev, P. Musienko, A. Hirsch, Q. Barraud, N. Wenger, E.M. Moraud, J. Gandar, M. Capogrosso, T. Milekovic, L. Asboth, et al. Biomaterials. Electronic dura mater for long-term multimodal neural interfaces. *Science* **347**, 159-163 (2015).
 - [136] Y. Zhao, Y. Cao, W. Hong, M. Khurram Wadee, X. Q. Feng, Towards a quantitative understanding of period-doubling wrinkling patterns occurring in film/substrate bilayer systems. *Proceedings of the Royal Society A: Mathematical, Physical and Engineering Sciences* **471**, 2173 (2015).
 - [137] S. Im, R. Huang, Wrinkle patterns of anisotropic crystal films on viscoelastic substrates. *Journal of the Mechanics and Physics of Solids* **56**, 3315-3330 (2008).

- [138] E. P. Chan, K. A. Page, S. H. Im, D. L. Patton, R. Huang, C. M. Stafford, Viscoelastic properties of confined polymer films measured via thermal wrinkling. *Soft Matter* **5**, 4638 (2009).
- [139] M. K. Kang, R. Huang, Swelling-Induced Instability of Substrate-Attached Hydrogel Lines. *International Journal of Applied Mechanics* **03**, 219-233 (2011).
- [140] H. Mei, C.M. Landis, R. Huang, Concomitant wrinkling and buckle-delamination of elastic thin films on compliant substrates. *Mechanics of Materials* **43**, 627-642 (2011).
- [141] J. Li, Y. An, R. Huang, H. Jiang, T. Xie, Unique aspects of a shape memory polymer as the substrate for surface wrinkling. *ACS applied materials and interfaces* **4**, 598-603 (2012).
- [142] F. Weiss, S. Cai, Y. Hu, M. Kyoo Kang, R. Huang, Z. Suo, Creases and wrinkles on the surface of a swollen gel. *Journal of Applied Physics* **114**, 073507 (2013).
- [143] T. Jiang, R. Huang, Y. Zhu, Interfacial Sliding and Buckling of Monolayer Graphene on a Stretchable Substrate. *Advanced Functional Materials* **24**, 396-402 (2014).
- [144] V. Nayyar, K. Ravi-Chandar, R. Huang, Stretch-induced wrinkling of polyethylene thin sheets: Experiments and modeling. *International Journal of Solids and Structures* **51**, 1847-1858 (2014).
- [145] S. Chatterjee, C. McDonald, J. Niu, S. S. Velankar, P. Wang, R. Huang, Wrinkling and folding of thin films by viscous stress. *Soft Matter* **11**, 1814 (2015).
- [146] M. Destrade, R. W. Ogden, I. Sgura, L. Vergori, Straightening wrinkles. *Journal of the Mechanics and Physics of Solids* **65**, 1-11 (2014).
- [147] M. Destrade, R.W. Ogden, I. Sgura, L. Vergori, Straightening: existence, uniqueness and stability.Proceedings. *Mathematical, physical, and engineering sciences / the Royal Society* **470**, 20130709 (2014).
- [148] E. A. Korznikova, S. V. Dmitriev, Moving wrinkle in graphene nanoribbons. *Journal of Physics D: Applied Physics* **47**, 345307 (2014).
- [149] E. A. Korznikova, S. V. Dmitriev, Effect of the configuration of a wrinkle on the distributions of the energy and elastic strain in a graphene nanoribbon. *JETP Letters* **100**, 181-186 (2014).
- [150] D. Vella, A. Ajdari, A. Vaziri, A. Boudaoud, Wrinkling of Pressurized Elastic Shells. *Physical review letters* **107** (2011).
- [151] D. Blair, A. Kudrolli, 2005 Geometry of Crumpled Paper. *Physical review letters* **94** (2008).
- [152] D. P. Holmes, M. Ursiny, A. J. Crosby, Crumpled surface structures. *Soft Matter* **4**, 82 (2008).
- [153] A. D. Cambou, N. Menon, Three-dimensional structure of a sheet crumpled into a ball. *Proceedings of the National Academy of Sciences of the United States of America* **108**, 14741- 14745 (2011).
- [154] X. Ma, M.R. Zachariah, C.D. Zangmeister, Crumpled nanopaper from graphene oxide. *Nano letters* **12**, 486-489 (2012).
- [155] E. Araque, R. Villalonga, M. Gamella, P. Martínez-Ruiz, J. Reviejo, J.M. Pingarrón, Crumpled reduced graphene oxide–polyamidoamine dendrimer hybrid nanoparticles for the preparation of an electrochemical biosensor. *Journal of Materials Chemistry B* **1**, 2289 (2013).

- [156] S. Deboeuf, E. Katzav, A. Boudaoud, D. Bonn, M. Adda-Bedia, Comparative Study of Crumpling and Folding of Thin Sheets. *Phys Rev Lett* **110** (2013).
- [157] Y. Z. Liu, C. M. Chen, Y. F. Li, X. M. Li, Q. Q. Kong, M. Z. Wang, Crumpled reduced graphene oxide by flame-induced reduction of graphite oxide for supercapacitive energy storage. *Journal of Materials Chemistry A* **2**, 5730 (2014).
- [158] S. F. Ahmed, G.-H. Rho, K.-R. Lee, A. Vaziri, M.-W. Moon, High aspect ratio wrinkles on a soft polymer. *Soft Matter* **6**, 5709 (2010).
- [159] Y. Chen, F. Guo, A. Jachak, S.P. Kim, D. Datta, J. Liu, I. Kulaots, C. Vaslet, H.D. Jang, J. Huang, et al. Aerosol synthesis of cargo-filled graphene nanosacks. *Nano letters* **12**, 1996- 2002 (2012).
- [160] S. N. Naess, A. Elgsaeter, G. Helgesen, K.D. Knudsen, 2009 Carbon nanocones: wall structure and morphology. *Science and Technology of Advanced Materials* **10**, 065002 (1965).
- [161] G. Cao, X. Chen, C. Li, A. Ji, Z. Cao, Self-assembled triangular and labyrinth buckling patterns of thin films on spherical substrates, *Physical review letters* **100** 036102 (2008).
- [162] J. W. Gibbs, Scientific Papers, Dover, New York, 1961 (2008).
- [163] V. L. Ginzburg, L.D. Landau, L. D. Landau, Collected papers, Pergamon Press, Oxford, (1965).
- [164] D. Chen, L. Jin, Z. Suo, R. C. Hayward, Controlled formation and disappearance of creases. *Materials Horizons*, **1**, 207-213(2014).
- [165] S. Nagashima, H. Ebrahimi, K.-R. Lee, A. Vaziri, M.-W. Moon, Tunable nanochannels fabricated by mechanical wrinkling/folding of a stiff skin on a soft polymer. *Advanced Material Interfaces* **2**, 1400493 (2015).
- [166] N. Sridhar, D. J. Srolovitz, B. N. Cox, Buckling and post-buckling kinetics of compressed thin films on viscous substrates. *Acta Materialia* **50**, 2547–2557 (2002).
- [167] S. H. Im, R. Huang, Evolution of wrinkles in elastic-viscoelastic bilayer thin films. *Journal of Applied Mechanics* **72**, 955-961 (2005).
- [168] C. Werner, K. Engelhard, Pathophysiology of traumatic brain injury. *British journal of anaesthesia* **99** (1): 4-9 (2007).
- [169] J. Nortje, D. K. Menon. Traumatic brain injury: physiology, mechanisms, and outcome. *Current Opinion in Neurology* **17**:711–718 (2004).
- [170] A. Baethmann, J. Eriskat, M. Stoffel, D. Chapuis, A. Wirth, N. Plesnila, Special aspects of severe head injury: recent developments. *Current Opinion in Anaesthesiology* **11**, 193-200 (1998).
- [171] T. E. Moschandreou, Blood Cell: An Overview of Studies in Hematology. *InTech* 2012.
- [172] online source (lab material for anatomy course)
<http://www.iupui.edu/~anatd502/Labs.f04/circulatory%20lab/Circulatory%20System%20Lab.html>
- [173] M. Diab, R. Zhao, K. S. Kim, Journal Club Theme of February 2015: The Ruga Mechanics. (published online source)
<http://imechanica.org/node/17889>
- [174] H. Kolsky, Stress Waves in Solids. Clarendon Press, Oxford (1953).

[175] D.D.L. Chung, Review Materials for vibration damping. *Journal of Materials Science*, **36** (2001).